Spatial and Temporal Structure of Alfvén Resonator Waves at the Terrestrial Plasmapause

Von der Fakultät für Elektrotechnik, Informationstechnik, Physik
der Technischen Universität Carolo-Wilhelmina
zu Braunschweig
zur Erlangung des Grades eines
Doktors der Naturwissenschaften
(Dr.rer.nat.)
genehmigte
Dissertation

von Sebastian Schäfer
aus Braunschweig

Vorabveröffentlichungen der Dissertation

Teilergebnisse aus dieser Arbeit wurden mit Genehmigung der Fakultät für Elektrotechnik, Informationstechnik, Physik, vertreten durch den Mentor der Arbeit, in folgenden Beiträgen vorab veröffentlicht:

Publikationen:

Schäfer, S., K.-H. Glassmeier, P. T. I. Eriksson, V. Pierrard, K.-H. Fornaçon, L. G. Blomberg: Spatial and temporal characteristics of poloidal waves in the terrestrial plasmasphere: a CLUSTER case study, *Ann. Geophysicae, 25*, pp.1011-1024, 2007

Schäfer, S., K.-H. Glassmeier, P. T. I. Eriksson, P. N. Mager, V. Pierrard, K.-H. Fornaçon, L. G. Blomberg: Spatio-temporal structure of a poloidal Alfvén wave detected by Cluster adjacent to the dayside plasmapause, *Ann. Geophysicae, 26*, pp.1805-1817, 2008

Tagungsbeiträge:

Chapman Conference On Magnetospheric ULF Waves, San Diego, USA, 21.-25. März 2005, (Searching for Field Line Resonance: Case Studies From CLUSTER, Vortrag)

EGU General Assembly, Wien, Österreich, 24.-29. April 2005, (Searching for Field Line Resonance: Case Study From CLUSTER, Poster)

STIMGM Workshop(Solar - Terrestrial Interactions from Microscale to Global Models), Sinaia, Rumänien, 05.-09. September 2005, (Identification and Analysis of Field Line Resonances Using Cluster Satellites, Vortrag)

Cluster Symposium, ESTEC, Nordwijk, Niederlande, 19.-23. September 2005, (Identification of Field Line Resonances Using CLUSTER, Poster)

IMPRS Evaluation Meeting, Katlenburg-Lindau, Deutschland, 11. November 2005, (Field Line Resonances as Seen by CLUSTER, Poster)

Contents

Summary

The interaction of solar and terrestrial magnetic field and particle populations produces various plasma processes in the magnetosphere of the Earth. The most popular of these phenomena is the generation of polar lights in the auroral zones due to the collision of magnetospheric protons and electrons with particles of the upper atmosphere. Other processes, such as magnetic reconnection, are believed to be responsible for feeding energy into the magnetospheric plasma environment. This energy can be released in terms of wave activity generated by wave-wave or wave-particle interactions. Some of these waves are regarded as fluctuations of magnetospheric field lines fixed at the ends in the northern and southern ionosphere. In general these standing waves are divided into two wave types, poloidal and toroidal mode, oscillating with different eigenfrequencies due to the influence of field line curvature and external currents.

After decades of investigating ground based and in situ satellite observations some properties of such standing field line oscillations are well understood, however, numerous questions are still open concerning their spatial characteristics and temporal evolution. In particular the wave topology radial outward from the Earth is of interest. Due to gradients of plasma background parameters in this direction standing waves feature a complex structure and are able exist only in certain regions opaque for radial wave propagation. These so called Alfvén resonators are generated especially near the terrestrial plasmapause at a sharp change of plasma density.

Theoretical works aiming for a description of the spatio-temporal structure of Alfvén resonator waves need to account for the complex background conditions in the terrestrial magnetosphere. The results of these theories are desired to be compared with in situ observations, e.g. the Cluster mission that consists of four identical spacecraft. Its spatial separation allows a detailed analysis of spatial wave field characteristics and to distinguish them from temporal effects. As the perigees of the polar orbits are at around 4 R_E the satellites frequently cross the region near the inner or outer edge of the plasmapause and wave activity can be detected regularly in this region of interest.

Comparing theoretical concepts describing Alfvén resonator waves with spacecraft observations of standing field line oscillations can be considered as the primary concern of the present thesis. In Chapter 1 the plasma background conditions of the magnetosphere are described. Furthermore, origin and characteristic properties of toroidal and poloidal field line oscillations are introduced and discussed. The basic equations necessary for the determination of poloidal and toroidal eigenfrequencies are summarized in Chapter 2. Based on this the theoretically expected spatial structure of Alfvén resonator waves is described in Chapter 3 followed by discussing their temporal evolution in Chapter 4.

The Cluster mission is introduced in Chapter 5 explaining the advantages of the four spacecraft configuration and its orbit as well as briefly summarizing the functionality of

magnetic and electric field measurements.

Spatial and temporal characteristics of poloidal field line oscillations under investigation become very complex under realistic background conditions. A large number of parameters need to be considered, which has been done in this work. The evaluation of magnetospheric plasma conditions, such as density, pressure and magnetic field, is introduced in Chapter 6 together with further methods necessary for the analysis of magnetospheric wave activity. In particular, the numerical method used for the determination of toroidal and poloidal field line eigenfrequencies is presented.

Two case studies are presented in Chapters 7 and 8 discussing field line oscillations detected inside and outside the plasmapause boundary, respectively. Each study concentrates on a detailed analysis of a standing poloidal field line oscillation observed in spacecraft magnetic and electric field measurements. Energy flux and azimuthal wave numbers m are determined. In the first case study one takes advantage of a large scale satellite configuration with spacecraft separation up to 2.5 R_E, while the second case is characterized by a small tetrahedron with spacecraft distances of around 0.2 R_E. Each configuration allows the application of specific analysis techniques that are developed and applied for the first time for the investigation of standing wave fields in the magnetosphere. In both cases a field line related coordinate system enables the estimation of spatial extension in the radial direction of the wave field as well as its temporal decay rate. In addition a range-time-intensity data representation possible for the small spacecraft constellation allows an accurate identification of a phase jump in the radial direction and indicates the same field lines are excited to a standing wave oscillation twice.

In both case studies the determination of toroidal and poloidal eigenfrequencies reveals that the conditions for the excitation of Alfvén resonator waves are not fully satisfied. However, the plausibility of the resulting information about the spatio-temporal wave topology is tested by modeling standing wave fields and comparing with the amplitude modulation in the observed signals. The theoretically expected localizations and sizes of the Alfvén resonators are determined for realistic plasma background conditions and compared with the position finding of the observed wave fields. Spatial and temporal properties of the analyzed wave fields are in good agreement with main features predicted by the applied theoretical framework, which is capable to provide a deeper insight into the properties of magnetospheric plasma waves.

1 Introduction

1.1 The terrestrial magnetosphere

The terrestrial magnetic field originates from a dynamo process inside the molten iron core of the Earth. The flow of conducting material through an existing weak magnetic field induces electrical currents which in turn produce magnetic fields. This cumulative interaction results in measurable magnetic field strengths and the formation of a magnetic field that is described in first approximation by a dipole field, currently inclined by $11.5°$ compared to the Earth's rotation axis. The shape of the terrestrial magnetosphere is illustrated in Fig. 1.1. Its outer boundary, called the magnetopause, is determined by the balance of the dynamic pressure of the super-alfvénic solar wind flow and the magnetic pressure at the outer edge of the magnetosphere. Due to the presence of the Earth's magnetic field the charged polar wind particles cannot enter the magnetosphere directly and flow along the magnetopause with sub-alfvénic speed decelerated by the bow shock wave (see Fig. 1.1). At the dayside the solar wind compresses the geomagnetic field, while at the nightside the field lines are deformed to a magnetic tail.

The magnetosphere consists of several spacious currents systems and different plasma populations (Fig. 1.1), where in the following the regions of interest for this thesis are briefly described. The innermost part of the magnetosphere is the plasmasphere, first discovered by Carpenter (1963), constituting the extension of the ionosphere in magnetospheric regions. The sunlit ionosphere leaks up into space along magnetic field lines, slowly filling dayside flux tubes with ionospheric plasma (Goldstein 2006). Due to the Earth's eastward rotation the dayside filling produces a torus of cold plasma with particle energies of approximately 1 eV that is composed of H^+ ions (up to 80%) and significant rates of heavier ions such as He^+, O^+, and O^{2+} (e.g. Berube et al. 2005).

The configuration of the plasmaspheric particles depends on the electric field that is formed by the interplay of the co-rotation and the convection electric field. Due to reconnection processes at the dayside magnetopause magnetic flux tubes and plasma convects with the solar wind velocity V_{SW} over the polar caps to the magnetotail (Dungey 1961). According to the Lorentz transformation a electric field emerges in the Earth's fixed frame of reference given by $E_{con} = -V_{SW} \times B_z$, where B_z the z-component of the magnetic field. This convection electric field is directed from dawn to dusk and can be assumed as homogeneous. It causes a sunward convection of plasma in the inner magnetosphere (e.g. Baumjohann and Treumann 1996). The co-rotation electric field results from the viscous coupling of the ionospheric plasma with the planetary rotation, which induces an electric field in the ionosphere given by $E_{cor} = -V_{rot} \times B$, where V_{rot} is the rotation speed. As magnetic field lines are equipotential lines, this electric field is transported in
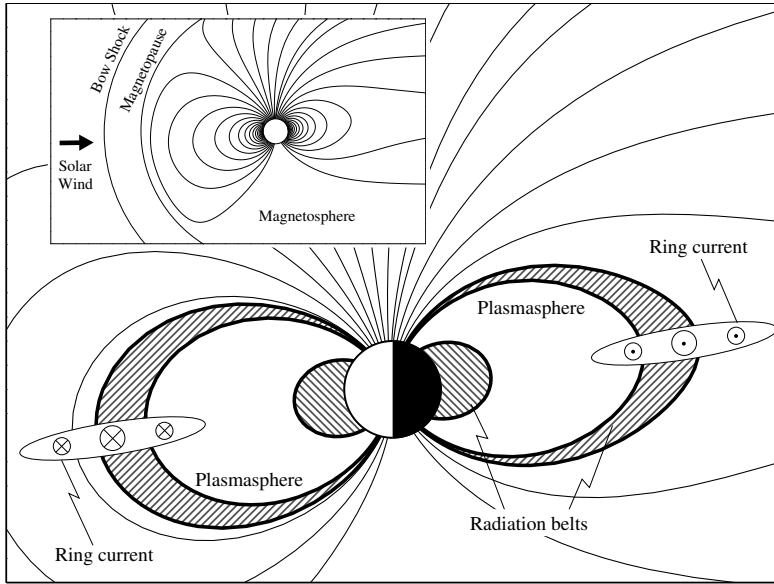
Figure 1.1: Sketch of terrestrial magnetosphere

the plasmasphere and forces the plasma contained therein to co-rotation. The equipotential lines of the radially symmetric co-rotation and the homogeneous convective electric fields are illustrated in Fig. 1.2, as well as the resulting combination of both fields. In this picture the outer surface of the plasmasphere, called the plasmapause, coincides with the last closed equipotential surface of the electric field. Inside the plasmasphere co-rotation dominates and the plasma density is high. Outside this region the equipotential lines are open, so that flux tubes end at the magnetopause and loose their plasma, which explains the strong density gradient at the plasmapause (e.g. Baumjohann 1991).

However, the above explanation of the plasmapause origin requires a stable magnetospheric electric field for an ideal plasmapause frontier to form. But the variations of geomagnetic activity are too fast and the condition of stationary E_{con} is never achieved. An alternative explanation for plasmapause formation has been proposed by Lemaire (1974). The outer boundary of the plasmasphere is determined by the "Zero Parallel Force Surface" (ZPFS) where the gravitational force is overtaken by the centrifugal force. The pressure gradient will force the particles to move outwards across the equipotential surfaces where they finally are lost at the magnetopause. Accordingly, convective instabilities at the ZPFS in the post midnight sector, where the convection velocity is maximum, determines the plasmapause location in this region, which is then carried by the planetary rotation. During periods of increasing solar activity the plasmapause is peeled off in the post-midnight sector and moves closer to the Earth due to the depletion of the outer flux tubes. In the
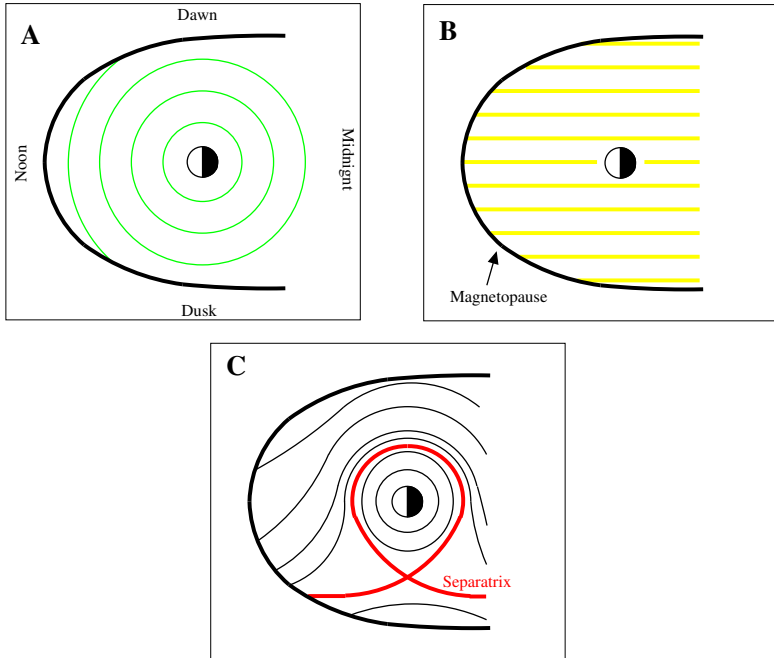
Figure 1.2: Equipotential lines of the magnetospheric electric field. The total field as displayed in panel C is composed of the co-rotation field (panel A) and the convection field (panel B).

opposite case the plasmapause shifts to larger radial distances. Consequently, the equatorial position of the plasmapause varies from 2.5 R_E to 7.0 R_E depending on the level of geomagnetic activity (e.g. Carpenter and Anderson 1992, Moldwin et al. 2002). According to this mechanism the plasmapause is not circular, but can exhibit complex structures, such as shoulders, caused by a sudden increase of geomagnetic activity, or plumes in the afternoon section due to differential rotation (e.g. Goldstein et al. 2002, Pierrard and Lemaire 2004, Pierrard and Cabrera 2005).

Next to the plasmasphere the radiation belts, or "Van Allen" belts, are regions of trapped particle populations in the inner magnetosphere containing high-energy ions and relativistic electrons. These particles are believed to be generated by the collision of cosmic rays with atomic nuclei of the atmospheric gas leading to the diffusion of neutrons released in this way into the magnetosphere. The neutrons resolve into high energetic protons and electrons stored in the local magnetic field. Depending on their energy the particles are separated into two belts, an inner belt below $L \approx 2$ and an outer belt above $L \approx 3$ (e.g. Goldstein 2006). Protons with energies larger than 20 MeV are stored in the inner belt,

which is quite stable, affected only by strongest geomagnetic storms. The outer belt is populated mainly by relativistic electrons with energies of around 20 MeV and can move inward to penetrate the region between the belts during times of intense storms (Baker et al. 1994). On average the the outer extent of the plasmasphere coincide with the inner boundary of the radiation belt, as the electrons are scattered by broad-band whistler mode waves commonly observed in the plasmasphere (e.g. Goldstein et al. 2005).

In general all trapped particles in the inner magnetosphere execute three basic motions: a gyration around magnetic field lines, a bounce motion between magnetic mirror points above northern and southern ionospheres and drift motions according to the gradient of magnetic magnitude perpendicular to the field lines and due to the curvature of the magnetic field lines (e.g. Baumjohann and Treumann 1996). The total effect of the latter motion is a collective azimuthal drift oppositely directed for ions moving westward and electrons moving eastward. The resulting current associated with this charge transport is the ring current (Daglis et al. 1999). Significant current densities are produced by a population H^+ and O^+ ions in the medium-energy range of 1 - 100 keV that originates from the ionosphere and the solar wind (Williams 1981). During undisturbed periods the ring current is distributed between $L = 2$ and $L = 9$ and is mainly composed of protons (e.g. Lui and Hamilton 1992). The storm time ring current is characterized by increasing current density over its whole radial extend and rising density of O^+ ions (Lui et al. 1987).

1.2 Observation of magnetospheric ULF pulsations

A wide variety of magnetohydrodynamic waves occurs in magnetospheric regions of the Earth excited by different processes inside the magnetosphere and the solar wind. Waves in the ultra low frequency (ULF) range below 1Hz are classified with respect to their waveform and frequency, where quasi-sinusoidal oscillations are called "Pc" (French: pulsation continue) and oscillations with irregular waveforms are called "Pi" (French: pulsation impulsive) (Jacobs et al. 1964). Each major type is subdivided into frequency bands roughly corresponding to distinct phenomena. Although the limits of these bands are not precise in consideration of present knowledge, standing field line oscillations are in general associated with Pc3 to Pc5 waves corresponding to a frequency range between 1 mHz and 100 mHz. Contrary, oscillations classified as Pc1-2 are traveling waves with frequencies up to 5 Hz, such as ion-cyclotron waves, and Pi1-2 oscillations are excited by geomagnetic substorms (e.g. Heacock 1967).

A standing wave in the magnetosphere implies that a bunch of magnetic field lines with a length of several Earth radii is excited to an oscillation comparable to a guitar string. Such oscillations exhibits the largest wave amplitude compared to other waves in the ULF range. Accordingly, at first this type of magnetospheric wave has been detected with ground based measurements. The first published record of a giant pulsation appears to be that of Balfour Stewart during the great magnetic storm on September 1, 1859. A reproduction of Stewart's observation can be found in Glassmeier (1995). The magnetic storm, which is presumed to be one of the strongest in history, is comprehended by Tsurutani et al. (2003). At the beginning of the twentieth century it has been noticed that the recurrence of geomagnetic disturbances coincide with the rotation period of the sun. A possible explanation for this phenomenon was given by J. Bartels in 1932 who suggested that the so-called M-regions

on the sun are a source of solar corpuscular streams. These regions are now identified as coronal holes. Finally, the connection of solar activity and geomagnetic disturbances has been explained by Chapman and Ferraro (1931, 1932, 1933) who proposed that magnetic storms occurs when clouds of solar plasma collide with the Earth's magnetic field.

Since that time the interest on exploring magnetospheric activity increases steadily. Several large-area magnetometer arrays, such as CARISMA[1] or the Scandinavian IMAGE[2] network, have been build and equipped with up to date senors that allow for accurate detection and analysis of magnetospheric pulsations. Furthermore, ULF wave activity can be observed by radar measurements, e.g. the STARE[3] system at the northern and the SuperDarn[4] at the southern hemisphere. In general ground based measurements allow long duration observations of field lines excited by ULF waves (e.g. Samson et al. 1971, Walker et al. 1979, Fenrich et al. 1995). However, amplitude and polarization of these waves observed at the ground are modified by the ionosphere (Hughes 1974, Hughes and Southwood 1976, Glassmeier 1984) and consequently, modeling of the ionospheric screening effect is necessary for an accurate understanding of the ground based observations (e.g. Glassmeier 1988, Sciffer et al. 2004, 2005).

Finally, evidence of the existence of magnetospheric ULF waves has been supplied by spacecraft measurements, which in contrast to ground based observations provide direct insight into the wave structure. Especially results obtained from the double spacecraft mission ISEE[5] by e.g. Singer and Kivelson (1979) and Singer et al. (1982), as well as from the single spacecraft mission AMPTE[6] by e.g. Engebretson and Cahill (1981) and Engebretson et al. (1986) have increased the knowledge about the spatial structure of standing field line oscillations. However, single and double spacecraft observations have a limitation as they exhibit an ambiguity between spatial and temporal variations. A multi-spacecraft mission is not affected by this limitation and hence the four Cluster spacecraft (Escoubet et al. 1997) are suitable to investigate both, the spatial and temporal structure of ULF pulsations as shown in this thesis and in recent studies (e.g. Eriksson et al. 2005a, Schäfer et al. 2007, 2008).

Investigating magnetospheric ULF waves allows to study plasma waves under background conditions that cannot be achieved by conventional laboratory experiments. It conduces to raise the understanding of the interaction of solar wind plasma and the terrestrial magnetosphere. A detailed theoretical knowledge of general ULF wave properties allows in turn the monitoring of magnetospheric plasma conditions (e.g. Menk et al. 1999, Denton et al. 2001, Takahashi et al. 2004). In this context standing field line oscillations are wave phenomena of particular interest as they are frequently detected by ground and satellite observations. In general two different types of standing waves exist in the magnetosphere, toroidal and poloidal oscillations. Their generation processes as well as their theoretically expected and observed wave characteristics are introduced in the following sections 1.3 and 1.4, respectively.

---

[1]Canadian Array for Realtime Investigations of Magnetic Activity
[2]International Monitor for Auroral Geomagnetic Effects
[3]Scandinavian Twin Auroral Radar Experiment
[4]Super Dual Aurora Radar Network
[5]International Sun Earth Explorer
[6]Active Magnetospheric Particle Tracer Explorer
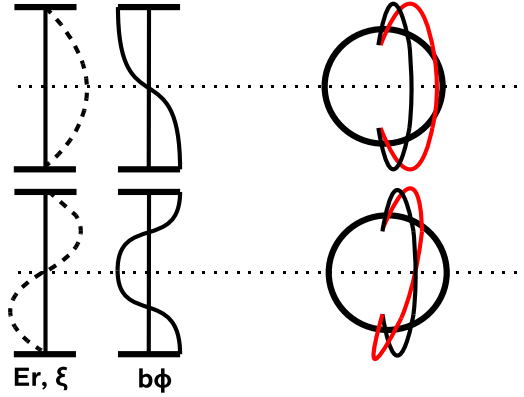
Figure 1.3: Left: Field aligned structure of a first harmonic (top) and a second harmonic (bottom) toroidal oscillation, where E_r is the radial component of the electric field, ξ the displacement vector and b_ϕ the azimuthal component of the magnetic field disturbance. Right: Sketch of the azimuthal field line oscillation, where the red line marks the disturbed field line.

1.3   Toroidal field line oscillations

Toroidal oscillations are believed to be driven by sources external of the magnetosphere, such as solar wind impulses (Allan et al. 1986) and Kelvin-Helmholtz instabilities at the magnetopause (Fujita et al. 1996, Engebretson et al. 1998) generating a compressional wave which propagates across magnetic field lines. Due to the process known as field line resonance (Tamao 1965, Southwood 1974), the compressional wave can be transformed to an Alfvén wave propagating parallel to the magnetic field. Wave reflection at the ionosphere can lead to the formation of a standing wave at a specific field line. Mode coupling of an incoming fast magnetosonic wave to an Alfvén wave occurs at magnetic field lines where the field parallel component of the phase velocity of the compressional wave matches the local Alfvén velocity $V_A = B_0 / \sqrt{\mu_0 \rho_0}$ that is influenced by local magnetic field strength B_0 and plasma mass density ρ_0. When the length of the field line is an integer multiple of the half Alfvén wavelength, the coupling between both wave modes becomes resonant. Initially, this field line resonance process was described in a box model of the magnetosphere with straight magnetic field lines (Tamao 1965, Southwood 1974, Kivelson and Southwood 1986), however, it appears also in dipolar magnetic field configuration (e.g. Chen and Cowley 1989).

The physical resonant mode coupling can be understood considering electric current continuity. From Maxwell's equations the following wave equation is derived for low-frequency waves:

$$\nabla \times \nabla \times \boldsymbol{E} + \mu_0 \frac{\partial \boldsymbol{j}}{\partial t} = 0. \tag{1.1}$$

Here E denotes the wave electric field, and j is the electric current density driving the wave. A magnetohydrodynamic wave in a homogeneous plasma carries polarization currents

$$j_p = \frac{1}{\mu_0 V_A^2} \frac{dE}{dt}. \qquad (1.2)$$

For an Alfvén mode this polarization current is curl-free in a plane whose normal is the background magnetic field B_0. The fast mode carries a source-free polarization current. Considering a fast mode type perturbation with its source-free current in an inhomogeneous medium with spatially changing Alfvén velocity, current continuity requires the fast mode carried current to be partially closed via field-aligned currents driving Alfvénic perturbations carried by a curl-free polarization current system. If the phase velocity component of the fast mode parallel to the background magnetic field is equal to the local Alfvén velocity, both waves have ample opportunity to exchange their energy; resonance takes place.

Toroidally oscillating field lines generated by such a resonance process are standing Alfvén waves, which implies that their magnetic field is perturbed in the azimuthal direction and the electric field in the radial direction. That means a toroidal wave mode can be understood as an oscillation of magnetic shells. The corresponding field aligned structure is illustrated in Fig. 1.3. Due to the high ionospheric conductivity electric field and displacement are zero at the ends of the field line, while the magnetic field exhibits an amplitude maximum (e.g. McPherron 2005). Consequently, for the fundamental and higher odd modes the magnetic field have a node in the magnetic equatorial plane and the electric field an anti-node. For the second and higher even harmonics this characteristic is reversed. The azimuthal directed perturbation of the toroidal mode is most efficient at magnetospheric flanks, where the solar wind flows perpendicular to the magnetic field lines (e.g. Allan and Poulter 1992). The resulting elliptical polarized wave feature opposite directed wave polarizations on the morning and evening sector (Samson et al. 1971, Samson 1972, Samson and Rostoker 1972). The radial structure of the toroidal Alfvén wave is expected to show an almost Gaussian amplitude variation across magnetic L shells accompanied with a 180° change in the wave phase around the resonant magnetic field line (Southwood 1974). Both spatial features were detected in ULF pulsations by ground magnetometer and ionospheric observations, respectively (e.g. Glassmeier et al. 1984a, Walker et al. 1979). The observed lifetime of resonant field line oscillations is between several minutes and more than one hour limited due to wave damping at the ionosphere, where the wave energy dissipates due to Joule heating (e.g. Glassmeier et al. 1984b).

An important parameter of field line oscillations is the azimuthal wave number m, which is defined as the number of wavelengths fitting into a shell of oscillating field lines. The field line resonance process is most efficient for small azimuthal wave numbers $m \sim 1$ (e.g. Kivelson and Southwood 1986, Lee and Lysak 1990), i.e. the toroidal wave field is expected to exhibit a large spatial structure in the azimuthal direction. The left plot in Fig. 1.4 illustrates the azimuthal displacement of a toroidal mode with $m = 0$. Strictly speaking, only this mode describes a toroidal wave, as magnetic field magnitude and plasma density are not changed by the wave. Oscillations with higher m-values are compressed in the azimuthal direction and are coupled with a poloidal mode that features a non-zero radial component. However, the azimuthal structure of low-m waves is much larger than the
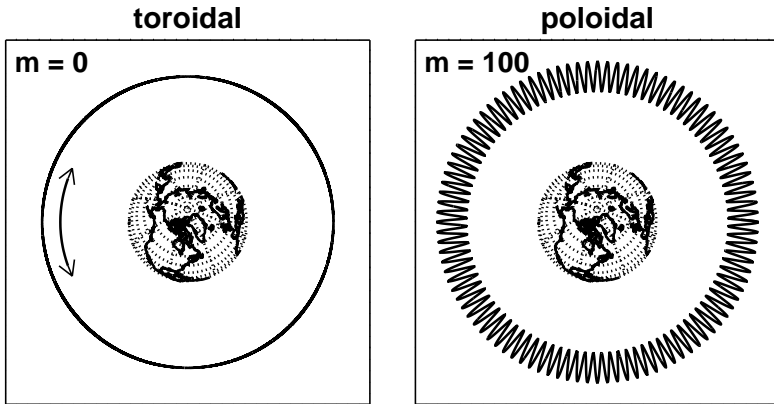
Figure 1.4: View on the displacement of a magnetic shell in the equatorial plane for the toroidal (left) the and poloidal (right) wave mode. The arrow illustrates the perturbation of the toroidal mode in the azimuthal direction. The exemplary poloidal mode has an azimuthal wave number of $m = 100$.

radial structure and waves with $m \leq 10$ are denoted as toroidal Alfvén waves.

1.4   Poloidal field line oscillations

Poloidal oscillations are characterized by a displacement of the field lines in the radial causing a compression of the magnetic field. In case the compressive perturbation of the magnetic field is small compared to the radial one, poloidal oscillations are usually referred as poloidal Alfvén waves. Its field aligned structure is similar to toroidal waves, however, the radial displacement of magnetic field lines lead to a "breathing" oscillation (Fig. 1.5).

Contrary to the toroidal mode poloidal field line oscillations are considered to derive their energy by processes inside the magnetosphere. Possible candidates for the generation of poloidal ULF wave activity are drift mirror (Hasegawa 1969) and bounce instabilities (Southwood et al. 1969, Southwood and Kivelson 1982, Glassmeier et al. 1999). In particular the azimuthal flow of ring current particles is suitable for the generation of resonant wave particle interaction. Details of this resonance process are given in Sec. 4.4. In this way excited poloidal waves should preferentially adopt an electric field node at the magnetic equator, as exists for even harmonic standing waves, and rapid phase variations perpendicular to magnetic field lines (Southwood 1983). This expectation is supported by the observation of second harmonic poloidal waves prevalently at the dayside near magnetic noon and afternoon (e.g. Cummings et al. 1969, Engebretson et al. 1988, Anderson et al. 1990, Takahashi and Anderson 1992). Also third harmonic poloidal oscillations have been detected around magnetic noon in the vicinity of the plasmapause (e.g. Takahashi and Anderson 1992). These odd harmonic waves are supposed to be excited by drift wave
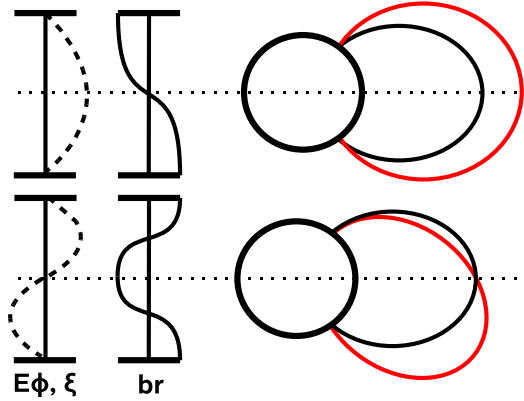
Figure 1.5: Left: Field aligned structure of a first harmonic (top) and a second harmonic (bottom) poloidal oscillation, where E_ϕ is the azimuthal component of the electric field, ξ the displacement vector and b_r the radial component of the magnetic field disturbance. Right: Sketch of the azimuthal field line oscillation, where the red line marks the disturbed field line.

instabilities in the ring current region (e.g. Hasegawa 1971, Chen and Hasegawa 1991b, Cheng and Qian 1994).

A main characteristic of poloidal field line oscillation is the large azimuthal wave number $m \gg 1$ (e.g. Allan et al. 1983) corresponding to a small azimuthal wave structure (right plot in Fig. 1.4). Wave numbers up to $m \approx 30$ have been detected using ground based observations (e.g. Glassmeier 1980), while poloidal waves with $m > 100$ have been observed in spacecraft measurements (e.g. Eriksson et al. 2005a, Schäfer et al. 2008). A suitable theoretical framework to interpret the spatial structure of poloidal oscillations with large m-values has been presented by e.g. Leonovich and Mazur (1990). Some of their results can be understood again considering the different currents associated with the restoring forces influencing the wave. For example, the influence of a finite plasma β can be incorporated in Eq. 1.1 by a diamagnetic current

$$j_\beta = \frac{\nabla P \times B_0}{B_0^2}. \tag{1.3}$$

Magnetic field line curvature introduces curvature currents j_c. If the background plasma carries a significant electric current J as observed in the ring current region a further current,

$$j_J = \frac{(J \times b) \times B_0}{B_0^2}, \tag{1.4}$$

needs to be considered when solving Eq. 1.1; here b denotes the magnetic field perturbation vector. This current describes forces associated with work done by the perturbed plasma

against the current-carrying background. Each of these additional currents influences wave dispersion and propagation velocity of ULF waves observed in the magnetosphere. Based on this Leonovich and Mazur (1990, 1993, 1995) and Klimushkin (1998a) have derived a rather general theoretical framework to describe the dispersion characteristics of ULF waves in more complex background plasma situations. Especially the curvature currents are important as they introduce transverse dispersion causing large-m waves to propagate in radial direction. Wave propagation inwards is hampered by the increasing plasma mass density and magnetic field strength; the inner magnetosphere/plasmasphere becomes opaque and a poloidal turning point exists.

Wave propagation outwards, however, is possible. As the local eigenfrequencies of toroidal and poloidal modes are different any outward propagating large-m poloidal wave may couple to a toroidal oscillation. Poloidal perturbations are related to toroidal transverse currents carrying the wave. As the azimuthal wave number m is large this toroidal current changes sign rapidly also in azimuthal direction. Current continuity requires the transverse divergence of this current to be closed via field-aligned and poloidal currents. This causes coupling between the primary poloidal magnetic field perturbation and a secondary toroidal magnetic field oscillation. If the local eigenfrequencies of the poloidal and toroidal oscillations match a local toroidal field line resonance occurs. Wave propagation is thus restricted to a region bounded by the poloidal turning point and the toroidal resonance point.

The radial structure of the wave field changes in time from a Gaussian-like distribution at the beginning to a complex and small-scaled structure at the end of the lifetime. Simultaneously, the wave polarization changes from poloidal to toroidal. An explanation for this spatio-temporal behavior can also be given by considering phase mixing effects on field lines excited independently and oscillating with their own eigenfrequencies (e.g. Mann and Wright 1995). This region thus defines a magnetospheric resonator or wave guide (Leonovich and Mazur 1995), which can be generated when poloidal and toroidal eigenfrequencies vary monotonic across magnetic L shells.

The outer boundary of the resonator can be another poloidal turning point, not a toroidal resonance, depending on plasma background properties (e.g. Vetoulis and Chen 1994, 1996, Leonovich and Mazur 1995, Denton and Vetoulis 1998, Klimushkin 1998a). The existence of two radially arranged turning points suggests that a poloidal wave trapped in this kind of resonator can propagate in both directions, inward as well as outward. This particular condition is satisfied at the inner and outer edge of the plasmapause, where the radial distribution of plasma density reaches a minimum and maximum, respectively. Mager and Klimushkin (2006) have modeled the spatio-temporal structure of a standing Alfvén wave in such an wave resonator assuming an impulse wave source. For a fundamental harmonic structure along the field line ($N = 1$) they predict a radial structure of the wave field comparable to a Gaussian and a constant poloidal wave polarization. By contrast, the radial structure of the second longitudinal harmonic ($N = 2$) develops soon after the impulse from a Gaussian distribution across L shells to smaller radial scales, similar to the radially propagating wave discussed above. Observations of poloidal Alfvén waves usually reveal a second harmonic structure of the oscillation along the field line (e.g. Takahashi and Anderson 1992). Furthermore the radial localization of the wave field requires a change in the wave phase by 180° across L shells (Klimushkin et al. 2004).

Many ULF pulsation observations, though interpreted as toroidal field line resonances

as described in Sec. 1.3, lag a definite proof of their resonant character as single spacecraft observations do not allow to demonstrate the spatial localization of the wave amplitude and the typical 180° phase change of the toroidal component in radial direction. What is observed is usually a spatial localization in the radial or poloidal component, not the toroidal component (e.g. Singer et al. 1979, 1982, Singer 1982, Cramm et al. 2000). As such poloidally localized waves exhibit large azimuthal wave numbers $m \approx 50 - 150$ the field line resonance mechanism cannot be used as an explanation to understand these poloidal resonances. Leonovich and Mazur (1990) give a simple reason for this: In the limit $m \to 0$ the azimuthal component of the wave vector k_ϕ is equal to infinity. But also the radial component k_r tends to infinity in case of an ideal resonance. Because of $\nabla \cdot \boldsymbol{B} = 0$ the direction of the transverse magnetic field component is not defined.

Accordingly, the spatio-temporal structure of large-m poloidal waves is rather complex compared to that of a classical field line resonance due to the radial confinement within two possible magnetospheric resonator regions and their change of wave polarization from poloidal to toroidal in time, as discussed in Sec. 1.4. Detailed studies of the spatial variations and the temporal evolution of the ULF wave field in such regions are thus desirable and will allow a deeper insight into the plasma physical processes there.

2 Theory of field line oscillations

2.1 Basic equations

The theoretical treatment of magnetospheric ULF waves needs a formulation of MHD waves under realistic background conditions, such as a inhomogeneous plasma with curved field lines and a small but finite plasma β. Based on these requirements in this section the derivation of a system of equations is summarized describing hydromagnetic waves. Initially the method used was developed by Leonovich and Mazur (1990, 1993) and later applied by e.g. Klimushkin et al. (1995) and Klimushkin (1997) investigating the influence of various background conditions on magnetospheric Alfvén waves. A detailed review of this method can be found in Klimushkin et al. (2004) containing the main features of the theoretical framework necessary for the analysis of ULF pulsations (Sec. 7 and 8).

To account for the field line curvature a curvilinear and orthogonal coordinate system $\{x_1, x_2, x_3\}$ is introduced, in which $x_1 = const$ coincide with a magnetic shell, i.e. it represents the radial direction comparable to the known McIlwain parameter L (McIlwain 1966). The coordinate x_2 resembles the azimuthal direction, i.e. it gives the magnetic local time (MLT) of a field line on a specific L shell. The coordinate x_3 completes the system by representing a point on a specific field line for constant coordinates x_1 and x_2. In this coordinate system, which is shown in Fig. 2.1, a length element is specified by

$$ds^2 = g_1(dx_1)^2 + g_2(dx_2)^2 + g_3(dx_3)^2. \tag{2.1}$$

Here $g_i = g_{ii}(x_1, x_3)$ are the diagonal components of the metric tensor, whose non-diagonal components are zero. The determinant of the metric tensor is $g = g_1 g_2 g_3$.

If the radial coordinate is $x_1 = L$, the azimuthal angel $x_2 = \phi$ and the field parallel coordinate given by the geomagnetic latitude θ, the the components of the metric tensor have the form $g_1 = \cos^6 \theta (1 + 3 \sin^2 \theta)^{-1}$ and $g_2 = L^2 \cos^6 \theta$. According to Eq. 2.1 a field parallel length element is given by

$$dl = \sqrt{g_3} dx_3 = h_\theta d\theta \tag{2.2}$$

with

$$h_\theta = L \cos \theta \sqrt{1 + 3 \sin^2 \theta}.$$

This coordinate system is orthogonal provided that $\boldsymbol{J} \cdot \boldsymbol{B} = 0$ (Salat and Tataronis 2000), which is fulfilled in the magnetosphere, as the magnetospheric ring current is perpendicular to the background magnetic field:

$$\boldsymbol{J} = \frac{1}{\mu_0} \nabla \times \boldsymbol{B} = \boldsymbol{J}_\perp. \tag{2.3}$$
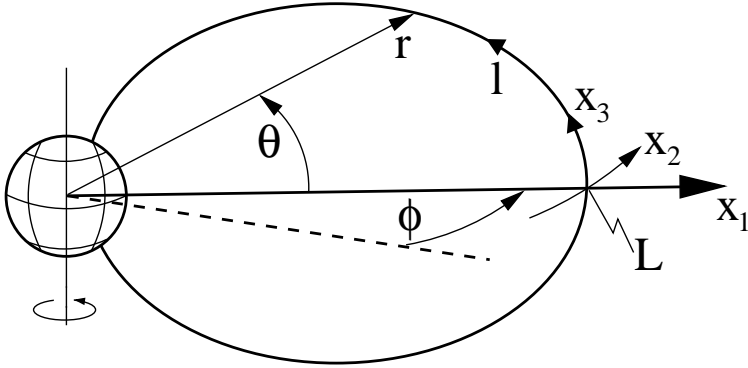
Figure 2.1: Curvilinear orthogonal coordinate system, adapted from Leonovich et al. (2006).

In the following, small amplitude oscillations are considered, that permit the wave field to be represented as plane waves. The equilibrium plasma quantities such as magnetic field, current density, plasma pressure and density are designated as $\boldsymbol{B}_0$, $\boldsymbol{J}_0$, P_0 and ρ_0, while the corresponding perturbed quantities are $\boldsymbol{b}$, $\boldsymbol{j}$, δp and ρ. The magnetosphere is considered within the axial symmetry approximation and the equilibrium parameters are independent of the azimuthal coordinate x_2. All perturbed quantities, including the plasma displacement ξ and the electric field $\boldsymbol{E}$, will be assumed to have the form

$$\xi(L, \phi, \theta) \propto \xi(L, \theta) \exp(-i\omega t + im\phi), \tag{2.4}$$

where m is the azimuthal wave number and ω the frequency of the oscillation.

Within the inner magnetosphere the plasma pressure P is isotropic in good approximation (e.g. Lemon et al. 2003) and the plasma equilibrium must adhere to the condition

$$\nabla P = \boldsymbol{J} \times \boldsymbol{B} = \frac{(\boldsymbol{B} \cdot \nabla)\, \boldsymbol{B}}{\mu_0} - \frac{\nabla B^2}{2\mu_0}. \tag{2.5}$$

The equilibrium requires a compensation of the pressure gradient by the magnetic force due to the magnetic field configuration. The first term of the right side of Eq. 2.5 includes the influence of the curvature of magnetic field lines. This term is often neglected in order to simplify the magnetospheric configuration to a box model with straight field lines (e.g. Southwood 1974, Klimushkin 1997). However, as field line curvature in particular triggers the main differences between poloidal and toroidal field line oscillations (see details in Sec. 2.2), it is incorporated in the theoretical description of the present work.

The linearized MHD equation of motion for an oscillation in a hot plasma is given by (e.g. Goossens 1991)

$$-\rho\omega^2\boldsymbol{\xi} + \nabla\delta p = \frac{1}{\mu_0}\boldsymbol{J}_0 \times \nabla \times (\boldsymbol{\xi} \times \boldsymbol{B}_0) - \frac{1}{\mu_0}\boldsymbol{B}_0 \times \nabla \times \nabla \times (\boldsymbol{\xi} \times \boldsymbol{B}_0), \tag{2.6}$$

where the pressure perturbation p is given by the adiabaticity condition in its linearized form:

$$\delta p = -\boldsymbol{\xi} \cdot \nabla P_0 - \gamma P_0 \nabla \cdot \boldsymbol{\xi}. \tag{2.7}$$

The equation of motion (Eq. 2.6) provides three equations of the displacement vector ξ, which in principle contain all information about the wave field. A convenient way to obtain the structure of the wave field is the transformation of Eq. 2.6 to three functions describing the wave modes of an inhomogeneous hot plasma, the Alfvén mode, the fast and the slow magnetosonic mode, respectively (e.g. Klimushkin 1998b).

For that purpose one uses the two dimensional nature of the wave electric field $\boldsymbol{E} = (E_1, E_2, 0)$ caused by the perfect plasma conductivity. In this case the frozen-in theorem is valid given in its linearized form by

$$\boldsymbol{E} = -i\omega\boldsymbol{\xi} \times \boldsymbol{B}_0 \ \text{ or } \ \boldsymbol{\xi} = -\frac{i}{\omega}\frac{\boldsymbol{B}_0 \times \boldsymbol{E}}{B_0^2}, \tag{2.8}$$

i.e. the electric field is always perpendicular to the background magnetic field $\boldsymbol{B}_0$. This property of $\boldsymbol{E}$ allows the application of the Helmholtz theorem (e.g. Arfken and Weber 1995), which implies the decomposition of a vector field into a irrotational and a solenoidal component (Glassmeier 1995). According to this, the electric field can be expressed in terms of a scalar potential Φ and a vector potential $\boldsymbol{\Psi}$. The former can be understood as the potential corresponding to the electric field of an Alfvén wave in a homogeneous plasma, while both the fast and the slow magnetosonic mode are represented by $\boldsymbol{\Psi}$. Thus, in the case of an inhomogeneous plasma the electric field is given by (e.g. Leonovich and Mazur 1993)

$$\boldsymbol{E} = -\nabla_\perp \Phi + \nabla_\perp \times \boldsymbol{\Psi}, \ \ \boldsymbol{\Psi} = (0, 0, \Psi_\theta), \tag{2.9}$$

where the transverse Nabla-operator is defined as $\nabla_\perp = (\partial/\partial L, \partial/\partial \phi, 0)$. Similar to the homogeneous case the functions Φ and $\Psi = \Psi_\theta$ describe Alfvén mode and the magnetosonic mode, respectively. Using Eqs. 2.8 and 2.9 the momentum equation 2.6 can be rewritten in two equations in terms of the functions Φ and Ψ (e.g. Klimushkin 1998a, Klimushkin et al. 2004):

$$\hat{L}_A\Phi + \hat{L}_C\Psi = 0 \tag{2.10}$$

and

$$\hat{L}_F\Psi + \hat{L}_C^+\Phi = 0, \tag{2.11}$$

where $\hat{L}_C^+$ is the Hermitian conjugate to $\hat{L}_C$. The so called Alfvén operator $\hat{L}_A$ is related to magnetospheric Alfvén waves including the polarization splitting of these waves into toroidal and poloidal modes:

$$\hat{L}_A = m^2\hat{L}_P(\omega) - \frac{\partial}{\partial L}\hat{L}_T(\omega)\frac{\partial}{\partial L}. \tag{2.12}$$

The operator $\hat{L}_T$ represents the toroidal mode by

$$\hat{L}_T(\omega) = \frac{\partial}{\partial l}p\frac{\partial}{\partial l} + p\frac{\omega^2}{V_A^2} \tag{2.13}$$

and the operator $\hat{L}_P$ is related to the poloidal mode by

$$\hat{L}_P(\omega) = \frac{\partial}{\partial l}\frac{1}{p}\frac{\partial}{\partial l} + \frac{1}{p}\left(\frac{\omega^2}{V_A^2} + \eta\right) \tag{2.14}$$

with

$$\eta = -\frac{2}{R}\left(\mu_0\frac{J_0}{B_0} + \frac{2}{R}\frac{V_S^2}{V_A^2}\right). \tag{2.15}$$

Here the local parameter are $V_A = B_0/\sqrt{\mu_0\rho_0}$ the Alfvén velocity, $V_S = \sqrt{\gamma P_0/\rho_0}$ the plasma sound velocity and R the curvature radius of a field line. Both operators $\hat{L}_T$ and $\hat{L}_P$ exhibit the same mathematical structure. In Eq. 2.14 the additionally occurring parameter η provides for the difference between the toroidal and the poloidal mode, which is explained in more detail in Sec. 2.2. Furthermore, the quantity p is defined as

$$p = \sqrt{\frac{g_2}{g_1}} = L\sqrt{1 + 3\sin^2\theta}, \tag{2.16}$$

that is related to a geometric property of magnetic field lines. Assuming the cross section of a thin magnetic flux tube have the physical size $\sqrt{g_1}dx_1 \cdot \sqrt{g_2}dx_2$. The function p describes the variation of the ratio $\sqrt{g_2}dx_2/\sqrt{g_1}dx_1$ along the flux tube, i.e. the ratio of the azimuthal size to the radial size of the tube that is only able to vary in a magnetic field with curved field lines (Leonovich and Mazur 1990). Similar to the curvature radius R the function p is largest at the end of the field line and lowest in the equatorial plane $\theta = 0$.

The operator $\hat{L}_C$ in Eq. 2.10 describes the coupling between the fast magnetosonic mode and the Alfvén mode in an inhomogeneous plasma:

$$\hat{L}_C = im\left(\frac{\partial}{\partial L}\frac{\omega^2}{V_A^2} + \frac{\partial}{\partial L}\frac{\partial}{\partial l}p\frac{\partial}{\partial l}\frac{1}{p} - \frac{\partial}{\partial l}\frac{1}{p}\frac{\partial}{\partial l}p\frac{\partial}{\partial L} - \eta\frac{\partial}{\partial L} - \frac{\sqrt{g_3}}{\sqrt{g_2}}\frac{R\eta}{2}\Delta_\perp\right) \tag{2.17}$$

with the transverse Laplacian

$$\Delta_\perp = \frac{\partial}{\partial L}p\frac{\partial}{\partial L} - m^2\frac{1}{p}.$$

The operator $\hat{L}_F$ in Eq. 2.11 describes the structure of the fast magnetosonic wave in the magnetosphere and $\hat{L}_C^+$ gives the back influence of an Alfvén wave on the fast magnetosonic mode (Klimushkin et al. 2004). Further investigations on the propagation region of this wave type are done by e.g. Lee (1996) and Leonovich and Mazur (2001). They have discovered that for low frequencies and high azimuthal wave lengths the fast magnetosonic waves are narrowly localized near the magnetopause. As the main concern of this work is on magnetospheric Alfvén waves, we can concentrate on Eq. 2.10 that includes the fast magnetosonic wave as a source. In case of a azimuthally small scaled Alfvén wave ($m \gg 1$) in a plasma with a finite but small plasma pressure ($\beta \ll 1$) a relation between the functions Φ and Ψ is obtained comparing Eqs. 2.10 and 2.17:

$$\Delta_\perp\Psi = im\frac{R\eta}{2}\Phi. \tag{2.18}$$

Hence, investigating poloidal Alfvén waves in the magnetosphere permits to neglect the function Ψ compared to Φ, as it follows from Eq. 2.18 that $\Psi \sim \beta m^{-1}\Phi \ll \Phi$ (Klimushkin

1998b). The physical interpretation of this relation is the well accepted fact that poloidal field line oscillations are not excited by the coupling with a fast magnetosonic mode, i.e. by the process of field line resonance. On these conditions Eq. 2.10 reduces to the differential equation

$$m^2 \hat{L}_P(\omega)\Phi - \frac{\partial}{\partial L}\hat{L}_T(\omega)\frac{\partial}{\partial L}\Phi = 0. \tag{2.19}$$

The solution Φ of this homogeneous differential equation giving the spatial structure of the Alfvén wave field was described extensively by Leonovich and Mazur (1993) for a cold plasma. Their method presented is in principle also applicable with respect to a warm plasma (Klimushkin 1997, 1998a,b). However, in both cases the homogeneous character of the differential equation avoids implementing a source of the oscillation (Leonovich and Mazur 1997). This deficit can be removed by changing Eq. 2.19 to an inhomogeneous differential equation, where a source term q is introduced:

$$m^2 \hat{L}_P(\omega)\Phi - \frac{\partial}{\partial L}\hat{L}_T(\omega)\frac{\partial}{\partial L}\Phi = q. \tag{2.20}$$

This equation will be used to explore in detail the spatial structure of magnetospheric field line oscillations in Sec. 3 and possible sources of these waves will be discussed in Sec. 4.

2.2 Difference between poloidal and toroidal modes

Both types of standing field line oscillation in the magnetosphere feature perturbations transverse to the magnetic field. Due to the radial dependencies of the plasma background parameters, such as magnetic field strength B_0, plasma pressure P_0 and density ρ_0, the toroidal and poloidal mode exhibit different characteristics regarding their oscillation behaviour. Mathematically these difference between both wave modes emerge from the term η of the poloidal operator $\hat{L}_P$ (Eq. 2.14) comparing with the toroidal operator $\hat{L}_T$ (Eq. 2.13). The definition of η in Eq. 2.15 implies that the poloidal mode is in particular effected by field line curvature and plasma pressure.

In general the plasma pressure influences both the toroidal and the poloidal mode, because $\hat{L}_T$ as well as $\hat{L}_P$ include the coefficients of the metric tensor that are affected by the equilibrium condition $\boldsymbol{J}_0 \cdot \boldsymbol{B}_0 = 0$, i.e. the coefficients depend on the derivative the of pressure along the radial coordinate (Klimushkin et al. 2004). However, the poloidal mode is expected to be stronger affected by a radial gradient in the plasma pressure, as its magnetic field is perturbed in the radial direction. In this case the poloidal oscillation causes a pressure perturbation, which in fact does not interact with the poloidal Alfvén wave (e.g. Walker and Pekrides 1996). From this it follows that even in a non-cold plasma with $\beta \ll 1$ the poloidal mode has the character of an Alfvén wave when the field parallel component of the magnetic field oscillation $b_\parallel$ is much smaller than the radial component b_r. The magnetic field of the toroidal mode oscillates in azimuthal direction, in which the equilibrium parameters are assumed to be constant, and is exempt from perturbation of the plasma pressure. Consequently, due to the existence of a radial gradient in the plasma pressure each type of wave mode receives a different strength of the restoring force, so that toroidal and poloidal Alfvén waves oscillate with different frequencies. This phenomena is referred to as polarization splitting of Alfvén waves, that occurs even in a straight field line configuration (e.g. Klimushkin 1997).
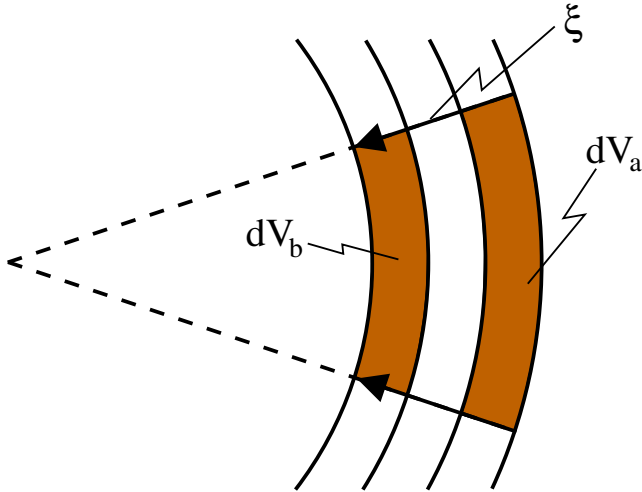
Figure 2.2: Effect of a poloidal wave in curved magnetic field on flux tube volume, adapted from Southwood and Saunders (1985). The arrows denote the displacement vectors $\boldsymbol{\xi}$, the continuous lines are magnetic field lines. The colored areas are flux tube elements. The dashed lines cross in the center of curvature.

A more realistic treatment of toroidal and poloidal Alfvén waves requires considering the curvature of the magnetospheric field lines. Qualitatively, field line curvature influences a poloidal Alfvén wave via coupling with a slow magnetosonic wave (e.g. Southwood and Saunders 1985, Walker 1987). This slow mode exhibits a compressible perturbation of the magnetic field as its plasma displacement $\boldsymbol{\xi}_{SM}$ has a component parallel to $\boldsymbol{B}_0$. Contrary, the plasma displacement $\boldsymbol{\xi}_A$ of an Alfvén wave is perpendicular to $\boldsymbol{B}_0$. This implies that in a straight field line configuration the coupling between Alfvén and slow mode is impossible, because the Alfvén wave does not cause any field parallel pressure perturbations (e.g. Walker 1987). The situation is different in a curved magnetic field configuration, such as the terrestrial dipole field. Also in this case the condition $\boldsymbol{\xi}_A \perp \boldsymbol{B}_0$ holds, but if field lines are bent the poloidal perturbation leads to a change in the volume occupied by the plasma on a flux tube (Southwood 1972), which is illustrated in Fig. 2.2. As consequence the plasma displacement due to the Alfvén mode, which in fact does not change the total magnetic field $\boldsymbol{B}_0$, modifies the plasma pressure and vice versa, i.e. coupling between a poloidal Alfvén wave and a compressible slow mode occurs (Southwood and Saunders 1985). It is obvious that the interaction of these wave modes becomes stronger with increasing curvature. Furthermore the presence of a finite plasma pressure amplifies this effect, because coupling efficiency of a poloidal Alfvén mode with a slow mode is proportional to the ratio V_{SM}/V_A, where V_{SM} is the slow mode velocity (e.g. Walker and Pekrides 1996). In summary the coupling efficiency of a poloidal Alfvén with a slow mode,

and thus the difference between poloidal and toroidal mode, is proportional to β/R.

2.3   Field line eigenfrequencies

Magnetospheric pulsations investigated in the present work are standing field line oscillations caused by oppositely propagating Alfvén waves. The eigenfrequencies ω_A of these standing waves depend primarily on the length of the field lines l in the region of excitation and the Alfvén wave velocity V_A. Magnetic field and plasma density, and thus also the Alfvén velocity, depend on the coordinate along the field line, so that the Alfvénic travel time approximation is required to estimate ω_A (e.g. Warner and Orr 1979):

$$\omega_A = \frac{2\pi N}{T_A}, \quad T_A = 2 \int_S^N \frac{dl}{V_A},$$
(2.21)

where N is the latitudinal harmonic number, T_A the eigenperiod and dl an increment of length. The integration limits are the northern and the southern ionospheres.

The values of ω_A determined by Eq. 2.21 approximate the real eigenfrequencies, because this expression for ω_A is valid for an "ideal" Alfvén wave, which is, strictly speaking, only given by a toroidal mode in a cold plasma with straight magnetic field lines. As exposed in the previous section, plasma β and field line curvature effect both the poloidal and the toroidal mode significantly, where the influence on the poloidal mode is stronger. Accordingly, under realistic conditions for magnetospheric oscillations the field line eigenfrequencies, firstly, differ from ω_A of Eq. 2.21 and, secondly, are different for the toroidal and poloidal mode, respectively.

In general the field line eigenfrequencies are the solutions of an eigenvalue problem given by the linearized differential equation describing the perturbations e.g. of the wave electric field (e.g. Cummings et al. 1969, Southwood and Hughes 1983, Walker 1987). In doing so one aims for the solution of Eq. 2.19 representing an Alfvén wave modified by the influence of the plasma inhomogeneity (Klimushkin 1998b). This equation is, in view of a poloidal mode represented by $m \gg 1$, dominated by the term $m^2 \hat{L}_p \Phi$, whereas for the toroidal mode with $m \ll 1$, Eq. 2.19 is dominated by $-(\partial/\partial L)\hat{L}_T(\partial/\partial L)\Phi$. That means the wave equation is decoupled in poloidal and toroidal mode (e.g. Dungey 1967, Radoski 1967). Within these two limiting cases the eigenvalue problem is simplified to

$$\hat{L}_P(\omega)\Phi = 0$$
(2.22)

for the poloidal mode and

$$\hat{L}_T(\omega)\Phi = 0$$
(2.23)

for the toroidal mode (Mager and Klimushkin 2002). As the wave electric field E vanishes at the footprints of the oscillating field lines at the ionosphere, a boundary condition for Eq. 2.22 and 2.23 can be formulated as

$$\Phi(\theta = \theta_N) = \Phi(\theta = \theta_S) = 0,$$
(2.24)

where θ_N and θ_S denote the position of intersection of field line and ionosphere (e.g. Leonovich and Mazur 1993). By changing the variable l to θ in Eqs. 2.13 and 2.14 the

toroidal and poloidal equations can be rewritten in the following form:

$$\frac{V_A^2}{h_\theta^2}\frac{\partial^2\Phi}{\partial\theta^2} + \frac{V_A^2}{ph_\theta}\frac{\partial}{\partial\theta}\left(\frac{p}{h_\theta}\right)\frac{\partial\Phi}{\partial\theta} = -\omega^2\Phi \qquad (2.25)$$

and

$$\frac{V_A^2}{h_\theta^2}\frac{\partial^2\Phi}{\partial\theta^2} + \frac{V_A^2 p}{h_\theta}\frac{\partial}{\partial\theta}\left(\frac{1}{ph_\theta}\right)\frac{\partial\Phi}{\partial\theta} + V_A^2\eta\Phi = -\omega^2\Phi. \qquad (2.26)$$

The eigenvalues ω of the above differential equations are the desired field line eigenfrequencies. In the following the toroidal eigenfrequencies are denoted as Ω_T and the poloidal eigenfrequencies Ω_P. Details about the method applied to solve Eqs. 2.25 and 2.26 in order to determine the radial distribution of $\Omega_T(L)$ and $\Omega_P(L)$ are given in Sec. 6.1.

As evident from the discussion in Sec. 2.2 the response of the poloidal mode to field line curvature and plasma pressure is distinct from the response of the toroidal mode. This implies also differences between the corresponding poloidal and toroidal eigenfrequencies due to the different restoring forces acting on each mode. A parameter defining this difference is the radial distance between the L shells, where Ω_P and Ω_T, respectively, are equal to the wave frequency ω, as illustrated in Fig. 2.3. These L shells are called poloidal surface L_P and toroidal surface L_T (Leonovich and Mazur 1993). The radial distance is then given by $\Delta_N = L_T - L_P$, where the index N specifies the dependency of the distance on the longitudinal harmonic number N of the field line oscillation. Assuming that Δ_N is much smaller that a typical scale size a of the magnetosphere the distance between poloidal and toroidal surface is approximately (Klimushkin et al. 2004)

$$\Delta_N \sim a\frac{\Omega_T^2 - \Omega_P^2}{\Omega_T^2}. \qquad (2.27)$$

It will be shown in Sec. 3 that the area of wave activity in the radial direction is confined by the surfaces L_T and L_P. This region of the width Δ_N is transparent for the radially propagating Alfvén mode and is, thus, referred to as wave transparency region.

The numerical solution of Eqs. 2.25 and 2.26 yield to the precise values of the eigenfrequencies Ω_T and Ω_P. However, more descriptive information about the difference between both oscillations can be obtained by the application of the WKB approximation in the longitudinal direction on the electric field perturbation (Klimushkin 1998a). The longitudinal WKB approximation is, strictly speaking, only valid, if the field parallel scale of the wave is very small or, in other words, the harmonic number of the wave is $N \gg 1$. Appropriate results, correct by the order of magnitude, are nevertheless expected also for $N \geq 1$. Within this limitation the toroidal eigenfrequency is given by Eq. 2.21, i.e. $\Omega_T = \omega_A$, and the poloidal eigenfrequency is expressed by (Klimushkin 1998a)

$$\Omega_P = \Omega_T - \frac{1}{N}\int_S^N V_A\frac{\partial^2}{\partial l^2}(\ln p)\,dl - \frac{1}{N}\int_S^N V_A\eta\,dl. \qquad (2.28)$$

The second term of Eq. 2.28 depends mainly on the geometry of the field line represented by the parameter $p(l) = \sqrt{g_2(l)/g_1(l)}$, while the parameter η of the third term is proportional to the plasma β (Eq. 2.15). Apparently, in a cold plasma with $\eta = \beta = 0$ the field line curvature causes a reduction of the poloidal eigenfrequency compared to the toroidal one leading to $\Delta_N > 0$.
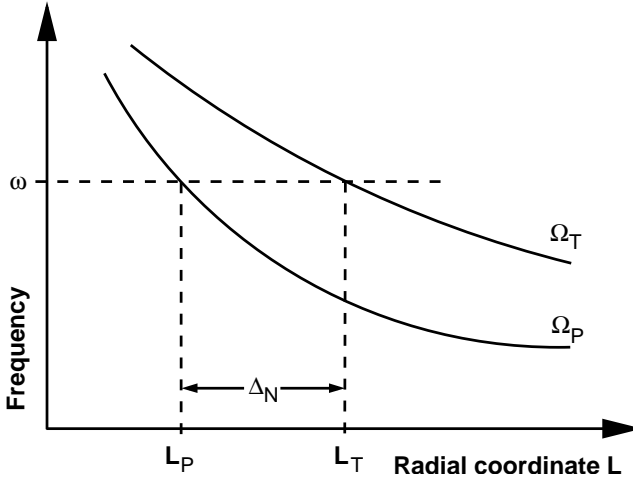
Figure 2.3: Positions of the poloidal and toroidal surfaces, after Klimushkin et al. (2004).

Note that in a straight field line configuration both types of eigenfrequencies coincide even when the plasma is warm, because in this case the parameter η is zero due to the infinite curvature radius R. This fact is reflected in the WKB approximation (see Eq. 2.28) as well as in the poloidal eigenvalue problem Eq. 2.26, where the latter is equal to the toroidal eigenvalue problem Eq. 2.25 when $\eta = 0$ and $p = 1$.

The appearance of finite plasma pressure in a curved magnetic field makes both $\Omega_T > \Omega_P$ and $\Omega_T < \Omega_P$ possible depending on the sign of the parameter η. Bearing in mind the definition of η in Eq. 2.15 three different scenarios may occur:

1. The magnetospheric ring current flows westward, i.e. $J_0 < 0$, and additionally $|\mu_0 J_0/B_0| > 2V_S^2/(RV_A^2)$ holds. That means η is dominated by the ring current. In this case one has $\eta > 0$.

2. When $J_0 < 0$ but the plasma β has a greater impact than the ring current, i.e. $|\mu_0 J_0/B_0| < 2V_S^2/(RV_A^2)$, one also has $\eta < 0$.

3. An eastward flowing ring current, i.e. $J_0 > 0$, always leads to $\eta < 0$.

In the first case the reduction of Ω_P compared to Ω_T is further enhanced leading to increased values of Δ_N. Contrary, in the scenarios 2 and 3 the poloidal eigenfrequency Ω_P can exceed Ω_T, if the third term of Eq. 2.28 becomes larger than the second one, which results in $\Delta_N < 0$. This requirement is fulfilled easily under the discussed background conditions, curved field lines and warm plasma, as η also depends on the curvature $(1/R)$.

Under quiet solar activity conditions the three scenarios emerge in different magnetospheric regions. The first one may occur in outer regions of the magnetosphere beyond the
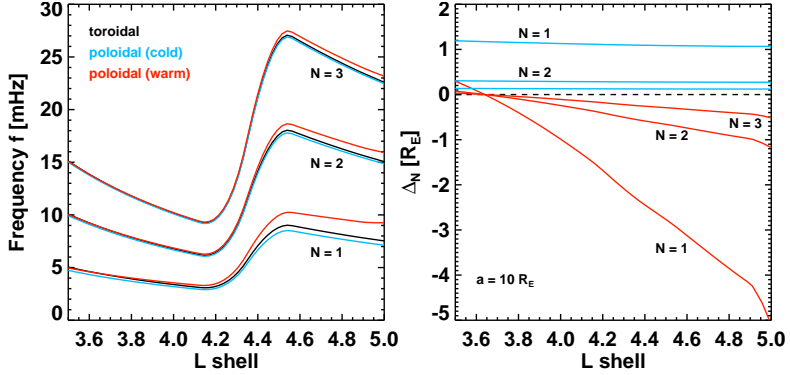
Figure 2.4: Radial distributions of the toroidal eigenfrequencies (black lines), the poloidal eigenfrequencies in a cold plasma (blue lines) and in a warm plasma (red lines) in the region of the plasmasphere for the first three longitudinal harmonics (left). The resulting widths of the wave transparency region Δ_N, displayed on the right, are calculated using Eq. 2.27 with a magnetospheric scale size of $a = 10\,R_E$.

plasmapause, where the ring current density reaches its maximum (e.g. Cheng 1992). The second case is expected to be found where the ring current density is low and the plasma β increases. As this configuration can appear near the plasmapause, this scenario is of main interest for this work and will be discussed in more detail in Sec. 3. A schematic picture of Ω_T, Ω_P in a cold plasma and Ω_P influenced by a finite plasma β in this region is shown in Fig. 2.4. An eastward directed ring current is expected deep inside the plasmasphere, but in this region the plasma β is close to zero when the solar activity is low (e.g. Cheng 1992). Consequently, in this case the parameter η is too small and the third term in Eq. 2.28 cannot compensate the second one and the Ω_P remains smaller than Ω_T. Further possible configurations, especially considering strong solar activity, are discussed in Klimushkin et al. (2004).

As evident from Eq. 2.28 the difference $\Omega_T - \Omega_P$ decrease with increasing longitudinal harmonic number N. Consequently, following Eq. 2.27 the higher N is the smaller is the distance Δ_N between the poloidal and toroidal surfaces. As a first approximation for the first harmonic $N = 1$ the distance Δ_N is about 0.5 R_E, whereas for $N = 2$ the distance is $\Delta_N \approx 0.05\,R_E$ (Klimushkin et al. 2004).

It should be emphasized that considerations made in this section are appropriate only when considering a plasma with $\beta \ll 1$. A simple relation was found by Klimushkin (1998b) allowing to verify if the finiteness of the plasma pressure has a major impact on the poloidal eigenfrequency Ω_P:

$$\beta > \frac{\Delta_N}{L}. \tag{2.29}$$

Using a typical radial distance of $L = 5\,R_E$ and the above mentioned values for Δ_N one find that a plasma β value of approximately 0.1 must be taken into account for $N = 1$ and

all higher harmonics. Even if $\beta \approx 0.01$ the finite pressure becomes important for $N = 2$ and higher harmonics (e.g. Leonovich and Mazur 1993, Klimushkin et al. 2004).

3   Radial structure of magnetospheric Alfvén waves

In the previous section it was elaborated that the difference between toroidal and poloidal eigenfrequencies is caused by field line curvature and amplified by finite plasma pressure. In the assumed axisymmetric magnetosphere this polarization splitting takes place in the radial direction. For this reason differences in the radial profiles of Ω_T and Ω_P lead to several characteristic spatial structures of magnetospheric Alfvén waves, which will be investigated in this section.

In general the radial and field aligned structure of an Alfvén wave field is represented by the Alfvén potential $\Phi = \Phi(L, \theta, \omega)$ representing the solution of the inhomogeneous differential equation 2.20. Following a general approach of perturbation theory the Alfvén potential Φ can be written as (Leonovich and Mazur 1997)

$$\Phi = R_N(L, \omega) T_N(L, \theta, \omega) + \delta\Phi_N. \tag{3.1}$$

The function $\delta\Phi_N$ is a small perturbation of the Alfvén potential considering small differences between toroidal and poloidal mode in their field aligned structure. The function $R_N(L)$ represents the small scale changes of the radial structure, as the Alfvén wave is narrowly localized across magnetic shells. Contrary, $T_N(L, \theta)$ gives the large scale structure of the solution, coinciding by order of magnitude with the length of magnetospheric field lines. Its dependency on the radial coordinate L is assumed to be much weaker than the function R_N changes with L (Leonovich and Mazur 1993). This construction of Φ reproduces properties of standing Alfvén waves, namely that the characteristic field aligned scale size is much larger than the radial scale size.

Substituting the ansatz Eq. 3.1 into Eq. 2.20 results in the following differential equation for the wave radial structure described by the function $R_N(L, \omega)$ (Leonovich and Mazur 1997, Klimushkin et al. 2004):

$$\frac{\partial}{\partial L}(\omega^2 - \Omega_{TN}^2)\frac{\partial}{\partial L}R_N - k_\phi^2(\omega^2 - \Omega_{PN})R_N = q_N \tag{3.2}$$

with

$$q_N = \int_S^N T_N q \, dl.$$

The variable k_ϕ corresponds to the azimuthal component of the wave vector in the equatorial plane $k_\phi = m/L$ (Leonovich and Mazur 1993). Solving Eq. 3.2 is possible in two limiting cases depending on the ratio of radial and azimuthal scale size of the wave field. An

appropriate parameter describing this ratio is the number of azimuthal wavelengths ν_N fitting into the radial scale size given by the distance Δ_N between the poloidal and the toroidal surface (Leonovich and Mazur 1997):

$$\nu_N \equiv k_\phi \Delta_N. \tag{3.3}$$

With the approximation of Δ_N in Eq. 2.27 and assuming the magnetospheric scale size a is by the order of magnitude comparable with the distance L of the wave field from the Earth, the the parameter ν_N can be written as:

$$\nu_N \sim m\frac{\Omega_{TN}^2 - \Omega_{PN}^2}{\Omega_{TN}^2}. \tag{3.4}$$

If $\nu_N \ll 1$ the radial wavelength of the Alfvén wave is much smaller that the azimuthal wavelength indicating a toroidal oscillation, whereas if $\nu_N \gg 1$ the azimuthal wavelength is larger than the radial one indicating a poloidal oscillation. It is remarkable that according to Eq. 3.4 a toroidal wave polarization can also be realized for large values of m in case the difference $\Omega_P^2 - \Omega_T^2$ is sufficiently small. In other words, the poloidality of an oscillation is assured only if the polarization splitting is significant. Obviously, the parameter ν_N is a more rigorous criteria than the azimuthal wave number m to distinguish between toroidal and poloidal Alfvén waves (Mager and Klimushkin 2002).

3.1 Localization of toroidal mode

In the case $\nu_N \ll 1$ the difference between poloidal and toroidal eigenfrequencies must be very small (see Eq. 3.4). In other words the difference between the poloidal and toroidal surface can be neglected ($L_T \approx L_P$) and field line curvature becomes unimportant. In this case the wave structure coincides with the well known wave field of a toroidal Alfvén wave excited by a field line resonance. Assuming that Ω_T and Ω_P are monotonically decreasing one can use Eq. 2.27, so that Eq. 2.20 becomes (Klimushkin et al. 2004):

$$\frac{\partial}{\partial L}(L - L_T)\frac{\partial}{\partial L}R_N - k_\phi^2(L - L_T)R_N = q_N\frac{a}{\omega^2}. \tag{3.5}$$

The solution of Eq. 3.5 can be written in terms of modified Bessel functions and is shown in Fig. 3.1. It is characterized by a logarithmic singularity at L_T, so that

$$R_N \propto \ln(\omega^2 - \Omega_T^2). \tag{3.6}$$

This singularity is a distinctive property of Alfvén resonance. Consequently, Eq. 3.5 describes the process of field line resonance.

3.2 Wave structure near boundaries of the transparency region

The condition $\nu_N \gg 1$ can be achieved by the presence of field line curvature resulting in a significantly large distance between the poloidal and the toroidal surface. Leonovich and
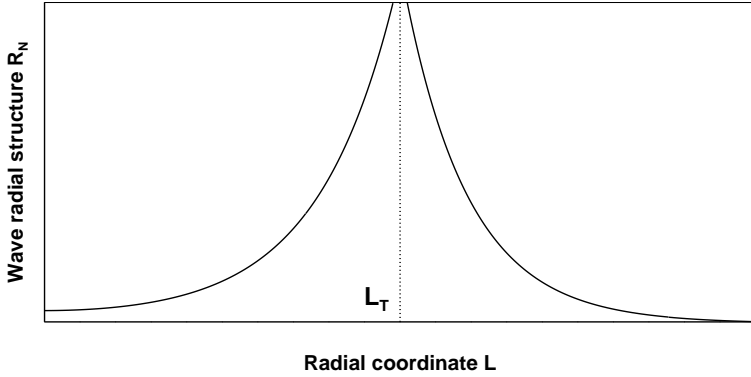
Figure 3.1: Radial structure of the localized toroidal mode. The dotted line marks the toroidal surface L_T, where resonance occurs and the wave amplitude is characterized by a singularity.

Mazur (1993) has demonstrated that when $\Delta_N > 0$ the radial structure R_N of the wave field is divided in three regions, near each of the surfaces L_P and L_T and between these surfaces. Their calculations are valid only, if the radial profile of the eigenfrequencies $\Omega_T(L)$ and $\Omega_P(L)$ is monotonically decreasing or increasing. Without loss of generality it is here assumed that the eigenfrequencies are decreasing and that $\Omega_T > \Omega_P$, which is tantamount to that the toroidal surface is located at a higher radial distance than the poloidal surface. This situation is reflected by Fig. 2.3.

At first we concentrate on the wave radial structure in the vicinity of the toroidal surface. In this region a solution of Eq. 3.2 has to be found under the condition $|L - L_T| \ll \Delta_N$. Using the substitution

$$z_T = \frac{L - L_T}{\lambda_T} \tag{3.7}$$

Eq. 3.2 is transformed to a zero-order Bessel equation, whose solution has the form (Leonovich and Mazur 1993)

$$R_N \propto K_0\left(2\sqrt{z_T}\right). \tag{3.8}$$

The function K_0 is the zero-order modified Bessel function and $\lambda_T = \Delta_N v_N^{-2}$ is the characteristic wavelength near the toroidal surface.

Similar to the localized toroidal mode discussed in Sec. 3.1 at $L = L_T$ the wave structure is characterized by a logarithmic singularity, which in both cases prohibit a physical description of the complete wave structure. In general such an infinite behaviour of resonance can be avoided by considering a small sink of energy. Concerning magnetospheric ULF pulsations this role is played by the dissipation of wave energy at the ionosphere due to its finite conductivity (e.g. Southwood 1974). Introducing a complex wave frequency $\omega^* = \omega + i\gamma$ the radial structure near the resonance surface is given by

$$R_N \propto \ln\left[(\omega + i\gamma)^2 - \Omega_T^2\right]. \tag{3.9}$$

The damping decrement γ is assumed to be small compared to the frequency ω indicating a high ionospheric conductivity (see details in Sec. 4.3). Now the function R_N has a finite value at $L = L_T$ and the radial wave structure is characterized by a sharp maximum around the resonant field line, where the characteristic scale size produced by the ionospheric damping is defined by (e.g. Southwood and Hughes 1983)

$$\sigma_{res} = \left| \frac{d\Omega_T}{dL} \right|^{-1}. \tag{3.10}$$

Such a small scaled pattern is associated with a large radial component of the wave vector k_r. Leonovich and Mazur (1993) have determined that k_r behaves as

$$k_r^2 \propto \frac{k_\phi^2}{\omega^2 - \Omega_T^2}, \tag{3.11}$$

if $L \approx L_T$. In view of the singularity arising in Eq. 3.8 the expression Eq. 3.11 shows mathematically that $k_r \rightarrow \infty$ at the resonance. On that account this surface L_T is denoted as resonance surface.

Near the poloidal surface, i.e. $|L - L_P| \ll \Delta_N$, the substitution

$$z_P = \frac{L - L_T}{\lambda_P} \tag{3.12}$$

with the characteristic poloidal wavelength $\lambda_P = \Delta_N \nu_N^{-2/3}$ turns Eq. 3.2 to an inhomogeneous Airy equation (Leonovich and Mazur 1993). The solution is given by

$$R_N(z_P) = i q_N k_\Phi^2 \Delta_N \int_0^\infty \exp\left(itz_P - \frac{it^3}{3} \right) dt. \tag{3.13}$$

A comparable form of such an Airy function is also known from the concept of the field line resonance process, where it describes a radially inward propagating fast mode that is reflected at a wave turning point (e.g. Southwood 1974). In this picture the energy of the compressional wave can tunnel beyond the turning point towards a resonance shell, where mode coupling to an Alfvén wave takes place. In a similar manner Eq. 3.13 is associated with a propagating wave reflected at the poloidal surface L_P, where the wave vector component k_r is described by (Leonovich and Mazur 1993)

$$k_r^2 \propto k_\phi^2 \left(\omega^2 - \Omega_P^2 \right). \tag{3.14}$$

Because k_r is zero at the poloidal surface L_P and becomes imaginary, if $\Omega_P > \omega$ or $L_P > L$, respectively, the poloidal surface $L = L_P$ is denoted as wave turning point.

3.3 Global wave structure

In the previous section the profile of the function $R_N(L, \omega)$ was investigated in the vicinity of both the poloidal turning point and the toroidal resonance surface. A complete view on the radial structure of the wave field requires the knowledge of R_N sufficiently distant from these surfaces. If the width of the transparency region Δ_N is wide enough, so that a large

number of radial wavelengths fits into it, it is allowed to apply the WKB approximation to Eq. 3.2 in the radial coordinate L that yields to the following expression for the wave radial structure (Leonovich and Mazur 1993):

$$R_N(L, \omega) = C_T \left[k_\Phi^2 (L - L_P)(L_T - L) \right]^{-1/4} \exp \left\{ i \int_{L_P}^{L} k_r(L') dL' \right\}. \tag{3.15}$$

Combining the expression for the radial component of the wave vector k_r near L_T (Eq. 3.11) and L_P (Eq. 3.14), respectively, leads to a model expression that approximates k_r between the boundaries of the transparency region (Leonovich and Mazur 1993):

$$k_r^2 = k_\phi^2 \frac{\omega^2 - \Omega_P^2}{\Omega_T^2 - \omega^2}. \tag{3.16}$$

Fig. 3.2 displays the radial distribution of k_r and the entire profile of the radial function $R_N(L, \omega)$ composed of Eq. 3.8 valid near the resonance surface L_T, Eq. 3.13 valid near the turning point L_P and Eq. 3.15, which holds in the region $L_P < L < L_P$. The radial wave vector changes from $k_r = 0$ to $k_r = \infty$ within a region of the size Δ_N.

This behaviour of k_r results in a characteristic wave energy transport occurring in the transparency region, which can be obtained by investigating the wave group velocity given by

$$V_{g,L} = \left(\frac{\partial k_r}{\partial \omega} \right)^{-1} = \frac{\sqrt{\omega^2 - \Omega_P^2} \sqrt[3]{\Omega_T^2 - \omega^2}}{2\omega k_\Phi (\Omega_T^2 - \Omega_P^2)}. \tag{3.17}$$

As it was initially assumed that $\Omega_P < \Omega_P$, the group velocity is positive indicating the wave energy directed from the turning point towards the resonance surface. This direction of energy transport remains in the opposite case. If $\Omega_P > \Omega_P$, the group velocity $V_{g,L}$ becomes negative. However, L_P is then located radially farther out compared to L_T and the wave energy transport from the poloidal surface towards the toroidal surface can be accepted as the general situation (e.g. Klimushkin et al. 2004).

Comparing radial and azimuthal scale sizes of the Alfén wave field represented by the transverse components of the wave vector, k_r and k_ϕ, explains their relation to the wave polarization in the transparency region. In contrast to k_r the azimuthal component $k_\phi = m/L$ remains nearly constant, as Δ_N is assumed to be much smaller than the scale size of the magnetosphere. Consequently, at $L \approx L_P$ the wave is poloidal polarized and $k_\phi \gg k_r \approx 0$. At $L \approx L_T$ the wave polarization is toroidal and $k_\phi \ll k_r \approx \infty$. Furthermore both situations are possible for large azimuthal wave numbers m implying that toroidal wave polarization is also possible for a wave with a large azimuthal wave number m, as mentioned above.

In summary, if a poloidal wave is generated at the poloidal surface L_P, its energy propagates towards the toroidal surface L_P due to the radial dispersion caused by the increasing radial wave number, but the azimuthal wave number does not change.

3.4 Alfvén resonator

The picture of the global radial structure drawn in the previous section is valid only under the limitation of monotonically decreasing or increasing eigenfrequencies $\Omega_T(L)$ and $\Omega_P(L)$.
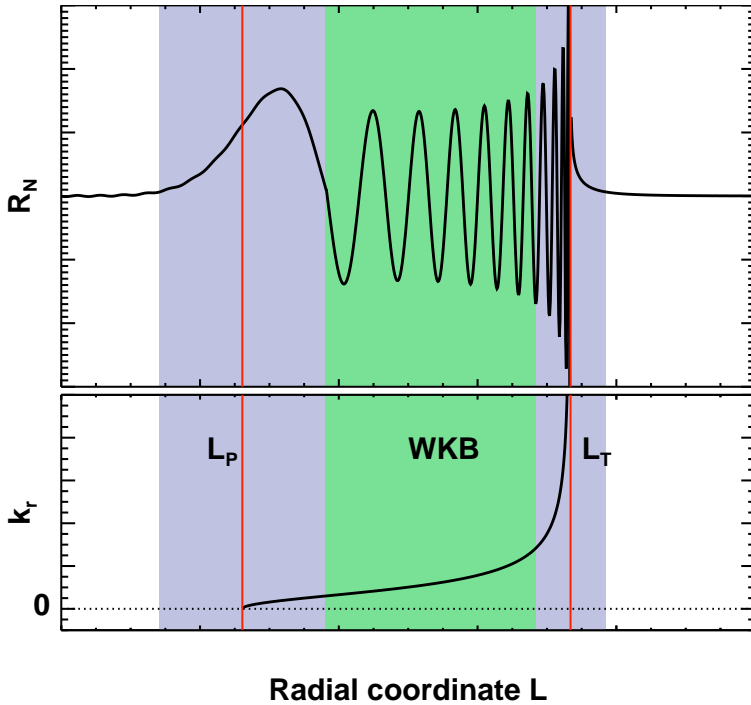
Figure 3.2: Upper panel: Radial structure R_N in wave transparency region (black line). Within the green shaded area the WKB approximation is valid, whereas it is not applicable in the vicinity of the surfaces L_T and L_T (red lines). Lower panel: Radial distribution of the wave vector component k_r approximated by Eq. 3.16.

This assumption is inappropriate in the vicinity of the terrestrial plasmapause, where the eigenfrequencies exhibit a maximum at the inner and a minimum at the outer edge of this boundary. According to this the radial structure of the wave field in this are is expected to differ clearly compared to the wave transparency region. Near extreme values of Ω_P the Alfvén wave field is confined by two poloidal turning points L_{P1} and L_{P2} and is called Alfvén resonator (see Fig. 3.3).

For the first time the possible existence of ULF pulsations in such a configuration was theoretically described by Vetoulis and Chen (1994) and Vetoulis and Chen (1996). However, in both publications an incompressible plasma is assumed neglecting in particular the interaction between the slow and the Alfvén mode (see Sec. 2.2). That means the effect of field line curvature was not incorporated and a finite plasma β was considered to be the only reason for a possible appearance of an Alfvén resonator. A more general approach was adopted by Leonovich and Mazur (1995), who discovered that poloidal turning points

may also emerges in a cold plasma due to the curvature induced polarization splitting between poloidal and toroidal mode.

At first view, one could assume that the radial structure in this configuration is represented by a double resonance due to the superposition of the solutions R_N close to the poloidal surfaces, which is assumed to be similar to R_N near L_P described by Eq. 3.13. However, at each turning point a wave would be generated with a group velocity directed radially towards the other poloidal surface. Such a wave traveling at the same time towards two oppositely located points cannot exist (e.g. Leonovich and Mazur 1995).

It was shown by Leonovich and Mazur (1995) and Klimushkin (1998a) that the radial structure inside the Alfvén resonator can be obtained from the solution R_N of the following differential equation:

$$\frac{d^2 R_N}{d\xi^2} + \left(\frac{\sigma^2}{\lambda_P^2} \frac{\omega^2 - \Omega_0^2}{\omega^2} - \xi^2\right) R_N = 0 \tag{3.18}$$

with

$$\lambda_R^2 = \sigma \frac{L_0}{m} \sqrt{\frac{\Omega_0^2 - \Omega_T^2}{\Omega_0^2}}, \tag{3.19}$$

where σ is a typical width of the resonator. This expression can be derived from Eq. 3.2 considering a parabolic distribution of $\Omega_P(L)$, as shown in Fig. 3.3, where Ω_0 is the minimum or maximum eigenfrequency depending on whether the resonator is located at the minimum or the maximum of Ω_P. With the characteristic radial wavelength λ_R of the poloidal wave the new coordinate $\xi = (L - L_0)/\lambda_R$ is introduced, where the extreme value of the eigenfrequency located at $L = L_0$. Furthermore the term q_N representing the wave source is assumed to be zero, so that Eq. 3.18 has the same form as the well known Schrödinger equation for the harmonic oscillator. Consequently, the wave frequency in the cavity close to the extremum of Ω_P is quantized as (Leonovich and Mazur 1995)

$$\omega_n^2 \equiv \Omega_0^2 \mp \Omega_0^2 \frac{\lambda_R^2}{\sigma^2} (2n + 1), \quad n = 0, 1, 2, \ldots. \tag{3.20}$$

The splitting of the eigenfrequencies depends on the ratio λ_r^2/σ^2 that in turn, considering Eq. 3.19, depends on the difference between the maximum poloidal eigenfrequency Ω_0 and the toroidal eigenfrequency Ω_T. As this difference decreases with the longitudinal harmonic number N (see Sec. 2.4), the eigenfrequency splitting is largest for the fundamental field line oscillation. Similar to the harmonic oscillator in quantum mechanics the required solution R_N is the product of a Hermitian polynomial $H_n(\xi)$ and a Gauss function:

$$R_N(\xi, \omega) \propto H_n(\xi) \exp\left(-\frac{\xi^2}{2}\right) \tag{3.21}$$

with the definition

$$H_n(\xi) = (-1)^n e^{x^2} \frac{d^n e^{x^2}}{d\xi^n}. \tag{3.22}$$

The resulting possible radial structure inside an Alfvén resonator is displayed in Fig. 3.3 for H_0, H_1 and H_2.

Considering ionospheric dissipation and a wave source q_n yields to an inhomogeneous differential equation and the radial structure is represented by a superposition of
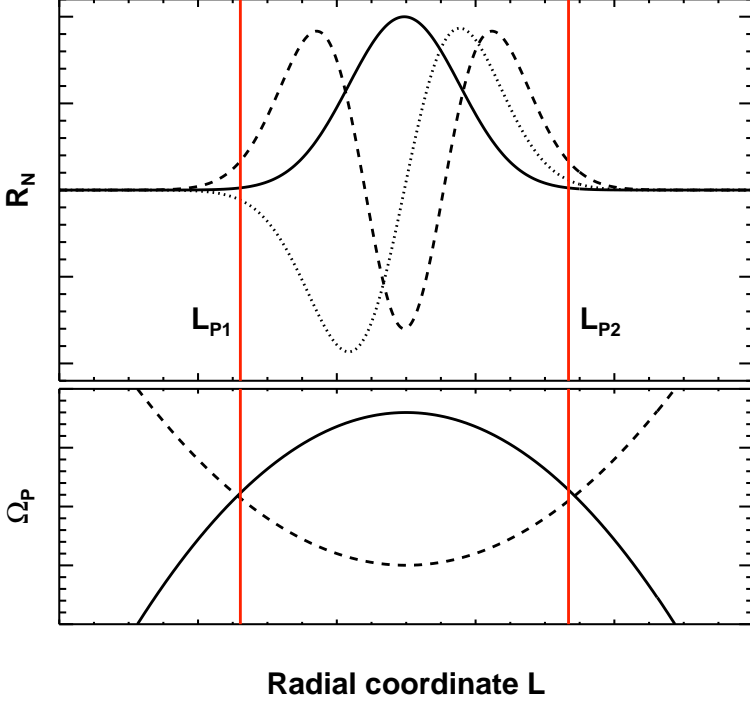
Radial coordinate L

Figure 3.3: Upper panel: Radial structure R_N of Alfvén wave field inside resonator between two poloidal turning points L_{P1} and L_{P2} for $n = 1, 2, 3$. Lower panel: Modeled poloidal eigenfrequency Ω_P at outer (solid line) and inner edge of the plasmapause (dotted line).

eigenmodes ω_n of the Alfvén resonator, which is expressed by (Leonovich and Mazur 1995)

$$Q_N(\xi, \omega) = \sum_{n=0}^{\infty} \frac{c_n}{(\omega + i\gamma)^2 - \omega_n^2} R_N(\xi) \qquad (3.23)$$

with

$$c_n = \int_{-\infty}^{\infty} R_N(\xi) q_N(L_P + \lambda_P \xi) d\xi. \qquad (3.24)$$

Thus, Eq. 3.23 describes a continuous spectrum of frequencies for the Alfén resonator. But its summand with $\omega \approx \omega_n$ obviously dominates all other terms, if additionally the difference $\omega - \omega_n$ and the damping decrement γ are smaller than the splitting of the eigenfrequencies $\Delta\omega_n$. In other words, in case the wave frequency ω is close to an eigenfrequency ω_n, the radial structure of the wave amplitude is well approximated by the function $R_N(\xi, \omega)$ given in Eq. 3.21 (e.g. Klimushkin et al. 2004).
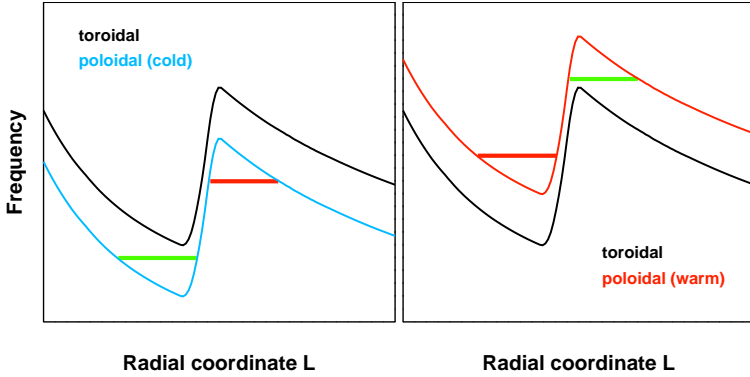
Figure 3.4: Possible locations of Alfvén resonator (green vertical lines) at plasmapause for cold plasma (left panel) and warm plasma (right panel). The vertical red lines mark areas bounded by two turning points, where the resonator cannot be excited.

In Fig. 3.4 poloidal and toroidal eigenfrequencies are displayed schematically for both the cold and the warm plasma in the vicinity of the plasmapause exhibiting the regions limited by two poloidal turning points L_P. As evident from this picture a further condition is required for the existence of a resonator, namely that the wave frequency ω must be situated between Ω_T and Ω_P. Otherwise, assuming that the wave is excited at a turning point where $\omega = \Omega_P$ holds, the wave energy would be transported towards the resonance surface $\omega = \Omega_T$, as described in Sec. 3.3. This behaviour is reflected by the the model expression Eq. 3.16 for the radial wave vector k_r that is valid obviously not only in the transparency region, but also inside the Alfvén resonator. Consequently, in a cold plasma when $\Omega_P < \Omega_T$, k_r becomes imaginary if $\omega < \Omega_P$, i.e. the Alfvén resonator cannot exist near the maximum of the field line eigenfrequencies. Considering a warm plasma with $\Omega_P > \Omega_T$ the resonator is not possible when $\omega > \Omega_P$, i.e. near the minimum of the eigenfrequencies. In these scenarios a wave cannot be radially trapped although the region is bounded by two turning points. In contrast to that Alfvén resonators are possible in a cold plasma near the minimum of eigenfrequencies and near the maximum when finite pressure has to be taken into account (e.g. Klimushkin 1998b).

3.5   Localization of wave phase jump

Next to its radial distribution of the amplitude modulation an Alfvén wave field additionally exhibits a characteristic profile of the wave phase. For instance, a well known feature of the field line resonance process is the jump in the wave phase across the resonance shell L_T. It was shown by Southwood (1974) that the wave polarization, i.e. the ratio of the radial (toroidal) component E_r of the electric field to the azimuthal (poloidal) component
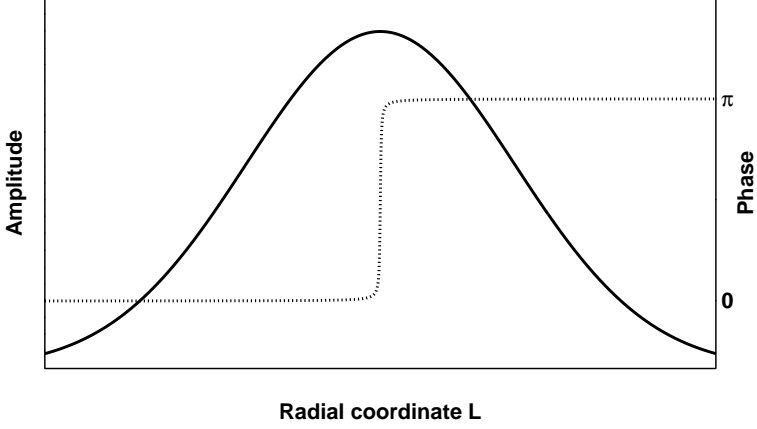
Figure 3.5: Radial profile of amplitude of the Alfvén wave field (solid line) inside a resonator for the eigenfrequency $\omega = \omega_1$ and its corresponding wave phase structure (dotted line).

E_ϕ, is given by

$$\frac{E_r}{E_\phi} = -\frac{i}{mE_\phi}\frac{\partial E_\phi}{\partial L}. \tag{3.25}$$

Due to the sharp amplitude maximum located at L_T, the sign of the term $\partial E_\phi/\partial r$ changes at the resonance shell corresponding to a narrowly localized change of the wave phase by 180°. The existence of this property of an Alfvén resonance was approved in ground based observations (e.g. Samson et al. 1971).

However, describing the wave polarization using Eq. 3.25 is not limited to the Alfvén resonance process. In general the electric field of an Alfvén wave can be expressed in terms of the potential Φ, so that $E_r = \partial\Phi/\partial L$ and $E_\phi = \partial\Phi/\partial\phi = -im\Phi$ (see Sec. 2.1) yielding to the expression

$$\frac{E_r}{E_\phi} = -\frac{i}{m\Phi}\frac{\partial\Phi}{\partial L}. \tag{3.26}$$

Assuming a Gaussian distribution of the wave radial structure $R_N(L, \omega)$, e.g. as displayed in Fig. 3.3, signifies that the radial distribution of the potential Φ given by Eq. 3.1 have a Gaussian character. Consequently, at the maximum of wave amplitude the term $\partial\Phi/\partial L$ has a change of sign which complies with a jump in the wave phase, similar to what is expected in a field line resonance (Klimushkin et al. 2004). Fig. 3.5 shows schematically the Gaussian character of R_N and the corresponding phase jump located at the amplitude maximum, which can be described by an arctan-function. Generally speaking, following Eq. 3.26, at each field line shell, where the radial amplitude distribution of an Alfvén wave field exhibits an extreme value, its phase is expected to change by 180°.

4 Temporal evolution of magnetospheric Alfvén waves

4.1 Temporal evolution inside the Alfvén transparency region

Using the simultaneous observation of four spatially separated satellites detecting a magnetospheric ULF pulsation allows under certain conditions the separation of spatial and temporal effects in the observed signal. Consequently, knowing details about the temporal evolution of an Alfvén wave field are essential for the interpretation of the observed data.

A simple approach to investigate the lifetime of a poloidal wave is the concept of field line phase mixing, where initially field line curvature, wave sources and sinks are ignored (e.g. Mann et al. 1995, Rickard and Wright 1995). In doing so the splitting of poloidal and toroidal eigenfrequency can be neglected. However, the wave frequency ω_A, e.g. determined by Eq. 2.21, still depend on the radial coordinate L and the radial (poloidal) component of the magnetic field disturbance may be expressed by

$$b_r(L,t) = A(L)\exp[-i\Omega_T(L)t], \tag{4.1}$$

where $A(L)$ represents the radial dependency of the wave amplitude. Defining the wave phase as $\Phi = -\Omega_T(L)t$ reveals that two neighboring field lines run out of phase in time as they oscillate with a slightly different frequency. At a certain time t' the radial structure of the wave field could be described by $b_r \propto \exp(ik_r L)$ with the slowly varying radial wave vector $k_r(L)$ (e.g. Wright et al. 1999a). From this follows by taking into account Eq. 4.1

$$ik_r = \frac{1}{b_r}\frac{\partial b_r}{\partial L} = i\frac{\partial \Omega_T}{\partial L}t + \frac{1}{A(L)}\frac{\partial A(L)}{\partial L}. \tag{4.2}$$

Assuming that the function $A(L)$ is, similar to k_r, almost constant in L, the radial component of the wave vector is given by

$$k_r \approx \frac{\partial \Omega_T}{\partial L}t. \tag{4.3}$$

Accordingly, due to phase mixing the radial wave length $\lambda_r = 2\pi/k_r$ decreases in time, i.e. the radial structure of the wave field evolves to smaller scale sizes. Considering the solenoidal constraint $\nabla \cdot \boldsymbol{b} = k_r b_r + k_\phi b_\phi + k_\| b_\| = 0$ reveals the temporal evolution of wave polarization, i.e. the ratio of radial and azimuthal wave amplitude b_r/b_ϕ. For magnetospheric standing waves the field parallel wavelength, which corresponds by the order of magnitude with the length of a field line, is much larger than the transverse

wavelengths, so that $k_\parallel b_\parallel \ll k_r b_r, k_\phi b_\phi$ holds even for nonzero $b_\parallel$. Hence with k_r given by Eq. 4.3 one can write

$$\frac{b_r}{b_\phi} \approx -\frac{k_\phi}{k_r} = -\frac{m}{L}\left(\frac{\partial \Omega_T}{\partial L}t\right)^{-1}. \qquad (4.4)$$

As the azimuthal wave vector $k_\Phi = m/L$ is constant in time, phase mixing entails the transformation of an initially poloidal polarized wave with $b_r \gg b_\phi$ and $k_r \ll k_\phi$ to a toroidal wave due to the increasing radial wave vector k_r. With Eq. 4.4 the lifetime τ of the poloidal wave can be defined as the time when the toroidal amplitude exceeds the poloidal one, i.e. $b_r = b_\phi$ (Mann and Wright 1995):

$$\tau \equiv \frac{m}{L}\left(\frac{\partial \Omega_T}{\partial L}t\right)^{-1}. \qquad (4.5)$$

Apparently, the stronger the radial gradient of the field line eigenfrequency ω_A the faster the radial scale size of the wave field reduces and the transformation process occurs from poloidal to toroidal polarization, respectively. After the onset of the field line oscillation at $t = 0$ the poloidal amplitude of the wave decreases immediately while the toroidal amplitude starts growing. When $t > \tau$ the toroidal amplitude dominates (Mann et al. 1997a,b).

Next to phase mixing the development of ULF pulsations in time is mainly triggered by the interplay of sources and sinks of the wave energy. Thereby magnetospheric instabilities are believed to be the origin of the waves, while finite ionospheric conductivity leads to wave damping. Details about these mechanism are described in Secs. 4.3 and 4.4. In general wave damping and growing are considered by introducing a complex wave frequency with the damping decrement γ and the growth rate δ. Then perturbed quantities are in general represented by

$$\boldsymbol{b}, \boldsymbol{E} \propto \exp\left[(-i\omega + \gamma - \delta)t\right]. \qquad (4.6)$$

Furthermore, field line curvature and the resulting polarization splitting have to be taken into account. In this section we are restricted to monotonically decreasing eigenfrequencies Ω_P and Ω_T, so that in the attendance of field line curvature the wave transparency region is bounded by a poloidal turning point L_P and a toroidal resonance point L_T (see Sec. 3.3). In this case wave damping and growing are incorporated into Eq. 3.2 leading to the following differential equation (e.g. Leonovich and Mazur 1999, Klimushkin and Mager 2004)

$$\frac{\partial}{\partial L}\left[L - L_T + i\sigma_{res}(\gamma - \delta)\right]\frac{\partial R_N}{\partial L} - k_\phi^2\left[L - L_T + i\sigma_{res}(\gamma - \delta)\right]R_N = q. \qquad (4.7)$$

Here the scale size σ_{res} is defined by Eq. 3.10. Considering the conditions $\sigma_{res}\delta/\Delta_N \ll 1$ and $\sigma_{res}\gamma/\Delta_1 \ll 1$, which coincides with the assumption that damping decrement and growth rate are small compared with the wave frequency. The source function q in Eq. 4.7 may be represented by a δ-function in time, i.e. the wave source is considered as a sudden impulse that is activated at the time $t = 0$ and immediately turns off. Furthermore the functions γ and δ are assumed to be frequency independent (Leonovich and Mazur 1999). Applying the Fourier-transformation on the solution of Eq. 4.7, which is the function $R_N = R_N(L, \omega)$, results in (Klimushkin and Mager 2004)

$$R_N = -\frac{2\pi}{k_\Phi^2\sqrt{1 + (t/\tau)^2}}\exp\left[i\Omega_T t + ik_\Phi \Delta_N \arctan\frac{t}{\tau} - \sigma_{res}k_\phi\gamma\frac{t}{\tau} + \sigma_{res}k_\phi\delta\arctan\frac{t}{\tau}\right] \qquad (4.8)$$

for $t > 0$, where now $R_N = R_N(L, t)$. This equation reflects the temporal evolution of a high-m Alfvén wave generated at the poloidal turning point L_P by a beam of particles, which is considered as a sudden impulse wave source. The characteristic time scale τ is on the order of magnitude given by Eq. 4.5. At times $t \leq \tau$ the wave amplitude is enhanced by the factor $\sigma_{res}k_\phi\delta \arctan(t/\tau)$. After that when $t > \tau$ the wave transforms from poloidal to toroidal due to phase mixing, which appears as the term $i\Omega_T(L)t$, as well as radial wave propagation caused by field line curvature represented by the second term of the exponential function in Eq. 4.8. Furthermore, the presence of a energy sink, e.g. ionospheric dissipation, induces the decrease of the total wave amplitude after the onset of the wave, which is expressed by the term containing the damping rate γ in Eq. 4.8. If the growth rate δ is smaller than the damping rate γ, the amplitude enhancement after the onset of the wave can be neglected and energy dissipation is dominant during the temporal evolution. In the opposite case the attendance of a wave source leads to an increasing wave amplitude as long as the wave polarization is mainly poloidal. After the time τ wave dissipation predominates wave growth and the wave field attenuates.

4.2   Temporal evolution inside an Alfvén resonator

Near local extrema of the field line eigenfrequency the gradient $d\Omega_T/dL$ is comparatively small. Thus, following Eq. 4.5 in such a region the effect of field line phase mixing is weak as the time τ becomes very large and the wave field possibly remains poloidal polarized in time. The temporal evolution of an Alfvén wave field inside a resonator region bounded by two poloidal turning points (see Sec. 3.4) has been investigated by Mager and Klimushkin (2006) for a monochromatic wave field, i.e. wave growth and damping have been neglected. Therefore, the Fourier transformation of the corresponding function $Q_N(L, \omega)$ (see Eq. 3.23) has to be determined, which defines the radial wave structure:

$$
\begin{aligned}
R_N(L, t) &= \frac{1}{\sqrt{2\pi}} \int_{-\infty}^{\infty} Q_N(L, \omega)e^{-i\omega t}d\omega \\
&= \sum_{n=0}^{\infty} c_n H_n(\xi)e^{-\frac{\xi^2}{2}} \int_{-\infty}^{\infty} \frac{e^{-i\omega t}}{\omega^2 - \omega_n^2}d\omega
\end{aligned}
\tag{4.9}
$$

with $\xi = (L - L_0)/\sigma$ (see Sec. 3.4). The Fourier-integral in the equation above can be solved by applying a Laplace-transformation on the function $f = 1/(\omega^2 - \omega_N^2)$, which results in $\mathcal{L}(f) = \sin(\omega_n t)/\omega_n$ (e.g. Bronstein et al. 1996). Furthermore, the wave source is again assumed to be described by a δ-function in time. In doing so one obtains an expression for the spatio-temporal structure of a wave excited inside an Alfvén resonator (Mager and Klimushkin 2006):

$$
R_N(L, t) = 2 \sum_{j=0}^{\infty} \frac{c_j}{\omega_{2j}} \sin(\omega_{2j}t)R_{N2j}(L, \omega)
\tag{4.10}
$$

with

$$
c_j = \sqrt{2\pi}q_N\pi^{-1/4}2^{-j}\frac{\sqrt{(2j)!}}{j!}.
$$

The eigenfrequencies ω_n of the resonator are defined by Eq. 3.20. The difference between the eigenfrequencies $\Delta\omega_n$, which is triggered by the factor λ_R^2/σ^2, has a major impact on the development of the wave field inside the Alfvén resonator in time. For values of λ_R^2/σ^2 being sufficiently large the first summand of Eq. 4.10 with $\omega_{n=0}$ exhibits the highest amplitude and thus dominates the other terms. In other words large frequency splitting prevents higher radial harmonics influencing the oscillation with the frequency ω_0. This fact inevitably results in the stability of the Gaussian radial amplitude distribution assumed for $n = 0$ (see Sec. 3.4) during the lifetime of the oscillation.

On the other hand smaller differences $\Delta\omega_n$ lead to similar eigenfrequencies of summands in a certain range of n values in Eq. 4.10. Consequently, the amplitudes of the corresponding radial structures $H_n \exp(-\xi^2/2)$ are of the same order of magnitude and their interaction cannot be neglected. The temporal evolution of such a wave field is shown in Fig. 4.1 for $\lambda_R^2/\sigma^2 = 0.001$, which is a realistic value for a second longitudinal harmonic oscillation. After the onset of the poloidal pulsation its radial structure is a Gaussian of the width σ which is still evident at $t = 10\,T$, where T is the wave period. Due to the interaction of radial harmonics the amplitude distribution changes to smaller radial scales in the course of time. When the radial wavelength becomes smaller than the temporally constant azimuthal wavelength, the polarization of the wave field is transformed from poloidal to toroidal. This situation is comparable to the process of field line phase mixing discussed in Sec. 4.1, where the temporal evolution of wave field is influenced by the interaction of separate waves oscillating with slightly different frequencies. Accordingly, the change of wave polarization after the elapse of a typical time τ also occurs for pulsation excited inside an Alfvén resonator, when the longitudinal harmonic number is at least $N = 2$ (Mager and Klimushkin 2006).

The temporal evolution of the wave amplitude can be implemented in Eq. 4.9 by considering wave growth rate δ and damping decrement γ. Consequently, the modified Fourier-integral is solved by the Laplace-transformation

$$\mathcal{L}(f) = \mathcal{L}\left[\frac{1}{(\omega - i\delta + i\gamma)^2 - \omega_N^2}\right] = \frac{1}{\omega_n}\sin(\omega_n t)e^{(\delta-\gamma)t}. \tag{4.11}$$

The resulting spatio-temporal structure can be expressed by

$$R_N(L,t) = 2\sum_{j=0}^{\infty}\frac{c_j}{\omega_{2j}}\sin(\omega_{2j}t)R_{N2j}(L,\omega)e^{(\delta-\gamma)t}. \tag{4.12}$$

This is the expression of Eq. 4.10 multiplied with an exponential function describing the interplay of wave growth and damping. As long as $\delta > \gamma$ the wave amplitude growth, while strong wave damping lead to decreasing wave amplitude (see Sec. 4.1).

4.3   Influence of the ionosphere

The terrestrial ionosphere presents the ionized part of the upper atmosphere and is a conducting interface between the lower neutral atmosphere and the magnetosphere. The response of standing field line oscillations on the ionosphere is influenced by the interaction of the current system carried with a standing Alfvén wave with the ionospheric currents. In
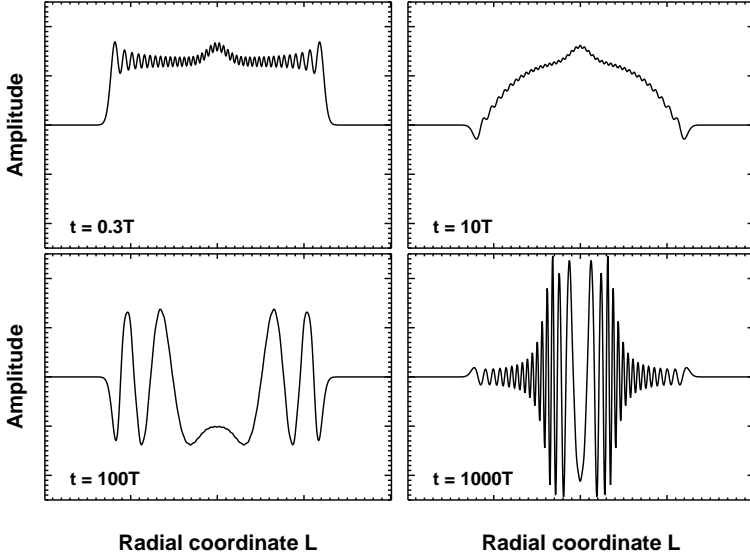
Figure 4.1: Temporal evolution of the wave radial structure. The amplitude remains a Gaussian distribution for several wave periods T. Small scaled stuctures appear later due to phase mixing of different resonator eigenoscillations.

this process immediately above the ionosphere the field aligned currents of the Alfvén wave are closed by ionospheric Pedersen currents, which are transverse to the magnetic field perturbation and parallel to the electric field (e.g. Glassmeier 1995). In this region magnetic and electric field of the wave are related by (Hughes 1974, Hughes and Southwood 1976)

$$b = \pm\mu_0\Sigma_P E, \qquad (4.13)$$

where Σ_P is the height integrated Pedersen conductivity. As the vertical scale size of the conducting layer, which is around 200 km, is much smaller than the wavelength of a field line oscillation of several Earth radii, it is sufficient using the height integrated values of the conductivity. When Σ_P is uniform one can derive the following relation between the electric field of the incident wave E_I and the reflected wave E_R (Scholer 1970):

$$E_R = \frac{1 - \mu_0 V_A \Sigma_P}{1 + \mu_0 V_A \Sigma_P} E_I = R E_I. \qquad (4.14)$$

Typical values of Σ_P are between 0.1 S at the nightside and around 10 S at the dayside. The Alfvén wave velocity is by the order of magnitude $V_A = 10^5$ km/s (e.g. Fedorov et al. 2006) leading to a reflection coefficients between $R \approx -0.85$ and $R \approx -0.99$. Thus, under realistic conditions the assumption of a ideal conducting ionosphere is justified. Furthermore, a reflection coefficient of $R = -1$ implies a zero electric field, which is

related via Eq. 2.8 with a slow plasma motion, so that the magnetic field line is tied in the ionosphere. However, not the complete energy of an incident Alfvén wave is reflected as under realistic conditions an ideal reflection coefficient cannot be realized. By multiplying Eq. 4.13 with the complex electric field E^* one obtains the expression

$$\frac{E^* b}{\mu_0} = \Sigma_P |E|^2. \tag{4.15}$$

This equation describes the mechanism how standing field line oscillations looses energy at their ionospheric footprint. On the left hand side of Eq. 4.15 emerges a downward Poynting flux in an Alfvén wave, which is balanced by the term $\Sigma_P |E|^2$. Thus, an Alfvén wave propagating along a magnetic field line towards the ionosphere is almost ideally reflected, but a small portion of the wave energy dissipates in the ionosphere due to Joule heating caused by the finite ionospheric Pedersen conductivity (e.g. Southwood and Hughes 1983).

The wave damping is considered by introducing a complex frequency with the imaginary part γ, so that the oscillation behaves as $\exp(-i\omega t + \gamma t)$. A quantitative information about the wave damping is provided by the damping decrement γ/ω. Numerical calculations of Newton et al. (1978) have suggested that the damping constant γ is inversely proportional to Σ_P and is given by the approximation

$$\gamma \approx \frac{1}{10 \cdot \Sigma_P \cdot L}. \tag{4.16}$$

Assuming an ULF pulsation located at the L shell $L = 4$ oscillating with $f = 0.01$ Hz results in typical damping decrements in the range $\gamma/\omega = 0.05, \ldots, 0.4$ (e.g. Glassmeier et al. 1984b, Allan et al. 1986, Ozeke and Mann 2004). Accordingly, magnetospheric Alfvén waves can occur in wave packets of up to 20 cycles, which is confirmed by ground based observations.

The general role of the ionosphere as a sink of wave energy is widely accepted. Nevertheless Leonovich and Mazur (1993) have proposed the possibility of extraneous field aligned currents $\boldsymbol{j}_{ext}$ in the ionosphere acting as source of ULF wave activity. In this case Ohm's law should be written as

$$\boldsymbol{j} = \hat{\boldsymbol{\sigma}} \boldsymbol{E} + \boldsymbol{j}_{ext} \tag{4.17}$$

with the conductivity tensor $\hat{\boldsymbol{\sigma}}$. These external currents are suggested to be excited by internal gravity waves or local perturbations of the electric field. Both ionospheric damping and source mechanism entrain the theoretical description of the wave spatial structure in Chapter 2 by modifying the boundary condition Eq. 2.24 to

$$\Phi|_{N,S} = \mp \frac{1}{\epsilon_0 \omega \Sigma_P} \frac{\partial \Phi}{\partial \theta}\bigg|_{N,S} - \Sigma_P \Delta_\perp J_\parallel \big|_{N,S} \tag{4.18}$$

with $\Delta_\perp J_\parallel|_{N,S} = j_{ext,\parallel}|_{N,S}$ (Leonovich and Mazur 1993). The first term on the right hand side of Eq. 4.18 describes the dissipation of the wave in the ionosphere and the second term represents its possible generation by external currents.

4.4 Magnetospheric plasma instabilities

A mechanism describing an effective interaction between standing Alfvén waves and magnetospheric particles is the drift-bounce resonance, which is capable to feed energy to an Alfvén wave field as well as to provide wave damping. Initially this process was suggested by Southwood et al. (1969), who derived the resonance condition

$$\omega_{wave} - m_{wave}\omega_{drift} = N\omega_{bounce} \qquad (4.19)$$

for the integer number N representing the harmonic number of the field line oscillation. The frequency ω_{bounce} is related to the bounce motion of charged particles in dipolar magnetic field lines trapped between the mirror points above the northern and southern ionosphere. This motion is superposed by a azimuthal directed current of the particles due to curvature and gradient drift, which is represented by the frequency ω_{drift}. If the condition Eq. 4.19 is satisfied, a magnetospheric particle is exposed to a constant electric field due to the presence of the wave with the frequency ω_{wave} and thus will be steadily accelerated or decelerated. In a collisionless plasma this resonance process may take a long time, until the particle moves out of synchronism with the wave. In the electric field of the fundamental standing field line oscillation the net acceleration over a bounce period is zero independent of the relative phasing between the wave and the particle. Contrary, for any even mode structure, such as the second harmonic waves which are often observed for poloidal Alfvén waves, particles in resonance may exchange energy with the wave over many bouncing periods (Southwood and Kivelson 1982).

As a wave resonates with a distribution of particles, the wave looses energy when more particles are accelerated than decelerated. This mechanism is also known as Landau damping in a collisionless plasma. In the opposite case the wave gains energy at the expense of the particle energy leading to unstable plasma, which is a possible source of ULF pulsations. The condition for such an instability leading to wave growth is

$$\frac{df_{res}}{dW} > 0, \qquad (4.20)$$

where f_{res} is the part the particle distribution approximately fulfilling Eq. 4.19 and W the particle energy (Southwood et al. 1969, Southwood and Hughes 1983). Eq. 4.20 describes a bump on the particle distribution that is believed to origin from a substorm injection of energetic particles. Due to differences in energy these protons drift with different velocities from the nightside in westward direction, so that the velocity distribution can be far from the Maxwellian (Southwood 1977).

Another excitation mechanisms for magnetospheric ULF waves are plasma instabilities driven by the free energy associated with pressure anisotropies that can be transported into wave energy. In case the plasma pressure transverse to the ambient magnetic field $P_\perp$ exceeds the parallel pressure $P_\parallel$, a mirror magnetic field geometry can occur, which in turn increases the pressure anisotropy (Hasegawa 1969). This mirror instability growth, if the condition

$$\frac{\beta_\perp}{\beta_\parallel} > 1 + \frac{1}{\beta_\parallel} \qquad (4.21)$$

is fulfilled. This mirror mode is a purely growing compressional structure. Due to gradients in plasma density, magnetic field or plasma pressure, e.g. in the ring current region, this

mirror mode couples to drift waves and the resulting instability is called drift mirror instability. The resulting growing mode is polarized like the slow magnetosonic mode and propagates azimuthally at the drift velocity (Hasegawa 1969, Pokhotelov et al. 1985). However, the classical drift mirror mechanism fails to explain poloidal waves, as these oscillations have transverse magnetic field components larger than the compressional one, which is not the case for the magnetosonic mode (e.g. Glassmeier 1995). Thus, the excitation of poloidal waves requires coupling of the compressional slow mode to shear Alfvén perturbations, which occurs in particular due to the presence of field line curvature, because of the small compressional component of the poloidal Alfvén wave (e.g. Pokhotelov et al. 1986, Woch et al. 1988, Chen and Hasegawa 1991a, Glassmeier et al. 1999, Klimushkin and Mager 2008).

5 The Cluster mission

5.1 Spacecraft configuration

A substantial progress in the in situ observations of magnetospheric plasma processes and its interaction with the solar wind has been achieved by the realization of the Cluster mission consisting of four identical build spacecraft (Escoubet et al. 1997, 2001). On July 16 and August 9, 2000, respectively, the satellites were delivered in pairs from the Russian cosmodrome in Baikonour into their designated orbit. After the commissioning of the instruments on board the mission was declared operational on February 1, 2001. Since that time 11 different experiments on each spacecraft provide measurements of magnetic and electric field as well as plasma particles and its distribution functions, most of them working in high time resolution. A mechanical drawing of a Cluster satellite is shown in Fig. 5.1.

The investigation of the interaction between solar activity and the terrestrial magnetosphere has been declared as the main goal of the Cluster mission, that is intended to be achieved by the investigation of small-scaled plasma structures in space and time in
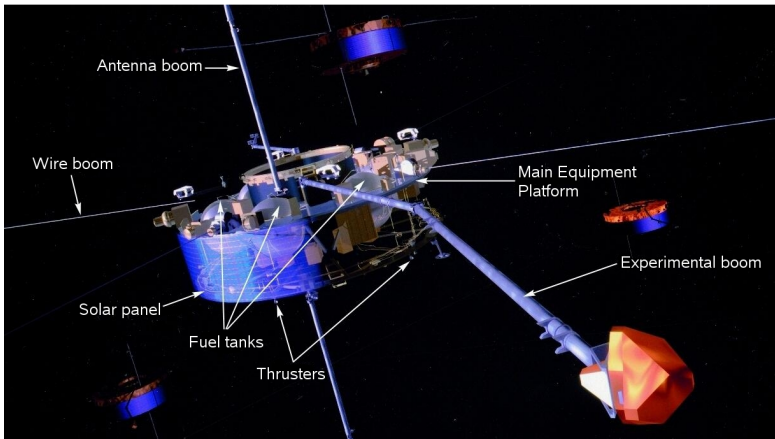

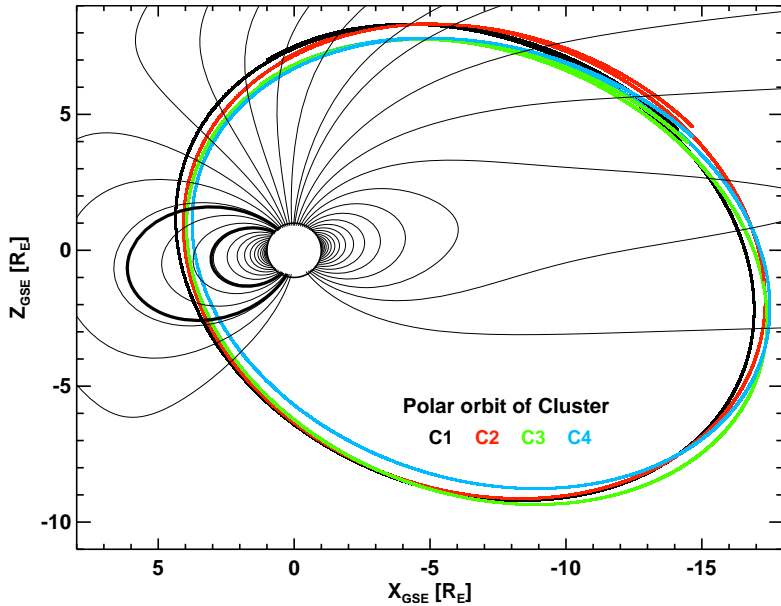Figure 5.1: Image of Cluster satellite and instrumentation (Escoubet et al. 1997).

Figure 5.2: Cluster orbit in GSE coordinates and magnetic field lines determined from Tsy96 modell. The thick field lines represent possible locations of the plasmapause.

the following key plasma regions: Solar wind and bow shock, magnetopause, polar cusp, magnetotail and auroral zone (Escoubet et al. 2001). In order to study these specific regions the Cluster spacecraft are placed in a polar orbit with the perigee about 4 and the apogee about 20 Earth radii and a 57 hours period. The plane of the orbit is fixed with respect to inertial space allowing for a complete 360° scan of the magnetosphere every year. A typical Cluster orbit with dayside perigee is displayed in Fig. 5.2 in GSE (Geocentric Solar Ecliptic) coordinates, where X_{GSE} is directed from the Earth towards the sun, Y_{GSE} is chosen to be in the ecliptic plane opposing the planetary motion and Z_{GSE} is parallel to the ecliptic pole (Russell 1971). The orbit is compared with possible locations of the terrestrial plasmapause that is between 3 and 6 R_E depending on the solar activity level. Obviously, during the perigee passage the Cluster satellites approach the plasmapause or even transit this boundary. As elucidated in Sec. 3.4 this specific region exhibits suitable conditions for the excitations of radially trapped ULF waves inside the Alfvén resonator. Thus, the design of the Cluster orbit implicates suitable conditions for the detection of this particular type of standing field line oscillations.

The main advance of the Cluster mission compared to earlier one or two spacecraft missions, which are restricted to one-dimensional or under certain circumstances two-dimensional data processing, is the possibility of building a tetrahedron constellation by

the four satellites. Such a configuration best suites to study three-dimensional plasma structures and to derive vector quantities (e.g. Dunlop et al. 1990). In order to ensure the coverage of different scale sizes on which the plasma processes of interest take place the spacecraft separation varies from 100 km to 20,000 km during the mission. Due to orbital dynamics a fixed constellation cannot be maintained throughout a complete orbit, so that the spacecraft configuration changes continuously during the mission. For analyzing ULF pulsations in the inner magnetosphere that means one is obliged to deal with various spacecraft configurations, such as the extreme cases the perfect tetrahedron and satellites following each other on the same trajectory, like a string of pearls. The latter configuration is not necessarily a handicap for investigating field line oscillations, as it gives a good insight in the temporal evolution of a detected pulsation. On the other hand the analysis of the spatial structure is improved by slightly different orbits, in particular for the radial coordinate when the satellites cover a certain range of magnetic L-shells at the same time. Furthermore, the spacecraft separation in the azimuthal direction allows for determination of the wave azimuthal wavelength.

5.2   Measurement of FGM sensors

The observation of the magnetic field is of particular interest for this work. It is measured by two triaxial fluxgate magnetometer (FGM) onboard each satellite (Balogh et al. 2001), one inboard sensor another one fixed at the end of the 5 m long experimental boom. A fluxgate magnetometer is composed of a ring core of a highly magnetically permeable alloy and two coil windings (Fig. 5.3). The drive winding is wrapped around the core and generates an alternating magnetic field of constant frequency that moves the core periodically into saturation. Due to the presence of a external magnetic field a voltage is induced in a sensor coil oscillating in multiples of the driver frequency. The amplitude of this voltage, usually its second harmonic is considered only, is proportional to the amplitude of the external magnetic field to be measured. Combining three interleaved crossed fluxgate magnetometers allows the detection of the magnetic field vector. The normal operational mode of the FGM sensors provides a sampling rate of 15.519 Hz, while during the burst mode the sampling rate is increased up to 67.249 Hz. Furthermore the magnetometers operate in four measuring ranges with resolutions of 10^{-2} nT in the lowest and up to 0.5 nT in the highest range. The maximum detectable magnetic field strength is $B = 4096$ nT. Sampling rate and resolution of the fluxgate magnetometers assure high quality magnetic field measurements. FGM data transformed routinely from spacecraft to GSE coordinates and interpolated to a resolution of 4 s are used, as a Nyquist frequency of $f = 125$ mHz is sufficient for the basic analysis of standing field line oscillations with frequencies below 100 mHz. For deeper investigations of the signals, such as for the determination of the wave azimuthal wavelength m (Secs. 7.3 and 8.4), higher resolved data are produced.

5.3   Measurement of EFW sensors

The Electric Field and Wave (EFW) instrument onboard each Cluster satellite consists of two double-probes installed at the end of long wire booms in the spin plane with a
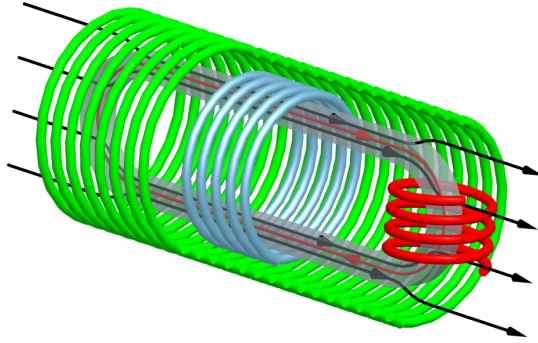
Figure 5.3: Construction of a fluxgate magnetometer. The drive winding (red coil) generates an oscillating magnetic field (red line) in the ring core (grey ring core). The black lines represent the external magnetic field. The blue and green windings are the sensor coils (with kind permission of Bernd Chares, MPS).

probe-to-probe separation of 88 m (Gustafsson et al. 1997, 2001). Two opposite spherical sensors are fed with constant and identical bias currents I_b (Fig. 5.4). If the resistances R_p over the sheath surrounding the probes are equal, the voltage U measured on board the spacecraft will be equal to the potential difference Φ in the plasma between the probe locations (Pedersen et al. 1998). The potential differences measured with the orthogonal double-probes provide the electric field in two directions in the spacecraft system, $E_{x,spin}$ and $E_{y,spin}$, that is a close approximation to GSE coordinates but with the z-axis along the spacecraft spin axis. For Cluster both z-axes differ only by a few degree, so that $E_{x,GSE} \approx E_{x,spin}$ and $E_{y,GSE} \approx E_{y,spin}$ (Eriksson et al. 2006). In this thesis the electric field vector E is used together with the magnetic field B for the determination of the Poynting vector (see Sec. 6.4). Thus, measurements of magnetic and electric field of Cluster provide an insight into the direction of energy transport of the Alfvén waves under investigation.

In addition to the current mode for measuring the electric field, the spherical sensors can be operated as current-collecting Langmuir probes (e.g. Gustafsson et al. 2001). For this mode the probe is given a bias voltage that is referred to as the satellite ground, though the variations in the spacecraft potential can be detected by another probe pair operating in electric field mode, which then have a potential close to that of the ambient plasma and serve as a reference for the spacecraft potential. The difference between spacecraft and probe potentials received in this way is proportional to the ambient electron density assuming that the electron temperature is constant (Eriksson et al. 2006). Consequently, the potential difference is capable e.g. for the identification of the plasmapause location, which is characterized by a steep change in the plasma density, in order to proof the reliability of the used model of the magnetospheric electron density distribution described in Sec. 6.2.3.
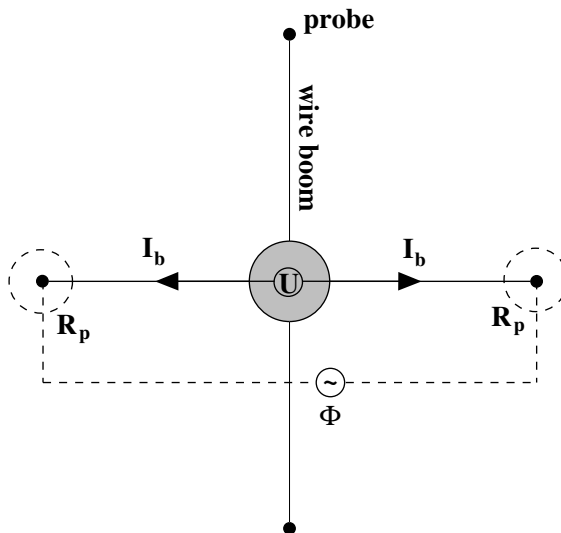
Figure 5.4: Sketch of a Cluster satellite with wire boom and spherical probes of EFW instrument (after Eriksson et al. (2006)). The illustration is not to scale.

6 Analysis of magnetospheric ULF pulsations

6.1 Determination of field line eigenfrequencies

The difference between toroidal and poloidal eigenfrequencies and their distribution within the magnetosphere mainly define the spatio-temporal structure of field line oscillations under investigation in the present work. Both the toroidal and poloidal eigenfrequency problems available by the differential equations Eqs. 2.25 and 2.26 are of the form

$$f_1(x)\frac{d^2y}{dx^2} + f_2(x)\frac{dy}{dx} + f_3(x)y = -\omega^2 y \qquad (6.1)$$

with the boundary condition $y(x_a) = y(x_b) = 0$ and the eigenvalue ω. An appropriate procedure to solve such differential equations is the finite difference method that allows to transform Eq. 6.1 to the eigenvalue problem

$$A\mathbf{y} = \lambda\mathbf{y}. \qquad (6.2)$$

In order to determine the derivations of y using finite differences the interval confined by x_a and x_b is separated into n subintervals each of the length h, so that $x_a = x_0 < x_1 < x_2 < \ldots < x_n = x_b$. Thus, in Eq. 6.2 the eigenvalue is given by $\lambda = -h^2\omega^2$ and the eigenvector $\mathbf{y}$ is of the dimension $(n-1)$. The corresponding $(n-1) \times (n-1)$ matrix A is tridiagonal:

$$A = \begin{pmatrix} b_1 & c_1 & 0 & \cdots & 0 & 0 & 0 \\ a_2 & b_2 & c_2 & \cdots & 0 & 0 & 0 \\ \vdots & \vdots & \ddots & \vdots & \vdots & \vdots & \vdots \\ \vdots & \vdots & \vdots & \ddots & \vdots & \vdots & \vdots \\ \vdots & \vdots & \vdots & \vdots & \ddots & \vdots & \vdots \\ 0 & 0 & 0 & \cdots & a_{n-2} & b_{n-2} & c_{n-2} \\ 0 & 0 & 0 & \cdots & 0 & a_{n-1} & b_{n-1} \end{pmatrix}. \qquad (6.3)$$

The three diagonals of the matrix A are given by

$$a_i = f_1(x_i) \qquad (6.4)$$
$$b_i = h^2 f_3(x_i) - h f_2(x_i) - 2 f_1(x_i) \qquad (6.5)$$
$$c_i = h f_2(x_i) + f_1(x_i) \qquad (6.6)$$

57

with $i = 1, \ldots, n - 1$. Comparing Eq. 6.1 with Eqs. 2.25 and 2.26 exhibits that the variable x corresponds to the field aligned coordinate θ, so that the eigenvector y describes the function Φ along a magnetic field line. Also the functions f_1, f_2 and f_3 depend on θ. For both toroidal and poloidal equation $f_1(\theta) = V_A^2 h_\theta^{-2}$ holds, while

$$f_2(\theta) = \frac{V_A^2}{p h_\theta^2} \frac{\partial}{\partial \theta} \left(\frac{p}{h_\theta} \right) \tag{6.7}$$

$$f_3(\theta) = 0 \tag{6.8}$$

is valid for the toroidal equation and

$$f_2(\theta) = \frac{p V_A^2}{h_\theta^2} \frac{\partial}{\partial \theta} \left(\frac{1}{p h_\theta} \right) \tag{6.9}$$

$$f_3(\theta) = \eta V_A^2 \tag{6.10}$$

for the poloidal equation. Finding the field line eigenfrequencies for a given L shell requires the solution of the eigenvalue problem Eq. 6.2 which is done by applying a standard precast code implemented in the used IDL (Interactive Data Language) programming packet used.

For a specific field line the functions $f_{2,3}(\theta)$ are determined by the field aligned distributions of Alfvén velocity, plasma β and current density, where the latter two terms influence the function η defined by Eq. 2.15. The Alfvén velocity requires the knowledge of magnetic field strength and plasma mass density. Furthermore, the geometry of the field line has to be considered, which is incorporated by the parameters p and h_θ (see Sec. 2.1). In the next section 6.2 the models are introduced that are used for the calculation of the previous mentioned terms. The radial profiles of poloidal and toroidal eigenfrequencies are determined by solving the eigenvalue problem of Eq. 6.2 for a range of L shells including the region of interest, i.e. the terrestrial plasmapause.

6.2 Modeling magnetospheric properties

Magnetospheric ULF pulsations are phenomena affecting a localized region of terrestrial field lines and the area of interest is extended several Earth radii. Certainly, observations with satellites or at the ground are not suitable to cover plasma parameters along a complete bunch of field lines. But the knowledge about the plasma properties along oscillating field lines is mandatory to determine resonance frequency, spatial and temporal structure of observed ULF pulsations. Thus, models of plasma parameters, such as magnetic field and plasma density, are used to infer the distribution of the Alfvén velocity in the magnetosphere which defines the toroidal field line eigenfrequency. Additionally models of plasma pressure and ring current density are necessary for the determination of the poloidal eigenfrequency that depends on the parameter η as defined in Eq. 2.15.

6.2.1 Magnetospheric field lines

The terrestrial magnetic field is composed of internal parts generated by the dynamo of the Earth, and external influences such as ionospheric and magnetospheric currents and the solar activity. Within distances of several Earth radii the inner magnetosphere is well

represented by the IGRF (International Geomagnetic Reference Field) magnetic field model and its field lines are dipole-like as a first approximation (e.g. Langel 1987). At larger distances from the Earth the activity level of the solar wind influences the shape and strength of magnetospheric field lines. During periods of high solar activity the magnetopause is moved towards the Earth at the dayside due to the increased solar wind dynamic pressure p_{dyn}, while at the nightside the field lines are stretched to a magnetospheric tail region. However, the solar activity also impacts the near Earth magnetospheric region, as the larger p_{dyn} the smaller is the radial distance of the terrestrial ring current and the larger is its current density, i.e. the back influence on the magnetic field strength becomes larger.

An appropriate model considering the influence of solar wind activity on the IGRF magnetic field was developed by Tsyganenko (1987) and Tsyganenko (1989). It is a semi-empirical best fit representation for the magnetic field by comparing sub-models of ring and current systems as well as Chapman-Ferraro and field-aligned currents with a large number of satellite observations. In a later version of this model the effect of the ring current variation was improved in particular (Tsyganenko 1995, Tsyganenko and Stern 1996), in the following referred as Tsy96. Knowing the correct change of magnetic field strength due to the existence of the ring current is evident for the case studies presented in Chapters 7 and 8 as the Cluster satellites pass magnetic field lines influenced by the ring current.

Information about the solar wind activity are inserted in the Tsy96 model by the solar wind dynamic pressure p_{dyn} and the magnetic field components b_y^{sw} and b_z^{sw} which describe the orientation of the of the solar magnetic field with respect to the terrestrial field lines. Furthermore, the storm time index D_{st} is considered indicating the level of substorm disturbances (Sugiura 1964). Fig. 6.1 displays a comparison of the magnetic field measurements by spacecraft C1 with the results of the Tsy96 model for both days of the case studies under investigation in this work, August 7, 2003 and September 15, 2002, respectively. For the first event the model input parameters are $p_{dyn} = 2.6$ nPa, $D_{st} = -7$ nT, $b_y^{sw} = 6.0$ nT and $b_z^{sw} = 5.0$ nT. For the second event we found $p_{dyn} = 0.85$ nPa, $D_{st} = -19$ nT, $b_y^{sw} = 0.9$ nT and $b_z^{sw} = -0.3$ nT. In both cases observation and modeled magnetic field coincide fairly good in all three components. A derivation of around 3% appears in the magnitude of the magnetic field. Accordingly, the accuracy of the model is sufficient for the estimation of realistic values of magnetic field strength along a field line and its length between the ionospheric boundary.

6.2.2 Current density and plasma pressure

As evident from observations quiet time the dayside ring current is axisymmetric in the inner magnetosphere (Lui and Hamilton 1992). Its intensity $J_\perp$ can be derived from the current model implemented in the Tsy96 model by assuming axially symmetric azimuthal currents confined to the equatorial plane (Tsyganenko and Peredo 1994). Based on these limitations the current density is given by the expression (Connerney et al. 1981)

$$J_{tsy,\perp}(L) = \frac{2}{\mu_0} \frac{\partial A}{\partial z}\bigg|_{z=0}. \qquad (6.11)$$

The vector potential A has a a nonzero azimuthal component $A = A_\phi$ and satisfies $\nabla \times \nabla \times A = 0$. Eq. 6.11 is written in cylindrical coordinates, where L is the radial distance
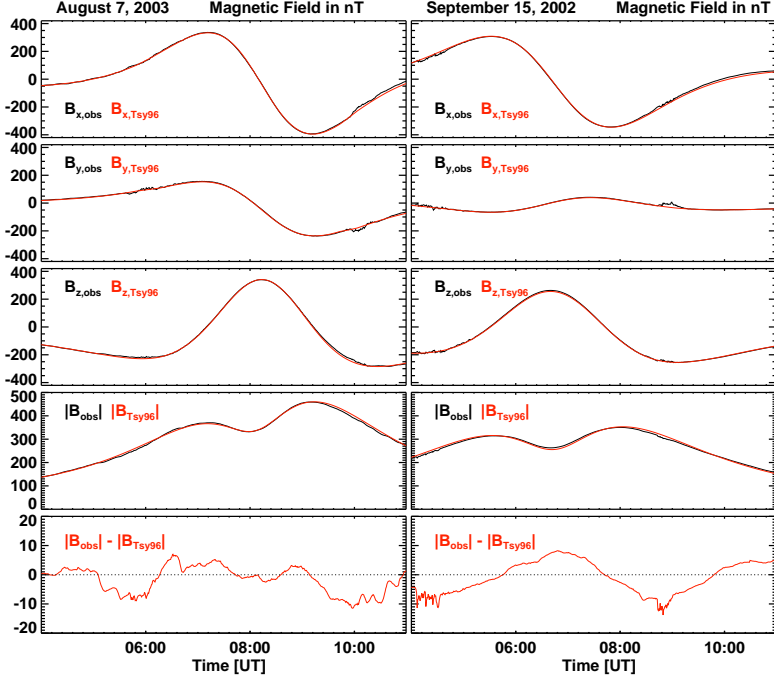
Figure 6.1: Comparison of Cluster measurement (black lines) and Tsy96 model (red lines) for August 7, 2003 (left) and September 15, 2002 (right) in GSM coordinates.

and $z = 0$ corresponds to the equatorial plane. The vector potential $\boldsymbol{A}$ is modeled using formula 11 in Tsyganenko and Peredo (1994) and a set of parameters for the ring current given in tabular 1 therein.

The radial distribution of the total magnetospheric plasma pressure in the noon sector can be approximated by the expression (Klimushkin et al. 2004)

$$P(L) = P_0 \left[1 - \tanh^2 \left(\frac{L_0 - L}{W} \right) \right]. \tag{6.12}$$

The pressure distribution reaches its maximum P_0 at the L-shell L_0 and exhibits a width controlled by the parameter W. As evident from AMPTE satellite observations the pressure maximum is located at $L_0 \approx 3\ R_E$ independent from the magnetospheric activity level (Lui and Hamilton 1992). Contrary, at higher level of disturbance the localization of $P(L)$ is narrower with larger values of P_0 than in quiet times (e.g. Lui et al. 1987, De Michelis et al. 1997). Furthermore, the proton pressure components generally dominates over pressure of heavier ions and electrons (Lui and Hamilton 1992) and there is no jump of pressure on the plasmapause (e.g. Sugiura 1972).

Current density and plasma pressure are connected by the relation valid in the equatorial plane (Lui et al. 1987)

$$J_\perp(L) \approx -\frac{1}{B}\frac{\partial P}{\partial L}.$$

(6.13)

Inserting Eq. 6.12 leads to

$$J_\perp(L) = \frac{\beta_0 B_0^2}{\mu_0 WB}\frac{\tanh\left(\frac{L_0-L}{W}\right)}{\cosh^2\left(\frac{L_0-L}{W}\right)},$$

(6.14)

where β_0 and B_0 are plasma β and magnitude of magnetic field at the L shell L_0. The current density can be obtained from the Tsy96 model by minimizing the function $|J_{tsy,\perp} - J_\perp|$ using the Powell method (e.g. Press et al. 2007), where the free parameters β_0, L_0 and W are varied.

6.2.3 Plasma density distribution

Next to the magnitude of the magnetic field B the plasma mass density along magnetic field lines and in the radial coordinate are required in order to infer a global axisymmetric distribution of the Alfvén velocity V_A. In principle the CIS (Cluster Ion Spectrometry) analyzer (Gustafsson et al. 2001) onboard each Cluster satellite provides information of the ion number density of cold ions (CIS-CODIF). The instruments are capable to distinguish between different sorts of ions, such as H^+, He^+, He^{++} and O^+, which can be used to determine the total plasma mass density via $\rho_{total} = m_p n_p + m_{He^+} n_{He^+} + m_{He2+} n_{He2+} + m_{O^+} n_{O^+}$, where m represents the atomic mass and n the measured number density of the corresponding ions. At first view CIS data are appropriate to determine the mass density at positions of the spacecraft. As an example Fig. 6.2 shows the measurements of number densities of protons and heavier ions made by spacecraft C4 on August 7, 2003. Between 07:20 and 08:50 UT the ion analyzer registers density of the oxygen ion up to 15 times higher than the proton density and the helium ion density similar to n_p. These values are not expected in plasmaspheric regions, where the concentration of O^+-ions can reach at the most 50% during storm time events (e.g. Goldstein 2006). A realistic ion composition in the plasmasphere during a low level of magnetospheric activity is 55% H^+, 40% He^+ and 5% O^+ (Berube et al. 2005) leading to a mass correction of $m_{corr} \approx 3$. In the vicinity of the plasmapause and further out the concentration of heavier ions decreases and one can assume $m_{corr} \approx 2$.

The reason for the obviously deficient measurement of the CIS-CODIF instrument is that the ion sensor is not designed to accomplish the ion densities and energies prevalent in this region of the magnetosphere as the Cluster mission was primarily not intended for the investigation of the plasmasphere. As a consequence disturbances of the CIS sensors are caused: The energy of a single proton can be large enough to excite the detection of heavier ions. For this reason measured densities of He^+, He^{++} and O^+ ions and the resulting total plasma mass density are larger than in reality.

In order to elude the problems with incorrect measured ion densities an empirical model of the electron number density n_e of the terrestrial magnetosphere is used in this work that has been developed by Carpenter and Anderson (1992) and is based on radio measurements of the ISEE 1 satellite and whistler wave observations. It considers diurnal, annual and
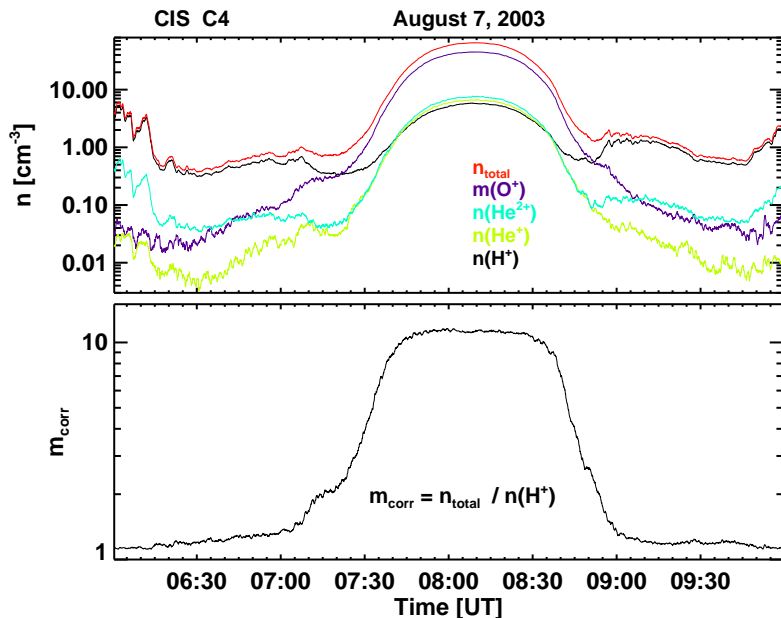
Figure 6.2: Number densities of protons and heavy ions (He^+, He^{++} and O^+) observed by the CIS instrument onboard Cluster C4 for August 7, 2003 (top panel). The ratio of total number density n_{total} compared with the proton number density $n(H^+)$ is shown in the lower panel.

solar cycle effects and, thus, realistic results are expected for given background conditions. The electron density is modeled on a piecewise basis for plasmasphere, plasmapause and magnetosphere, respectively, for the magnetic equatorial plane.

At first the location and profile of the plasmapause must be known to establish a radial profile of the electron density. In Carpenter and Anderson (1992) a simple expression was derived that gives the plasmapause position in terms of the level of solar activity via $L_{pp} = 5.6 - 0.46K_{p,max}$. Here L_{pp} is the inner boundary of the plasmapause and $K_{P,max}$ the maximum K_p index of the preceding 24 hours. This relation reflects that during high solar activity the plasmapause is pressed to smaller L-shells. However, the generation process of the boundary implies a dependency of L_{pp} on the magnetic local time (Sec. 1.1), so that an accurate identification of the plasmapause location at the magnetic local time of the Cluster satellite orbit requires a more complex model. Therefore, the plasmapause is determined using the dynamical simulations of plasmapause formation developed by Pierrard and Lemaire (2004) and Pierrard and Cabrera (2005). This simulation uses the magnetospheric electric field model E5D determined from dynamical proton and electron spectra measured on board the geostationary satellites ATS5 and 6 (McIlwain 1986). As

the electric field model depends only on the K_p index the simulation of the plasmapause formation is fully determined by this activity index.

Inside the plasmasphere corresponding to region up to the position of the inner boundary of the plasmapause,i.e. $L \leq L_{pp}$, the radial profile of the electron density is given by the expression Carpenter and Anderson (1992)

$$\log_{10} n_e = (-0.3145L + 3.9043) + A \exp\left(-\frac{L-2}{1.5}\right) \tag{6.15}$$

with

$$A = \left\{0.15\left[\cos\left(\frac{2\pi(d+9)}{365}\right) - 0.5\cos\left(\frac{4\pi(d+9)}{365}\right)\right] + 0.00127N_R - 0.0635\right\}. \tag{6.16}$$

The parameter d is the day of year number. The first summand of the function A in Eq. 6.15 refers to the observed annual variation of n_e inside the plasmasphere (e.g. Park et al. 1978, Clilverd et al. 1991). The global electron density is highest in December and lowest in June, because the tilt of the magnetic dipole axis from the rotation axis causes that the field line footprints at the southern ionosphere are longer exposed to sunlight in December leading to a higher rate of ionospheric ions filling the plasmasphere (e.g. Guiter et al. 1995, Clilverd et al. 2007). The parameter N_R is the 13-month average sunspot number reflecting the influence of the solar activity, as during periods of high sunspot numbers the electron density is larger than to that at solar minimum (e.g. Carpenter 1962, Park et al. 1978).

For magnetic L shells $L > L_{pp}$ the electron density inside the plasmapause is given by

$$log_{10}n_e = log_{10}n_e(L_{pp}) - \frac{L - L_{pp}}{0.1 + 0.011(MLT - 6)}, \tag{6.17}$$

where MLT is the magnetic local time defining the azimuthal coordinate (see Sec. 6.3.2). Eq. 6.17 is valid for the dayside sector between 06 and 15 MLT (Carpenter and Anderson 1992), which is sufficient for the present work as in both case studies the Cluster satellites are located near magnetic noon. In the same azimuthal range the electron density in the plasma trough outside the plasmapause can be expressed by

$$n_e = (-800 + 1400d)L^{-4.5} + \left[1 - \exp\left(-\frac{L-2}{10}\right)\right]. \tag{6.18}$$

The distributions of n_e for plasmapause and plasma trough are both calculated for L-shells $L > L_{pp}$, so that the outer boundary of the plasmapause is determined by the intersection of the resulting density profiles. An example of a complete radial distribution of $n_e(L)$ is displayed in Fig. 6.3 composed of the model expressions Eqs. 6.15, 6.17 and 6.18. Thus, the model applied gives realistic values of the electron number density in the magnetic equatorial plane and allows the determination of the plasmapause location as well as its thickness Δ_{pp}.

The plasma mass density $\rho(L)$ can be estimated from the modeled electron number density $n_e(L)$. This requires a mass correction factor m_{coor} to calculate the plasma mass density $\rho_{eq}(L) = n_e(L)m_{corr}m_p$, where m_p is the proton mass and m_{corr} is related to the influence of heavier ions by taking into account the ion compositions of plasmasphere and plasmapause mentioned above. Consequently, realistic values are between $m_{corr} = 2 - 3$
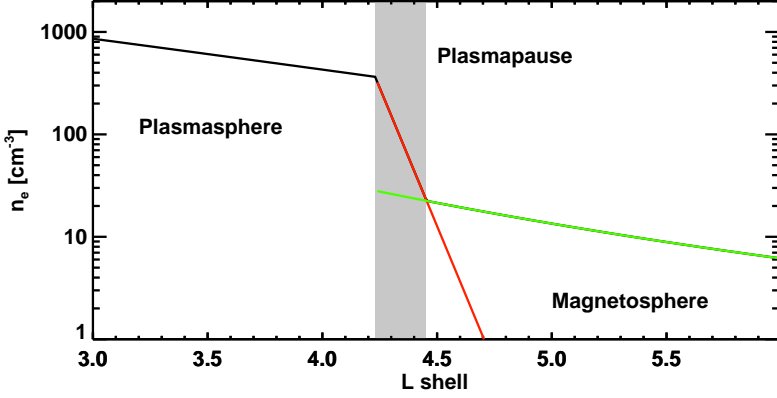
Figure 6.3: Example of electron number density distribution inside magnetosphere.

for the plasmasphere and $m_{corr} = 1 - 2$ for the plasmapause. Knowing the distribution ρ_{eq} in the magnetic equatorial plane the plasma density along a magnetic field line ρ_{fl} can be adopted from the power law (e.g. Cummings et al. 1969, Takahashi and Anderson 1992, Schulz 1996)

$$\rho_{fl} = \rho_{eq} \left(\frac{L}{r} \right)^{\alpha} , \qquad (6.19)$$

where L is the McIlwain parameter of the field line and r the radial distance from the center of the Earth to a position at the field line. The power law index α determines the field aligned density distribution. For $\alpha = 0$ the density and for $\alpha = 6$ the Alfvén velocity V_A is constant along the field line. In the latter case the frequencies of higher harmonic field line oscillations are integer multiple of the fundamental mode, i.e. $f_N = N f_1$ (e.g. Takahashi et al. 2004). Inside the high density plasmasphere, where the hydrostatic approximation is valid, the field line dependence of the density is consistent with diffuse equilibrium and $\alpha = 0 - 1$ has been theoretically predicted by Angerami and Carpenter (1966) and experimentally confirmed by e.g. Goldstein et al. (2001) and Denton et al. (2004). Outside the plasmasphere, where the density is small, power law indices of $\alpha = 1.7 - 3.0$ have been found representing an intermediate consistent between that consistent with diffusive equilibrium and collisionless models (e.g. Goldstein et al. 2001).

In summary, although the real plasma mass density is unknown estimations of the Alfvén velocity distributions in the equatorial plane as well as along magnetic field lines are possible that are necessary for the determination of field line eigenfrequencies (see Sec. 6.1). One can act on the assumption that the uncertainties of the eigenfrequencies are more influenced by the error of m_{corr} than by the error of α: As seen by the integral in Eq. 2.28 the greatest contributions to the eigenfrequencies are made by the Alfvén velocities near the magnetic equator, where B and hence V_A are smallest. Consequently, the value of the eigenfrequency is more influenced by the equatorial Alfvén wave than by its field aligned distribution.

6.3   Coordinate systems

6.3.1   Mean-field aligned coordinate system

Observations used are 4s averaged magnetic and electric field measurements. The data are transformed into a Mean-Field-Aligned (MFA) coordinate system $(e_r, e_\phi, e_\parallel)$, where $e_\parallel$ denotes the unit vector in the direction of the background magnetic field, e_ϕ the unit vector perpendicular to the plane spanned by $e_\parallel$ and the spacecraft position vector r_{sc}. The unit vector e_r completes the right hand $(e_r, e_\phi, e_\parallel)$ triad. The coordinate system used is thus defined as follows:

$$e_r \;=\; e_\phi \times e_\parallel \tag{6.20}$$

$$e_\phi \;=\; \frac{\langle B \rangle \times r_{sc}}{|\langle B \rangle \times r_{sc}|} \tag{6.21}$$

$$e_\parallel \;=\; \frac{\langle B \rangle}{|B|}. \tag{6.22}$$

The mean magnetic field $\langle B \rangle$ is defined as a 512 second running average magnetic field vector. In the MFA-system $(b_r, b_\phi, b_\parallel)$ denote the magnetic disturbance field vectors. As we are only interested in field perturbations the mean value of the field-aligned component has been subtracted. The MFA-system allows to inspect also the polarization of the analyzed oscillations with $(b_r, b_\phi, b_\parallel)$ approximately describing poloidal, toroidal, and field-aligned components, respectively.

To describe the electric field perturbations we furthermore assume that $E \cdot B = 0$, i.e. no field-aligned electric field exists. This allows to determine the third electric field component from the two spacecraft spin-plane electric field components provided by the EFW instrument onboard CLUSTER. The vector $(E_r, E_\phi, 0)$ denotes the electric field in the MFA-system.

6.3.2   LDM Coordinate System

The main aim of the case studies presented in Sec.7 and Sec.8 is to investigate spatial and temporal structures of poloidal Alfvén waves. In principle, this requires a 4D-representation of the measurements made. To approach this requirement a special coordinate system, the LDM coordinate system, is introduced which is schematically shown in Fig. 6.4. The radial coordinate is resembled by the McIlwain Parameter (McIlwain 1966) L that describes the distance of the vertex of a specific field line with respect to the center of the Earth in units of R_E. This coordinate agrees with the radial coordinate defined in Sec. 2.1. To identify the field line for a given point in space the Tsyganenko 96 model (Tsyganenko 1995, Tsyganenko and Stern 1996) is used. The second coordinate D describes the position of the spacecraft on the specified field line and is defined as the distance between the spacecraft and the field line vertex along the field line. Positive D values correspond to a spacecraft location in the northern magnetic hemisphere. This coordinate is related to the magnetic latitude θ introduced for the theoretical description of field line oscillations. As the units of both coordinates L and D are Earth radii R_E it appears to be more appropriate to use the D values for a more descriptive comparison of field aligned and radial spatial scales of the analyzed ULF pulsations.
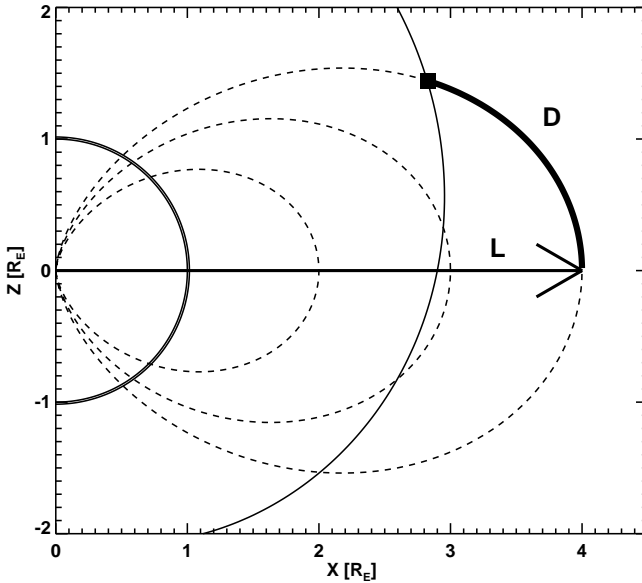
Figure 6.4: Schematic illustrating the L-D-M coordinate system. The spacecraft positions are marked by rectangles, the dotted lines represent magnetic field lines.

The third coordinate, M, describes the magnetic local time (MLT) at which the measurements are taken, which is related to the azimuthal coordinate ϕ used in Sec. 2.1. The value of M emanates from the geomagnetic coordinate system MAG, which is often used for defining the positions of magnetic ground based and spacecraft observations concerning magnetospheric field lines. Its z-axis is parallel to the magnetospheric dipole axis and its y-axis is perpendicular to the geographic poles such that Y_{MAG} is the intersection between the geographic equator and the geographic meridian 90° East of the meridian containing the dipole axis (e.g. Hapgood 1992). The x-axis completes the right-handed orthogonal system. In MAG coordinates the plane $Y_{MAG} = 0$ defines the magnetic equatorial plane and the magnetic local time is defined as the magnetic longitude of the observer minus the magnetic longitude of the sun expressed in ours plus 12h. In the MAG system the magnetic longitude is $\lambda = \tan(Y_{MAG}/X_{MAG})$ (e.g. Russell 1971). Consequently, the dayside sector is from 06h to 18h MLT and magnetic noon is at $M = 12$h MLT.

6.4   Poynting vector

The magnetospheric Alfvén waves theoretically described in Sec. 2 are accounted as standing waves along the magnetic field lines. Accordingly, it is of particular importance to proof the standing wave character of an observed ULF pulsation by investigating its

energy transport. In general direction and intensity of the energy flux density of a plasma wave, which corresponds to the direction of wave propagation, is given by the Poynting vector defined by

$$\boldsymbol{S}_p = \frac{1}{\mu_0} \boldsymbol{E} \times \boldsymbol{b},$$ (6.23)

where $\boldsymbol{E}$ is the electric field and $\boldsymbol{b}$ the perturbation of the magnetic field caused of the plasma wave. Assuming a standing magnetospheric field line oscillation with either a toroidal or a poloidal polarization, the wave fluctuates in the E_r and b_ϕ components or in the E_ϕ and b_r components, respectively (see Sec.1.2). In both cases, taking into account Eq. 6.23 the transverse components of the Poynting vector $\boldsymbol{S}_{p,r}$ and $\boldsymbol{S}_{p,\phi}$ are expected to be zero. Contrary, the field parallel component $S_{p,\parallel}$ consists of an oscillation of double the wave frequency ω (Chi and Russell 1998).

The flux of energy density integrated over an integer number of wave periods, nT, is defined by

$$\langle \boldsymbol{S}_p \rangle = \frac{1}{T} \int_0^{nT} \boldsymbol{S}_P \, dt$$ (6.24)

and provides further information about the observed signal. The energy flow of a standing field line oscillation must be directed into both the northern and southern ionospheres, because energy is being dissipated there. On that account a point along the field line must exists where northern and southern energy flow compensates and $\langle \boldsymbol{S}_{p,\parallel} \rangle = 0$. This position is called the field line null point (Allan et al. 1982, Ozeke et al. 2005). Assuming that the ionospheric conductivity is similar at northern and southern footprint of the field line the null point corresponds to the point where the field line intersects the magnetic equatorial plane. Significant differences between both conductivities lead to a shift of the null point into the northern or southern magnetic hemisphere (Ozeke and Mann 2004, Ozeke et al. 2005). Consequently, analyzing the energy flux of an observed signal and taking into account the ionospheric conductivity allows to ascertain its standing wave character and its location compared to the field line null point.

The ionospheric conductivities at northern and southern field line footprints are estimated using the latest empirical standard model of the ionosphere IRI2007 of International Reference Ionosphere (IRI) project (Bilitza 1990, Bilitza and Reinisch 2008). It provides monthly averages of characteristic ionospheric parameters, such as electron density and ion composition, in the altitude range from about 50 km to about 2000 km. It delivers reliable results for the non-auroral ionosphere for magnetically quiet conditions. For given footprint coordinates, time and date the height integrated Pedersen conductivity Σ_P can be obtained from public accessible web interfaces (e.g. http://swdcwww.kugi.kyoto-u.ac.jp/ionocond/sigcal/index.html).

6.5   Wave frequency and amplitude analysis

Spatial structure and temporal evolution of ULF wave activity appears in the time series of magnetic and electric field fluctuations as modulation of their instantaneous amplitude. A method to infer the information about this amplitude $A(t)$ from a monochromatic time series $x(t)$ is the so-called Carson-Gabor method or analytical signal developed by Carson and Fry (1937) and Gabor (1946). Basically, this method can be understand as a transformation

of $x(t)$ from the amplitude-time domain to the amplitude-phase domain. This means that the time series is assumed to be represented by

$$x(t) = A(t) \cos \left[\Phi(t) \right], \tag{6.25}$$

where $\Phi(t)$ is the wave phase. Applying a Hilbert transformation on Eq. 6.25 leads to

$$y(t) = \mathcal{H} \left[x(t) \right] = \int_{-\infty}^{\infty} \frac{x(\tau)}{\pi(t - \tau)} d\tau \tag{6.26}$$

and the complex analytic signal can be expressed as

$$z(t) = x(t) + iy(t). \tag{6.27}$$

Its instantaneous amplitude $A(t)$, wave phase $\Phi(t)$ and wave frequency $\omega(t)$ are given by

$$\begin{aligned} A(t) &= \sqrt{x(t)^2 + y(t)^2} \\ \Phi(t) &= \arctan\left(\frac{y(t)}{x(t)}\right) \\ \omega(t) &= \frac{d\Phi(t)}{dt}. \end{aligned} \tag{6.28}$$

The meaning of the analytic signal for the ULF pulsation analysis can be clarified by applying the method to an artificial signal $x_1(t) = A_1(t) \cos(2\pi f_1(t)t)$ with a linearly increasing frequency from $f_1(t = 0s) = 10$ mHz to $f_1(t = 1000s) = 25$ mHz and a Gaussian amplitude modulation. The time series $x_1(t)$ and the resulting instantaneous amplitude $A_1(t)$, phase $\Phi_1(t)$ and frequency $\omega_1(t)$ are shown in Fig. 6.5. $A_1(t)$ describes the envelope of the signal $x_1(t)$ and thus, can be used to quantify the wave activity of an ULF pulsation. The predetermined frequency $f_1(t)$ is reproduced by applying the Carson Gabor method.

The determination of the analytic signal leads to reliable results only for monochromatic waves (Glassmeier and Motschmann 1995), which is satisfied for most of the observed pulsations in the Pc3 to Pc5 range, as demonstrated for example by the successful application of the Carson-Gabor method to satellite observation of a field line oscillation by Cramm et al. (2000). However, in order to proof the monochromatic wave character a time-frequency analysis method is applied that is based on computing the power spectral density (PSD) of the time series $x(t)$ defined by (e.g. Jenkins and Watts 1969)

$$P_x(\omega) = 2 T \left| x(\omega) \right|^2, \tag{6.29}$$

where $x(\omega)$ denotes the Fourier transformation of the time series and T the length of the time interval. $P_x(\omega)$ describes the distribution of signal energy density in the frequency space. Instead of determining $P_x(\omega)$ for the complete signal the time interval T is separated into M shorter subintervals of the length $\Delta T = T/M$ and the PSD is calculated for each of these. In so doing a dynamical spectrogram is established that gives information about the time dependence of the signal frequency and if multiple frequencies contribute possibly to the fluctuation. Due to the short subintervals the frequency resolution is reduced at the expense of a better time resolution (e.g. Eriksson 1998).
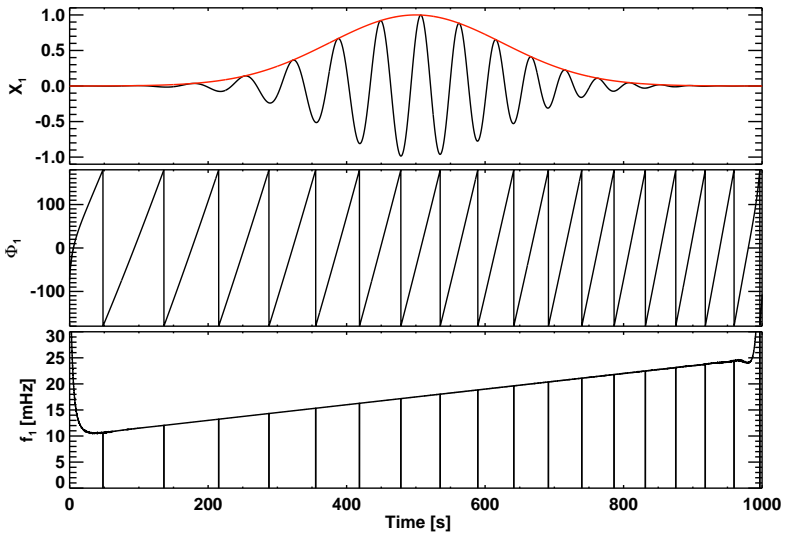
Figure 6.5: Top panel: Time series of an artificial signal with a Gaussian amplitude modulation and linearly increasing frequency. The red line corresponds to its instantaneous amplitude. Middle panel: Instantaneous phase of the artificial signal. Lower panel: Instantaneous frequency of the signal.

7 Case study: Poloidal Alfvén waves inside the plasmasphere

7.1 Cluster location

The first case study discussed under inspection of the theoretical expectations described in Sec. 2 has been detected onboard the Cluster spacecraft on September 15, 2002 between 06:50 and 08:00 UT. The orbits of the four satellites are displayed in Fig. 7.1 projected in the $(XY)_{GSM}$-plane (equatorial plane) and the $(XZ)_{GSM}$-plane. During the time interval of interest the satellites are located in the dayside magnetosphere near magnetic noon. The spacecraft move from the southern magnetosphere into the northern part of the magnetosphere with a velocity of $v_{sc} \approx 2$ km/s. The spacecraft form a large scale tetrahedron with distances between 3000 km and 16000 km. This configuration provides for an opportunity to investigate ULF pulsations simultaneously observed on different field lines by applying a specific analysis method described in detail in Sec. 7.3.

Spatial and temporal parameters of magnetospheric ULF pulsations are controlled by the local background conditions, e.g. plasma mass density and temperature as well as magnetic field strength and curvature (see Sec. 2). An accurate interpretation of the observations requires the knowledge of the magnetospheric region where the Cluster satellites are located. As the perigee of the spacecraft was rather low they most probably entered the terrestrial plasmasphere and traversed the magnetospheric resonator region discussed in Sec. 3.

The radial distance of the plasmapause in the magnetic equatorial plane is determined using the method described in Sec. 6.2.3 to confirm the passage through this resonator region. For the given time interval the activity index $K_p = 3$ indicates quiet and stable solar wind conditions which justifies the assumption of a constant position of the plasmapause in time. For comparison with the Cluster orbits the resulting distribution of the dayside plasmapause is added in Fig. 7.1 (left). The radial distance of the plasmapause near magnetic noon is $L_{pp} = 4.7$ R_E. The field line with the corresponding vertex at $L_{pp} = 4.7$ R_E is assumed as the plasmapause out of the equatorial plane and is indicated by the thick black line in Fig. 7.1 (right). Magnetic field lines have been calculated using the Tsyganenko magnetospheric magnetic field model as described in Sec. 6.2.1 with the following input parameters: a storm time index of $D_{st} = -19$ nT, a solar wind dynamic pressure of $p_{dyn} = 0.85$ nPa and the orientation of the interplanetary magnetic field, $b_{y,imf} = 0.9$ nT and $b_{z,imf} = -0.3$ nT.

The assumed plasmapause location is confirmed by the spacecraft potentials detected with the EFW instruments onboard the four satellites (Fig. 7.2). As the potential U is
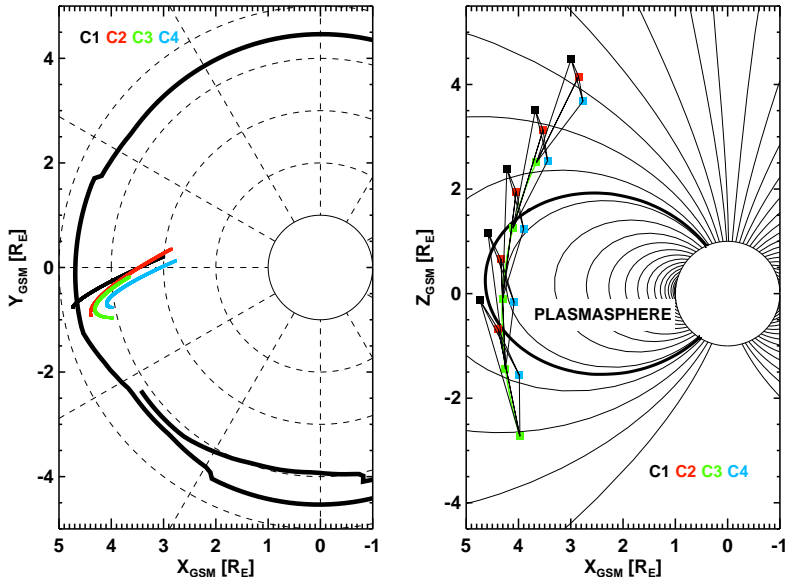
Figure 7.1: The Cluster orbits in the dayside magnetosphere on September 15, 2002, between 06:30 and 08:30. The satellites are located near magnetic noon (left) and move from south to north (right). The thick black line in the left panel represents the plasmapause distribution. In the right panel the field line $L = 4.7$ (thick line) marks the plasmapause out of the equatorial plane.

reverse proportional to the plasma electron density n_e, one would expect a clear change in U during the crossing of the plasmapause due to the large differences in the plasma density between plasmapause and outer magnetosphere. Furthermore, a spacecraft potential of $U < 1$ V is expected inside the plasmasphere (e.g. Gustafsson et al. 2001, Pedersen et al. 2001). The red lines in Fig. 7.2 represent the time intervals when a satellite crosses magnetic L shells lower than the assumed L shell of the plasmapause $L_{pp} = 4.7$. These intervals are in excellent agreement with the times when the spacecraft potential of C2, C3 and C4 is lower than 1 V. Consequently, these three satellites entered the dayside plasmasphere, whereas the orbit of spacecraft C1 was outside the plasmapause. Spacecraft C2 is inside the plasmasphere between 06:37 and 07:15 UT, spacecraft C3 between 07:19 and 08:03 UT and spacecraft C4 between 06:45 and 07:39 UT. Direct measurements of the electron density as well as ion density and plasma composition by the WHISPER (Décréau et al. 2001) and CIS (Rème et al. 2001) instruments, respectively, onboard Cluster do not provide reliable observations for the time period of interest.
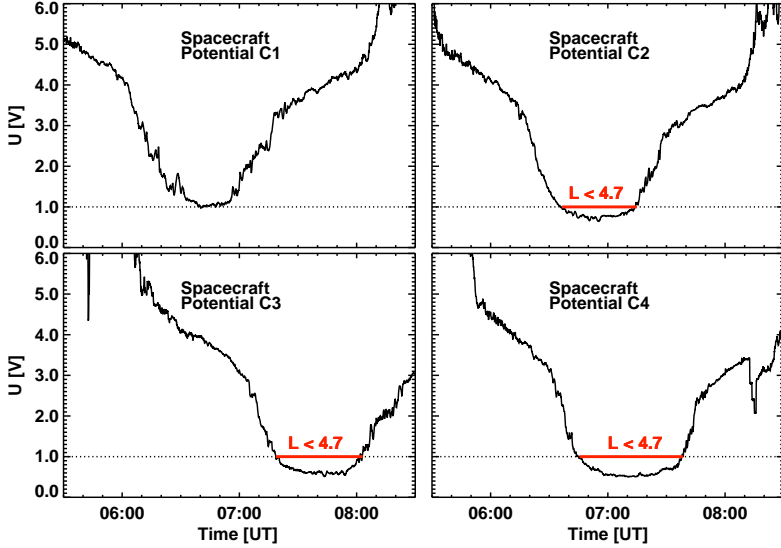
Figure 7.2: Spacecraft potential U detected by Cluster. The red lines mark the time intervals when spacecraft C2, C3 and C4 are located inside of the assumed plasmapause position at $L = 4.7$.

7.2 Observation of ULF pulsation

Magnetic and electric field measurements transformed into the MFA coordinate system (see Sec. 6.3.1) are displayed in Fig. 7.3, where b_r and E_r denote the radial, b_ϕ and E_ϕ the azimuthal and $b_\parallel$ the compressible field perturbations. To discriminate between the four spacecraft they are denoted as C1, C2, C3, and C4, respectively. The pulsation event is most clearly identified in records of spacecraft C3 and C4 with an onset time shift of about 30 minutes (Fig. 7.3). The other two spacecraft only detect minor field perturbations. The frequency of the observed signal is in the range of a Pc4 pulsation, $f \approx 16$ mHz, observed in all components of the magnetic and electric field. The pulsation at spacecraft C3 is detected between 07:20 UT and 08:00 UT with dominating transverse electric and magnetic field variations. The amplitudes of b_ϕ and b_r are modulated exhibiting a maximum of about 4 nT in b_r and nearly constant field after 07:40 UT. The compressible component $b_\parallel$ only shows a small amplitude fluctuation of the order of 1 nT. The electric field oscillates with a maximum amplitude of about 2 mV/m in both components and is almost zero between 07:37 UT and 07:48 UT. At spacecraft C4 the oscillation is seen 30 minutes earlier than at C3 and ceases at about 07:40 UT. Similar to the observation in C3 the pulsation is observable in every component of b and E. At C4 the radial amplitude b_r is twice as large as the azimuthal amplitude b_ϕ and exhibits a peculiar two-wave packet modulation. The
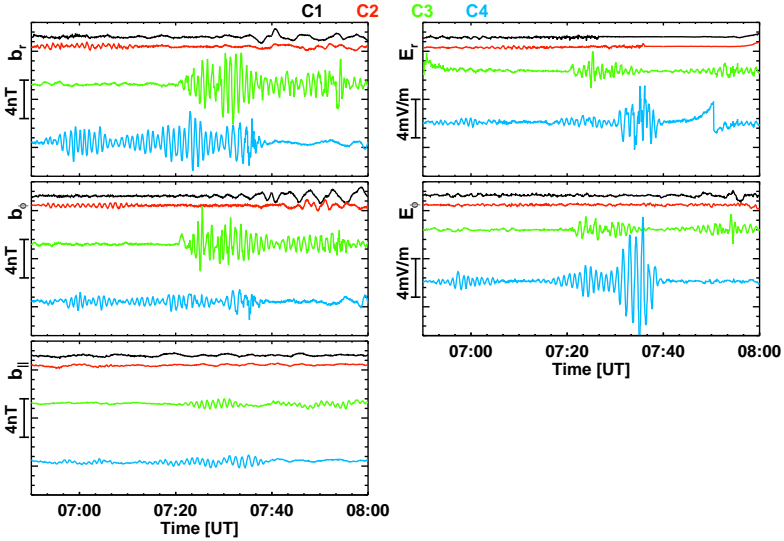
Figure 7.3: FGM and EFW measurements for the four Cluster spacecraft (C1:black, C2: red, C3, green, C4: blue), transformed into a Mean-Field-Aligned coordinate system. The scale denotes amplitudes of magnetic and electric field, respectively.

electric field oscillates again with an amplitude of 2 mV/m and is zero between 07:05 UT and 07:18 UT, whereas the amplitude increases in both components after 07:30 UT up to 5mV/m in E_ϕ and 10mV/m in E_r.

Further information about the observed signal is provided by the Poynting vector $\boldsymbol{S}_p$ and the time-average energy flux $\langle \boldsymbol{S}_p \rangle$ determined using Eqs. 6.23 and 6.24, respectively. Here $\langle \boldsymbol{S}_p \rangle$ is calculated by averaging over the wave period $T = 67$ s. Indications for the existence of a standing wave, i.e. a vanished time-average energy flux and fluctuation in $S_{p,\parallel}$ (see Sec. 6.4), are especially observed until 07:20 UT in spacecraft C4. After that time the character of the energy flux changes with both transverse components now indicating a non-zero energy flux transverse to the ambient magnetic field. In particular, the large negative radial component S_r corresponds to an inward directed energy transport indicating the presence of a propagating wave. The wave as observed by spacecraft C3 exhibits small variations of the transverse energy flux $\langle S_r \rangle$ and $\langle S_\phi \rangle$. The field parallel energy flux is non-zero between 07:20 and 07:34 UT, but the oscillating component of $S_\parallel$ is dominant. A non-zero component $\langle S_\parallel \rangle$ is expected for a standing poloidal wave in case of asymmetric ionospheric conductivities at the northern and southern footprint of the oscillating field lines (Ozeke et al. 2005). Using the Tsy96 magnetic field model (see Sec. 6.2.1) the geographic footprint coordinates of the field line crossed by spacecraft C4 at 07:00 UT have been identified as 64° N, 61° E for the northern footprint and 49° S, 61° E for the southern footprint. The northern ionospheric height integrated Pedersen conductivity is
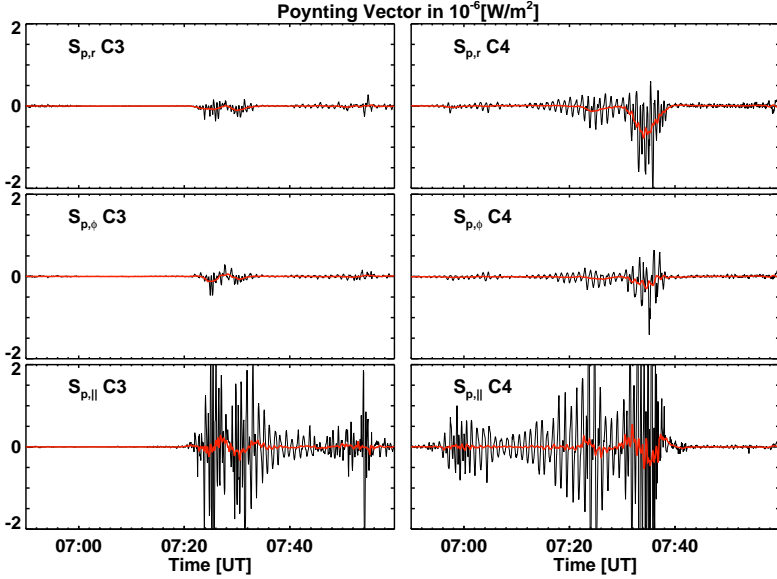
Figure 7.4: Components of the Poynting vector S_p observed by spacecraft C3 and C4. The red line represents the time-average energy flux.

$\Sigma_{P,N} = 9.1$ S, the southern conductivity $\Sigma_{P,S} = 11.7$ at this time. At the footprints of the field line crossed by spacecraft C3 at 08:00 UT (coordinates 65° N, 55° E and −51° S, 76° E) the conductivities found are $\Sigma_{P,N} = 9.1$ S and $\Sigma_{P,S} = 13.1$ S. Consequently, the small but significant non-zero component $\langle S_\parallel \rangle$ is supposed to be a consequence of the slightly different ionospheric conductivities at northern and southern field line footprints. We conclude that at this time interval an almost standing field line oscillation is observed by spacecraft C3 as well as spacecraft C4 between 06:50 and 07:20 UT.

7.3   Spatio-temporal structure

The orbital coordinates of the different spacecraft are transformed into the LDM coordinate system as defined in Sec. 6.3.2. Fluctuations of the electromagnetic field are still represented using the Mean-Field-Aligned coordinate system. At first we concentrate on the actual observations of b_r and $\langle S_{p,r} \rangle$ in the L-D plane as seen in the upper panels of Fig. 7.5. Effects of minor changes in the M coordinate (lowest panel of Fig. 7.5) are discussed later. For the representation of b_r the Carson-Gabor representation is used (see Sec. 6.5), which allows to determine instantaneous amplitude and phase of the given time series. As the ULF signals to be analyzed here are rather regular the analytic signal representation is a very suitable tool. The thickness of the lines denoting the spacecraft positions in the first

panel of Fig. 7.5 represents the instantaneous amplitude or signal envelope of the dominant radial component of the magnetic field oscillation. The width of the lines in the second panel of Fig. 7.5 is related to the radial component of the time averaged energy flux $\langle S_r \rangle$. The vertical black line in Fig. 7.5 represents the plasmapause position, previously also given in Fig. 7.1. Wave activity occurs preferentially within the plasmasphere.

In the present case study each spacecraft covers different ranges of L-values. The magnetic equator (D = 0) is crossed by spacecraft C4 at the field line with its vertex at $L = 4.1$, C3 at $L = 4.35$, C2 at $L = 4.45$, and C1 at 4.77, that is the four spacecraft cover a radial extent of about 0.67 R_E, a value comparable to earlier estimates of the radial extent of magnetospheric pulsations. Therefore, the configuration is suitable to analyze the poloidal oscillation.

Information about the time at which a spacecraft crossed a specific field line is of particular interest. Spacecraft positions at five selected times, labeled by roman numbers, are marked by squares in Fig. 7.5. These times have been selected as they correspond to those times when spacecraft C4 and C3 cross the L = 4.22 and L = 4.4 field lines in the southern and northern hemisphere and the time spacecraft C4 detects the maximum, radially directed energy flux.

At time I spacecraft C4 observed an amplitude maximum at $L = 4.22$; the wave amplitude decreased while spacecraft C4 moved to lower L-values and increased after it crossed the magnetic equator $D = 0$ R_E. Spacecraft C1 and C2 were located far away from this field line at $L > 4.45$ and did not detect pulsations as seen in the magnetic and electric field measurements (Fig. 7.3). We conclude that at time I the radial spatial extent of the pulsation event was too small to be observed by C1 and C2. Afterwards both spacecraft move further apart from the region of interest and in the following we concentrate on the observations of spacecraft C3 and C4. C3 was still too far away from the region of interest to detect any ULF signal at time I.

At time II another amplitude maximum was observed by C4 at the same field line $L = 4.22$ as at time I. This clearly indicates the existence of a radially localized wave structure along this field line oscillating for at least 24 minutes. At time II a pulsation was also detected by spacecraft C3, but at $L = 4.5$ indicating a more complex radial structure of the wave field observed by the two satellites.

At time III C3 and C4 were located at the same field line shell $L = 4.4$, but at slightly different M values. Approaching this field line shell C3 saw an increasing amplitude, indicating a localized wave packet. At the same time C4, moving towards the plasmapause only detected a minor change of the field amplitude. This difference in the amplitude behavior might be due to rapid azimuthal variations of the wave field.

After time III spacecraft C4 recorded regular fluctuations for about 10 minutes between $L = 4.4$ R_E and $L = 4.6$ R_E; these were not observed at any of the other spacecraft as they were located at other field lines. This period of regular oscillations ceased when C4 reached the plasmapause region.

Between time I and time III the time averaged Poynting vector $\langle S \rangle$ is close to zero indicating the existence of a standing wave field structure. Afterwards spacecraft C4 observes an increasing radial energy flux with its maximum at time IV located at $L = 4.55$ and $D = 1.4$ R_E. At the same time spacecraft C3 observes $\langle S_r \rangle = 0$ at $L = 4.36$ and $D = -0.3$ R_E. Spacecraft C4 seems to transit a wave propagating in a defined region as no energy flux is observed by spacecraft C3. One can speculate that a wave source is located
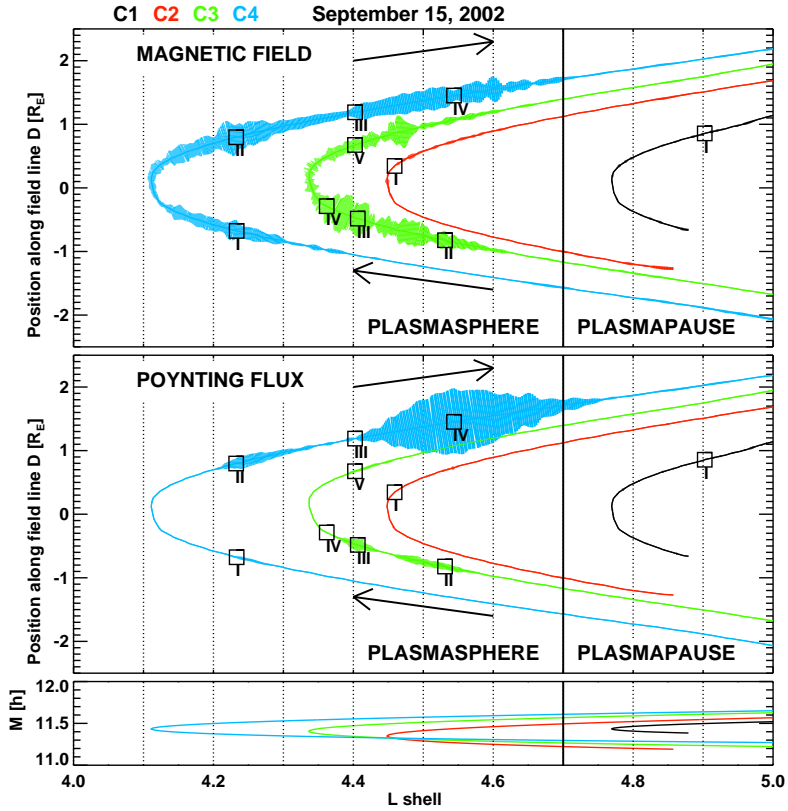
Figure 7.5: Positions of the Cluster spacecraft in the L-D coordinate system at different times, where the squares mark the positions of each spacecraft. Time I corresponds to 06:58:38 UT, time II to 07:23:42 UT, time III to 07:30:22 UT, time IV to 07:34:22 UT and time V to 07:50:06 UT. The arrows show the flight direction of the Cluster satellites. The thickness of the lines are related to the amplitude of the radial oscillation of the magnetic field b_r (upper panel) and the radial component of the time averaged Poynting vector $\langle S_r \rangle$ (second panel). The bottom panel shows the orbit in the L-M plane, where M corresponds to the magnetic local time MLT.
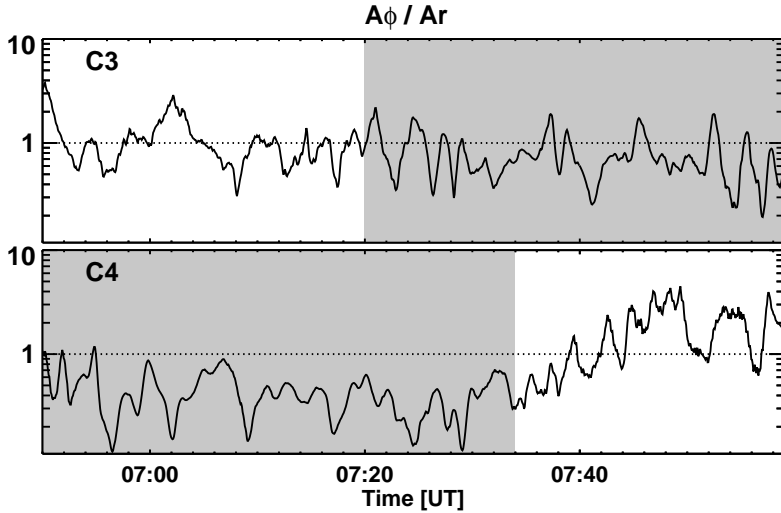
Figure 7.6: Ratio of poloidal and toroidal instantaneous amplitudes for time series of spacecraft C3 and C4. The grey shaded areas mark the time intervals when standing field lines are detected.

near the observed maximum of the energy flux. The nearby plasmapause at $L = 4.7$ acts as a very good wave reflector for the excited wave (e.g. Lee 1996) which can thus only propagate towards lower L shells; this is a probable explanation for the observed radially inward directed energy flux. At time V spacecraft C3 again crossed the $L = 4.4$ field line. However, the amplitude was smaller than during the southern crossing, which indicates a temporal variation of the pulsation activity rather than a spatial one. All other spacecraft had already left the activity region at this time.

As discussed in Chapter 4 poloidal Alfvén waves are expected to be transformed to toroidal waves in the course of time. This change in wave polarization can be identified in the time series of the magnetic field observation by introducing the ratio of the instantaneous toroidal amplitude A_ϕ to the instantaneous poloidal amplitude A_r. The resulting values A_ϕ/A_r are shown in Fig. 7.6 for spacecraft C3 and C4 observations during the time interval under investigation. In both cases $A_\phi/A_r < 1$ hold while oscillations with a standing wave character are detected. The average level of this ratio is slightly higher in the time series of C3 indicating that here the toroidal component is closer to the poloidal one than in the time series of spacecraft C4 (see also Fig. 7.3). A significant increase of A_ϕ/A_r is not apparent in both time series, i.e. a transformation of wave polarization cannot be identified for the standing Alfvén waves. However, when spacecraft C4 detects the radial directed energy flux, as described above, A_ϕ/A_r rises from 0.4 to approximately 1. Apparently, the end of the pulsation lifetime accompanies with radial wave propagation away from the outer barrier, the plasmapause. Unfortunately, all satellites besides C4 are
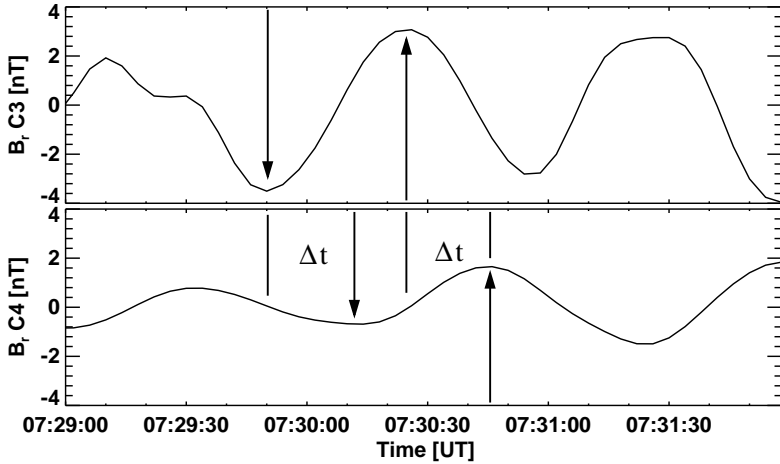
Figure 7.7: Time series of b_r for spacecraft C3 (top) and C4 (bottom) between 07:29 and 07:32 UT, where both satellites cross the same L-shell at different azimuthal positions M.

located at other field lines during this short time interval and, thus, a multi-point analysis of this situation is not possible.

7.4 Azimuthal wave number

A typical feature of poloidal Alfvén waves is a small-scale spatial structure associated with a large azimuthal wave number m. The knowledge of the phase difference $\Delta\Psi$ of signals observed by two different satellites allows an estimation of this number:

$$m = \frac{\Delta\Psi}{\Delta\Phi} = \frac{360°}{\Delta\Phi}\frac{\Delta t}{T},\qquad(7.1)$$

where $\Delta\Phi$ is the spatial separation between the two satellites in the azimuthal direction, Δt the time difference between points of the same wave phase and T the wave period (e.g. Eriksson et al. 2005a, Schäfer et al. 2008). A variation of the magnetic field $b \propto \exp(im\Psi)$ is assumed. High resolution magnetometer data (10 Hz) are used to estimate the phase difference in the b_ϕ component of two satellites observed between 07:29 and 07:32 UT, where the data are bandpass filtered between 5 mHz and 50 mHz (Fig. 7.7).

At time III spacecraft C3 and C4 are located on the same L shell, $L = 4.4$ (see Fig. 7.5). The angle in the azimuthal direction between the two satellites is $\Delta\Phi = 3.18° \pm 0.01°$. The time difference Δt between minima and maxima, respectively, is about 18 s (Fig. 7.7), which corresponds to $\Delta\psi \approx 100°$, as the wave period is $T = 1/f_{obs} = 63$ s. Assuming an uncertainties in Δt of $\delta t = 0.2$ s due to the temporal resolution of the time series and in T of $\delta T = 1 s$ the law of error propagation can be applied to Eq. 7.1. Accordingly, the

azimuthal wave number for the analyzed wave is $m = 30 \pm 2$. The corresponding azimuthal wavelength is $\lambda = 2\pi/k_\phi \approx 5900$ km with $k_\phi = m/L$. Such large azimuthal wave numbers are expected for poloidal oscillations (e.g. Radoski 1967) and observed by Eriksson et al. (2005b) recently.

7.5   Wave Frequency

Phenomenological characteristics of the waves observed in the outer region of the plasmasphere are quite complex as discussed above. The wave frequency, however, is rather stable at $f_{obs} = 16$ mHz during the time spacecraft C3 and C4 traversed this region, as seen in the dynamic spectra of the radial magnetic field component b_r (Fig. 7.8). Due to the radial spacecraft motion a frequency constant in time is equivalent to a uniform frequency with respect to magnetic L shells, which has been previously observed and discussed for poloidal wave events in outer magnetospheric regions ($L > 6$) by Denton et al. (2003). Contrary to that the frequency of toroidal waves is expected to have a L dependence and consequently the radial structure of the here observed poloidal wave event cannot be explained by the field line resonance mechanism. Details of the radial structure of poloidal waves can be gained by comparing the observed frequency with the radial profile of theoretically expected poloidal and toroidal eigenfrequencies (e.g. Denton and Vetoulis 1998, Klimushkin 1998b).

At first the eigenfrequencies Ω_T and Ω_P are estimated using the WKB approximation, i.e. Eqs. 2.21 and 2.28 are applied, respectively. For this purpose necessary plasma background parameters, e.g. distribution of magnetic field, current density and plasma density, are determined as introduced in Sec. 6.2. The radial and field aligned profiles of the magnetic field are calculated by the Tsy96 model (Tsyganenko and Stern 1996) for the input parameters $p_{dyn} = 0.85$ nPa, $D_{st} = -19$ nT, $b_y^{sw} = 0.9$ nT and $b_z^{sw} = -0.3$ nT. The radial plasma pressure profile $P(L)$ is calculated using Eq. 6.12 with $L_0 = 2.9$ R_E and $W = 1.9$ R_E. The maximum plasma pressure $P_0 = P(L_0)$ is selected so that at L_0 the plasma β is 0.035. For this set of parameters the current density $J_\perp(L)$ determined by Eq. 6.13 coincides with the current density obtained from the Tsy96 model (Eq. 6.11). The resulting radial profiles of β, P and $J_\perp$ are displayed in Fig. 7.9 corresponding to expected profiles during low geomagnetic activity (e.g. Lui and Hamilton 1992).

The plasma number density along the field line is assumed as the power law Eq. 6.19 with an exponent $\alpha = 1$ typical for the plasmasphere (e.g. Goldstein et al. 2001, Denton et al. 2004). The number density in the equatorial plane n_{eq} can be obtained from the model of Carpenter and Anderson (1992) (see Sec. 6.2.3). Influences on n_{eq} due to complex features of the plasmapause formation such as plasma plumes or shoulders (e.g. Pierrard and Lemaire 2004, Goldstein 2006) are not predicted by the applied simulation of the plasmapause formation, additionally approved by the observed spacecraft potential (Fig. 7.2). The plasma of the plasmasphere is composed of hydrogen and heavier ions such as helium and oxygen. This requires a mass correction factor m_{corr} to calculate the plasma mass density $\rho(s) = n(s)m_{corr}m_p$ accurately, where m_p is the proton mass. The typical plasmaspheric ion composition lead to a mass correction of $m_{corr} \approx 3$.

With these assumptions and model values the eigenfrequencies of the fundamental poloidal and toroidal field line oscillation, $f_P = \Omega_P/2\pi$ and $f_T = \Omega_T/2\pi$, as well as the
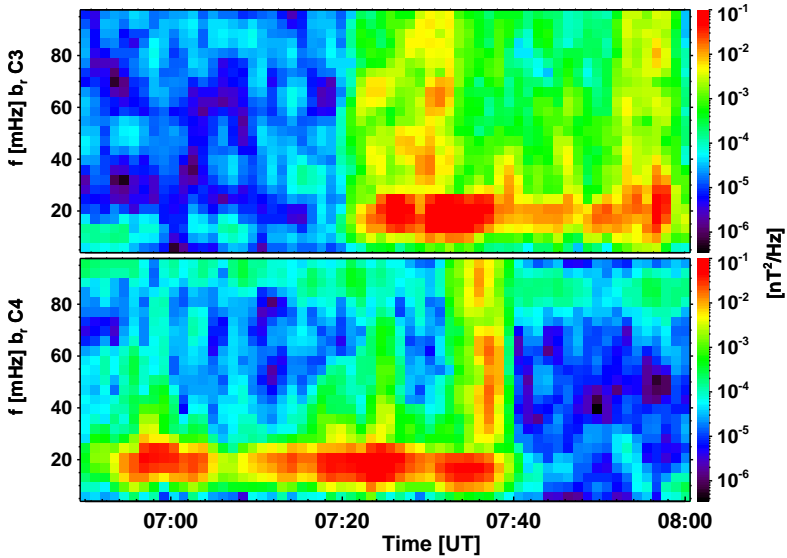
Figure 7.8: Dynamic spectra of the radial magnetic field components b_r of the spacecraft C3 (top) and C4 (bottom) observations.

frequencies of their harmonics $N = 2, ..., 4$ have been calculated for L shells in the range [2.5, 5.5] R_E (Fig. 7.10). In this region and in particular at L shells $L = [4.1, 4.7]$, where spacecraft C3 and C4 observe the described pulsation activity, poloidal eigenfrequencies are larger than the toroidal eigenfrequencies. The theoretical framework predicts the existence of a region transparent for poloidal waves near a minimum of f_P only if the condition $f_P < f_{obs} < f_T$ is satisfied (Klimushkin et al. 2004). In contrast to that $f_T < f_P < f_{obs}$ is found. In Schäfer et al. (2007) it has been suggested that the reason for this discrepancy is due to the power law assumed for the field aligned density distribution (Eq. 6.19) with $\alpha = 1$. In this case the second term on the right hand side in Eq. 2.28 can become negative for certain radial distances that results in $\Omega_P > \Omega_T$. It has been assumed that the WKB approximation does not lead to reliable results for the field line eigenfrequencies.

This evident difficulties are avoided when determining f_P and f_T with the numerical method introduced in Sec. 6.1. The resulting radial frequency profiles are shown in Fig. 7.11 (left), where the same plasma parameters are considered as described above (Fig. 7.9). As apparent in the fundamental harmonic f_T exceeds f_P only at magnetic shells below $L = 3.5$, while at higher L shells, where the pulsation is detected, the poloidal frequency is still larger than the toroidal one. In order to clarify the influence of the plasma pressure the eigenfrequencies are additionally calculated for $\beta = 0$ (Fig. 7.11, right). In this case $f_P < f_T$ holds over the complete range of L shells best visible in the fundamental and second harmonic frequencies, as field line curvature reduces f_P (see Sec.
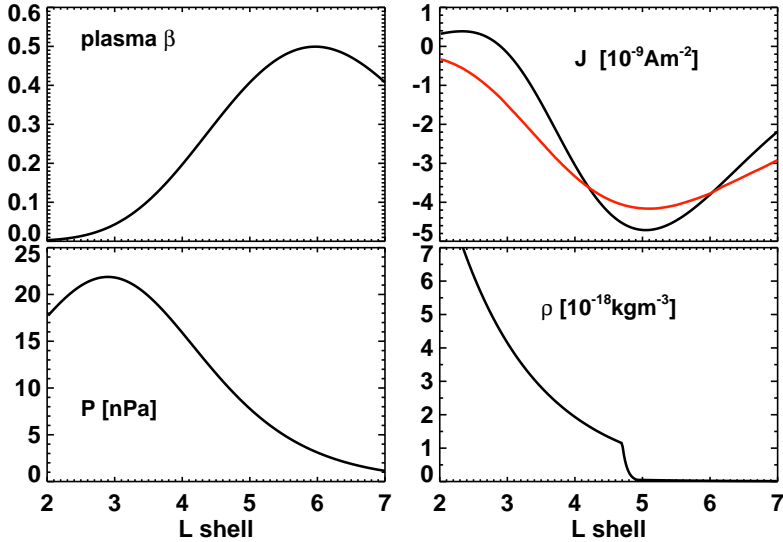
Figure 7.9: Profiles of plasma properties. Plasma pressure and plasma β are assumed for quiet geomagnetic activity (Lui and Hamilton 1992). The current density is obtained from the Tsyganenko '96 model (red line). Positive values of $J_\perp$ correspond to a current directed eastward. The plasma mass density is calculated from modeling the electron number density (Carpenter and Anderson 1992).

2.3). Consequently, the numerical calculation of the eigenfrequencies is not capable to resolve the discrepancy between theory and observation. For this particular case study $f_P > f_T$ is found considering realistic plasma background conditions as described above.

However, the theory used here describes wave fields bounded by surfaces satisfying the condition $f_{obs} = f_P$. These surfaces act as turning points of the radial propagating wave and define a region transparent for poloidal waves. Consequently, we assume that the observed pulsation is localized within such a wave transparency region despite the contradiction between observation and theory. We suggest that Fig. 7.10 reflects the radial width of the poloidal resonator (e.g. Leonovich and Mazur 1993). The outer boundary coincides with the plasmapause at $L \approx 4.7$ and the inner boundary depends on the harmonic number N. Since spacecraft C4 observes the pulsation even at $L = 4.1$, we exclude the fourth harmonic oscillation, which has the inner resonance surface located at $L \approx 4.2$. The observations described in the L-D coordinate system (Fig. 7.5) reveal a symmetric amplitude structure relative to the magnetic equator $D = 0$ R_E suggesting an oscillation with an odd harmonic number. For the fundamental oscillation $N = 1$ the spatial extent of the oscillating structure would be more than 2 R_E. Consequently, we suggest that the observed pulsation is a third harmonic oscillation with a spatial extent of approximately 0.7 R_E.
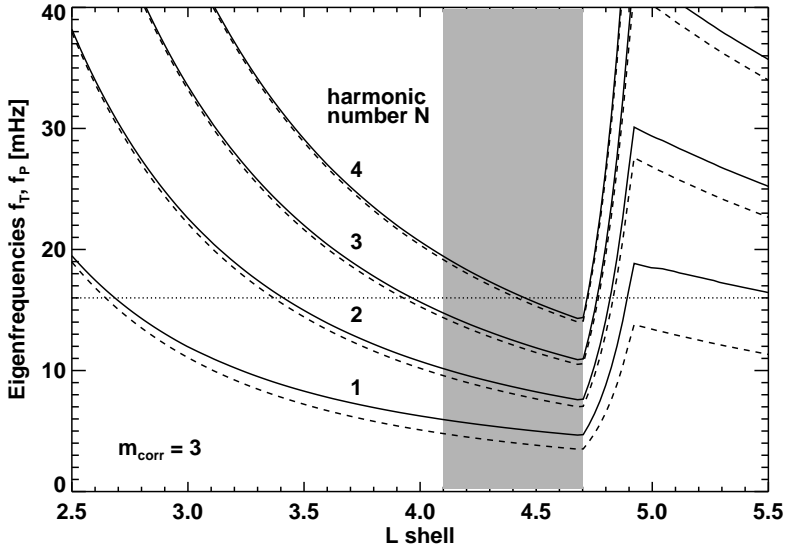
Figure 7.10: Profiles of the poloidal eigenfrequencies f_P (solid lines) and toroidal eigenfrequencies f_T (dashed line) of magnetospheric field lines calculated for harmonic numbers $N = 1, ..., 4$ and the mass correction factor $m_{corr} = 3$. The dotted line marks the observed frequency $f = 16$ mHz. The grey shaded background marks L-shells crossed by spacecraft C3 and C4 during the analyzed time interval.

7.6 Modeling the Spatio-temporal Structure

For further understanding of the observed pulsation event and to reach a deeper insight into its spatio-temporal structure we present a simple model for the spatio-temporal characteristics of the wave which is fitted to the actually observed data for better comparison. The dominant poloidal magnetic field component is given by

$$b_{r,model} = b_0 \cdot A(D, \phi) \cdot B(L) \cdot C(t). \tag{7.2}$$

Here $A(D, \phi)$ describes the spatial structure along the field line and in the azimuthal direction, $B(L)$ is the spatial structure in the radial direction across L-shells, and $C(t)$ is the temporal evolution of the wave amplitude. All three amplitude functions are normalized to 1, so that the maximum amplitude of the modeled signal is given by b_0.

The model assumes a standing wave along the background magnetic field line:

$$A(D, \phi) = \sin(k_\parallel D + m\phi) \cdot \cos(\omega_P t). \tag{7.3}$$

This functional form describes odd mode oscillations with $k_\parallel$ denoting the field parallel wave number. Wave frequency $\omega_P = 2\pi f_P$ and azimuthal wave number m are determined
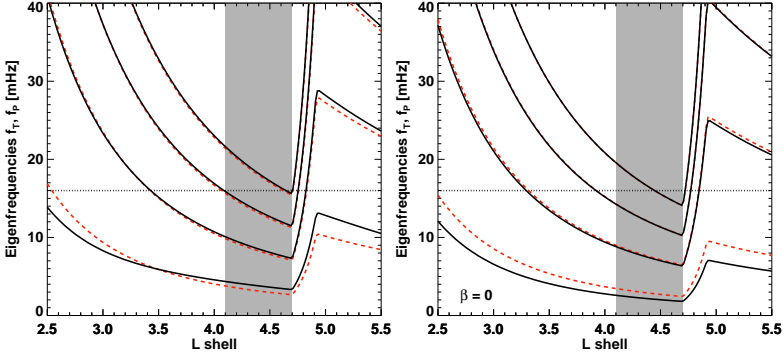
Figure 7.11: Numerically calculated poloidal eigenfrequencies f_P (solid lines) and toroidal eigenfrequencies f_T for given plasma background parameters (left) and assuming zero plasma pressure (right). The dotted lines marks the observed frequency $f = 16$ mHz. The grey shaded background marks L-shells crossed by spacecraft C3 and C4 during the analyzed time interval.

using the observations. As mentioned in Sec. 7.2 the change in the azimuthal spacecraft position $\Delta\phi = \Delta M$ is small, but since we found $m \approx 30$, the phase variation $\Delta(m\phi)$ is not negligible. The parallel wavelength $\lambda_\parallel = 2\pi/k_\parallel$ depends on the length of the field line l and the harmonic number N: $\lambda_\parallel = 2l/N$. The lengths of the field lines with vertices between $L = 4.1$ R_E and $L = 4.7$ R_E are between $l = 9.4$ and $l = 10.0$ R_E. Assuming a third harmonic oscillation as discussed above gives one wavelengths in the range $\lambda_\parallel = [6.3, 6.7]$ R_E or wave numbers $k_\parallel = [0.94, 1.00]$ R_E^{-1}.

The transverse variation of the wave field is described by multiplying the standing wave (7.3) with an amplitude function $B(L)$. Leonovich and Mazur (1990) have shown that for a poloidal wave resonator the function $B(L)$ can be approximated by the product of a Hermitian polynomial H_n of order n and a Gaussian:

$$B(L) = H_n(\xi) \exp(-\xi^2/2), \tag{7.4}$$

where $\xi = (L - L_R)/\sigma$. Here L_R denotes the location of maximum wave amplitude and σ describes the radial width of the wave field within the wave guide region, respectively. For a zeroth order Hermitian polynomial ($n = 0$) the radial structure $B(L)$ is just given by a Gaussian as already observed for poloidal pulsations (e.g. Cramm et al. 2000).

Using higher order Hermitian polynomials allows to describe a more complex wave field variation in radial direction as the number of extrema of the polynomial used is equal to $n + 1$. Fig. 7.5 exhibits two amplitude maxima at $L = 4.22$ and $L = 4.40$ R_E. The first one at $L = 4.22$ R_E is detected twice by spacecraft C4 when it crosses the corresponding field line below and above the magnetic equator. The second one at $L = 4.40$ R_E is detected only by C3. Due to this observation a first order Hermitian polynomial with $n = 1$ is used in Eq. 7.4.

The amplitude maxima on the field line $L = 4.22$ R_E are observed at $D = -0.7$ R_E and $D = 0.9$ R_E, that is almost symmetric with respect to the magnetic equator. Assuming a
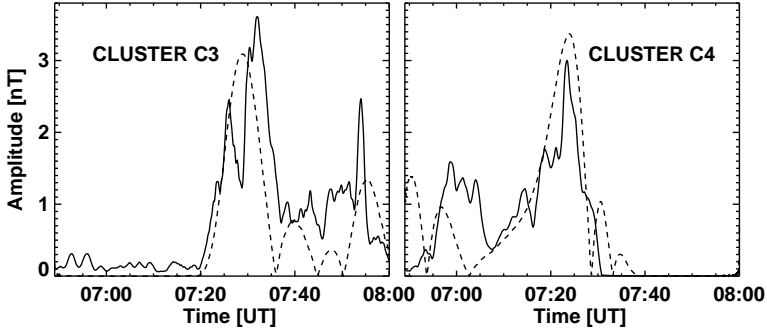
Figure 7.12: Comparison between measurements of the b_r (solid line) component and the model of the wave field $b_{r,model}$ (dashed line).

standing wave, one would expect nearly the same pulsation strength for both crossings. However, the opposite is observed with the northern maximum displaying a somewhat small amplitude value (Fig. 7.5). This is either due to the symmetry point not coinciding with the magnetic equator or the result of a temporal evolution of the wave field, approximated by a Gaussian function $C(t)$ with its maximum at 07:32 UT corresponding to the observed maximum of the signal. An increasing amplitude can be explained by e.g. drift bounce resonance effects, as described in Klimushkin and Mager (2004). On the other hand, wave dissipation at the ionospheric boundaries leads to a decreasing pulsation amplitude.

The aim of our modeling effort is to characterize the amplitude b_0, the activity maximum position L_R and its width σ. Varying these model parameters the best correspondence between modeled signal and the actual observations of spacecraft C3 and C4 have been reached for $L_R = 4.35$ R$_E$, $\sigma = 0.1$ R$_E$, $m = 30$, and $b_0 = 6.5$ nT. A comparison of both signals is displayed in Fig. 7.12. The correspondence is fairly reasonable with major features of the observed amplitude modulation being explained. However, it is not possible to reproduce the measurements in detail. The first amplitude maximum observed at spacecraft C4 is not fully reproduced by the model such as the amplitude modulation seen in C3 after 07:35 UT. Observations between 07:10 and 07:35 UT are well represented by the modeled signal. Especially the modeled shape of the second amplitude peak in spacecraft C4 is in a good agreement with the observed amplitude modulation.

Fig. 7.13 shows a comparison between the modeled radial variation of the wave field and the radial variation of the poloidal eigenfrequency. It is remarkable to see that the wave activity region as modeled well coincides with the wave guide region identified as the trough in the poloidal eigenfrequency variation. From the modeled signal we also infer that the total width of the wave guide is about 0.6 R$_E$, which corresponds to the observed extend of the wave activity region.

It should be noted that the time interval between 07:30 and 07:40 UT of the spacecraft C4 observation is excluded from our modeling efforts as at this time a propagating wave is detected (Figs. 7.4 and 7.5) and the assumption of a standing wave is not suitable in this
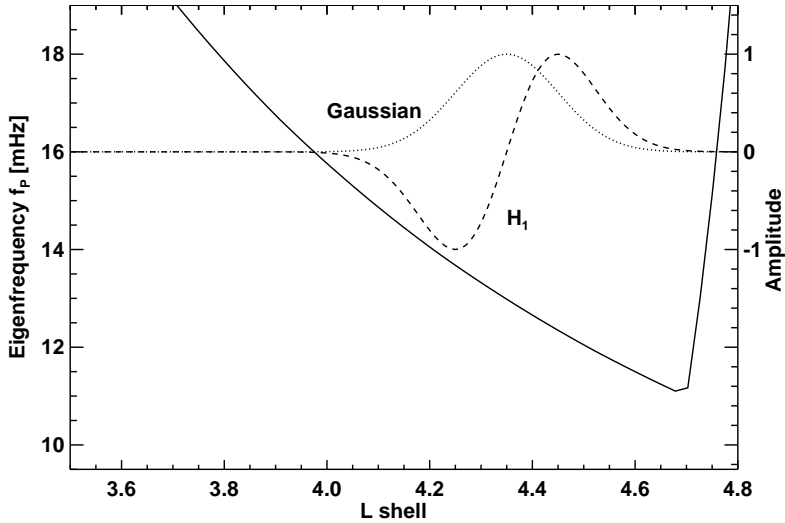
Figure 7.13: Comparison between the modeled radial variation and the radial variation of the poloidal eigenfrequency.

region.

Differences between model and measurements originate from several sources. First, the Hermitian function used to describe the radial structure is based on the assumption of a wave guide symmetric to the point of minimum eigenfrequency. This assumption is not fully consistent with the actual variation of the poloidal eigenfrequency. Second, theoretical studies such as presented by Klimushkin and Mager (2004) assume a constant wave amplitude in time. A more realistic temporal evolution of the wave field is not incorporated in current theoretical treatments. We think that this oversimplification is the main reason for discrepancies between model and observation. However, similarities found suggest that the theoretical assumptions allow for explaining the observed amplitude modulation, at least after the wave field is fully developed and before it collapses due to ionospheric dissipation.

7.7   Summary

The field line oscillations analyzed were observed in the time interval September 15, 2002, 06:50 - 08:00 UT. The large scaled spacecraft configuration during this interval has entailed the possibility to record the pulsation event over a time period of around 70 minutes in spacecraft C3 and C4. During this time the spacecraft crossed the oscillating field lines twice during their inbound and outbound approaches to the Earth on an almost polar orbit.

Analyzing the phase differences between signals observed by two spacecraft while

passing the same L shell has given us the possibility to estimate the azimuthal wave number; we found $m \approx 30$. Accordingly, a poloidal polarized oscillation with $m \gg 1$ was detected.

To describe temporal and spatial properties of the observed wave field we have used a theoretical framework developed by Leonovich and Mazur (1990, 1993, 1995) and Klimushkin (1998a). A profile of poloidal eigenfrequencies f_P was evaluated based on realistic assumption concerning plasma composition and plasma properties in the region of interest. The comparison with the observed frequency $f_{obs} = 16$ mHz has suggested a third harmonic oscillation.

The wave field was found localized near the minimum of f_P bounded by turning points $f_P = f_{obs}$ at the plasmapause and within the plasmasphere, respectively. In this region the existence of a localized pulsation is not fully predicted by theory. Hence, further efforts on the theoretical description of plasmaspheric ULF pulsations are necessary.

Modeling spacecraft observations of plasmaspheric field line crossing has suggested a spatial structure and temporal development of the detected wave field. We have found clear indications of the existence of a standing wave at $L = 4.22$ R_E together with a complex radial structure extended to higher L-shells. The wave event is localized in radial direction. However, this localization is not due to any resonant mode coupling, but thought to be the result of the wave field encountering two poloidal turning points, much as predicted by Klimushkin (1998a). The spatial extent of the wave field area is around 0.6 R_E, which confirms previous observations of plasmaspheric ULF pulsations (Ziesolleck et al. 1993, Menk et al. 1999). The radial structure was described by a specific function as suggested by Leonovich and Mazur (1990). In addition to the standing structure the investigation of the wave's Poynting vector has clearly exposed the existence of an inward directed, propagating wave.

Comparing observations with the modeled standing oscillation exposes strengths and weak points of the applied model and its theoretical basis. For the given situation of a solely poloidally polarized field line oscillation a theory is currently unavailable specifying the temporal evolution of such a wave field. Thus, the measured pulsation can only be reproduced in parts by the modeled standing structure.

8 Case study: Poloidal Alfvén waves near the plasmapause

8.1 Cluster location

The second ULF wave event was detected on August 8, 2003, between 07:40 and 08:20 UT. The Cluster orbits in GSM-coordinates are shown in Fig. 8.1. The satellites are located in the dayside magnetosphere at a magnetic local time of $MLT \approx 14$ h and move from the southern magnetosphere into the northern part of the magnetosphere with a velocity of $v_{sc} \approx 2$ km/s. In contrast to the previous case study (Sec. 7), the four satellites form a small scaled tetrahedron: the distances between the spacecraft are between 200 km and 1000 km allowing a detailed analysis of spatial properties of the detected pulsation (see Sec. 8.3 and 8.5).

The radial distance of the plasmapause in the magnetic equatorial plane is determined using the method described in Sec. 6.2.3 using the activity index $k_p = 3$ as input parameter. At the azimuthal position of the Cluster orbit, $MLT \approx 14$ h, the plasmapause is found at a radial distance of $L = 4.3$ R_E. The field line with the corresponding vertex at $L_{pp} = 4.23$ R_E is assumed as the plasmapause out of the equatorial plane and is indicated by the thick black line in Fig. 8.1 (right). Magnetic field lines have been calculated using the Tsyganenko magnetospheric magnetic field model as described in Sec. 6.2.1 with the following input parameters: a storm time index of $D_{st} = -7$ nT, the solar wind dynamic pressure of $p_{dyn} = 0.85$ nPa and the orientation of the interplanetary magnetic field, $b_{y,imf} = 6.0$ nT and $b_{z,imf} = 5.0$ nT. This set of parameters indicates quiet and stable solar wind conditions which justifies the assumption of a constant position of the plasmapause in time.

During the time interval of interest the spacecraft closely approach the plasmapause location. However, the exact position of the satellites with respect to the boundary layer has to be inferred from the measurement of the spacecraft potentials U as shown in Fig. 8.2. Neither the characteristic change in U while crossing the plasmapause nor the condition $U < 1$ V expected within the plasmasphere (e.g. Gustafsson et al. 2001, Pedersen et al. 2001), as observed for the first case study (Fig. 7.2), are detected by one of the four satellites. Consequently, it is assumed that during the time period of interest Cluster is located outside the plasmasphere near the magnetospheric resonator region at the maximum Alfvén velocity (see Sec. 3).
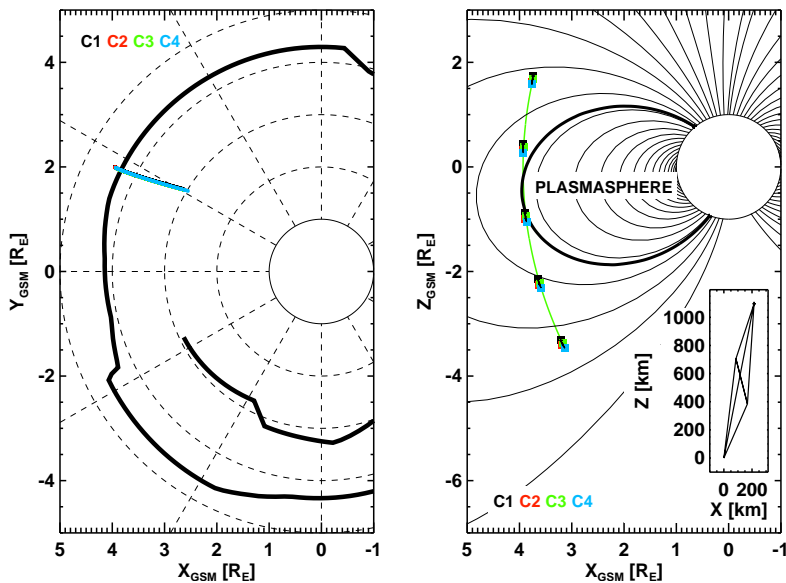
Figure 8.1: The Cluster orbits in the dayside magnetosphere on August 7, 2003, between 07:00 and 09:00. The satellites are located at magnetic local time 14 h (left) and move from south to north (right). The thick black line in the left panel represents the plasmapause distribution. In the right panel the field line $L = 4.23$ marks (thick line) marks the plasmapause out of the equatorial plane.

8.2   Observation of ULF pulsation

Fig. 8.3 shows observations of the magnetic and electric fields from all four Cluster spacecraft. The first three panels exhibit the magnetic field components, b_r, b_ϕ and $b_\parallel$. The latter component has been defined by subtracting the mean magnetic field from the field aligned component to identify perturbations parallel to $\boldsymbol{B}$. The lower two panels display the electric field components E_r and E_ϕ, respectively. To describe the electric field perturbations we assume that $\boldsymbol{E} \cdot \boldsymbol{B} = 0$, that is no field-aligned electric field component exists. The wave frequency is rather stable at $f = 23$ mHz during the time Cluster spacecraft detects the pulsation, as seen in the dynamic spectra of the radial magnetic field components b_r (Fig. 8.4). Consequently, as discussed in the previous case study the wave frequency is uniform with respect to magnetic L shells (see Sec. 7.5).

The pulsation event observed can be subdivided into two different wave packages with respect to its amplitude pattern. The first packet occurs between 07:50 and 07:56, where amplitudes up to 2 nT are observed in the b_r component and up to 1 nT in the b_ϕ component. The electric field oscillates mainly in the E_r component with amplitudes up to
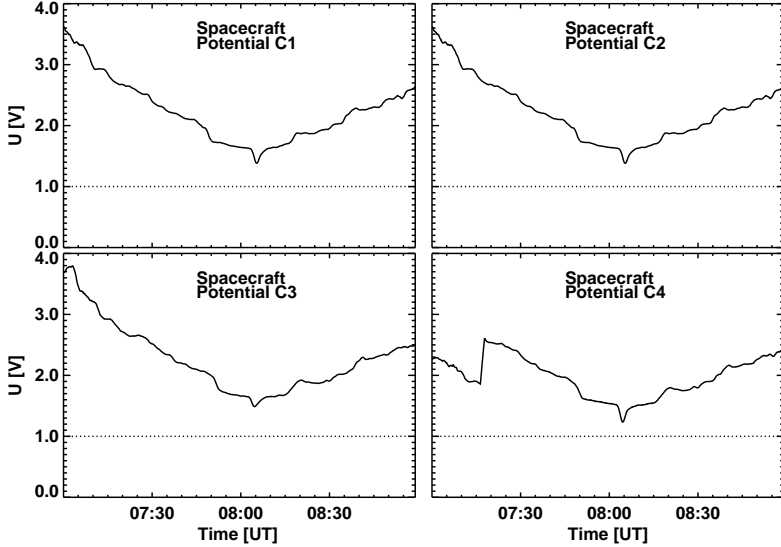
Figure 8.2: Spacecraft potential measured by Cluster spacecraft C1. Values of $U < 1$ V (dotted line) are expected inside the plasmasphere.

2 mV/m at C1 and lower amplitudes at the other spacecraft.

The onset of the pulsation occurs at different times and different locations with spacecraft C1 detecting the perturbation first followed by spacecraft C3, C2 and C4. Furthermore, the amplitude pattern of both, the magnetic and electric fields are clearly different at each spacecraft, where distinct signals are seen in the b_r and E_r components of C1 and C3, that is those spacecraft observing the pulsation first.

The second wave packet is seen between 08:04 and 08:16, where again amplitudes up to 2 nT are observed in b_r and up to 1 nT in b_ϕ. In contrast to the first wave packet the oscillations in the b_r components are regular at each spacecraft. The onsets of the wave are again different at the different spacecraft. But now the order has changed compared to the first packet. The pulsation event is first observed by C2 and C4 almost simultaneously followed by C1 and C3 observing the event about one minute later. The amplitude of the electric field is much smaller than in the first packet.

In order to proof the standing wave character of the detected pulsation, the Poynting vector S_p and the time-average energy flux $\langle S_p \rangle$ is determined using Eqs. 6.23 and 6.24, respectively. Here $\langle S_p \rangle$ is calculated by averaging over the wave period $T = 43$ s. We found $S_{p,r} \approx 0$ and $S_{p,\phi} \approx 0$ and oscillations in $S_{p,\parallel}$ (Fig. 8.5), but the field parallel component of the time integrated energy flux $\langle S_{p,\parallel} \rangle$ is non-zero for the first wave packet. $\langle S_{p,\parallel} \rangle$ can deviate from zero in case the oscillation is detected off from the null point of the field line (see Sec. 6.4). In order to proof this assumption the ionospheric conductivity is determined
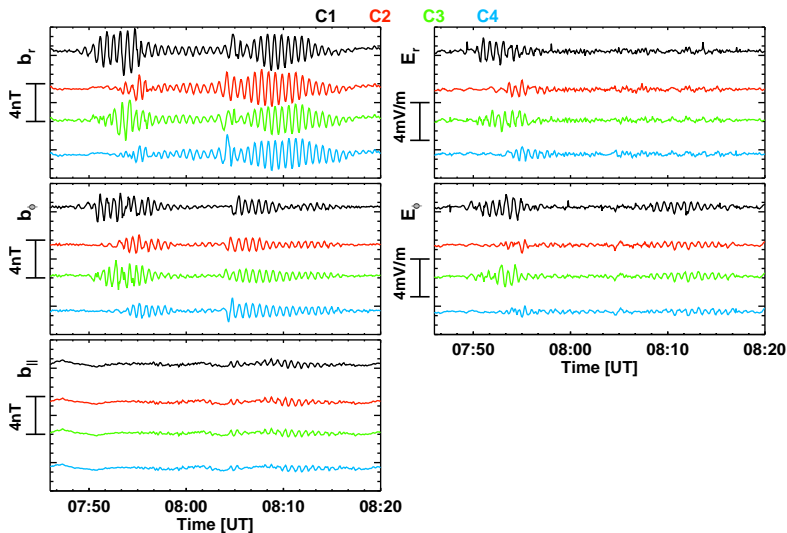
Figure 8.3: FGM and EFW measurements for the four Cluster spacecraft (C1: black, C2: red, C3, green, C4: blue), transformed into a Mean-Field-Aligned coordinate system.

at the northern and southern footprints of the field lines crossed by the four satellites. Due to the small Cluster configuration the geographic coordinates of all footprints are approximately at 50° N, 93° E at the northern and 70° S, 80° at the southern ionosphere. At 08:00 UT the northern ionospheric height integrated Pedersen conductivity is $\Sigma_{P,N} = 7.7$ S, and in the southern ionosphere it is $\Sigma_{P,S} = 5.9$, respectively. Similar to the first case study the small but significant non-zero component $\langle S_\parallel \rangle$ is supposed to be a consequence of the slightly different ionospheric conductivities (see Sec. 7.2). Accordingly, one can conclude that a standing field line oscillation is detected simultaneously by all four Cluster satellites. The first wave packet is detected south of the field line null point, whereas the second wave packet is located close to it, as here $\langle S_{p,\parallel} \rangle$ is almost zero.

8.3   Temporal evolution

The simultaneous measurements of the four Cluster satellites allows in principle the investigation of spatial and temporal structures of the detected ULF pulsation, but it requires a data representation in four dimensions. An approach to this representation is a field line related coordinate system, the LDM coordinate system, introduced in Sec. 6.3.2. During the time interval analyzed the spacecraft orbits vary in the M coordinate between $M = 13.72$ and $M = 13.84$ (Fig. 8.6), which implies that the Cluster satellites cover a spatial range of 0.05 R_E in azimuthal direction.
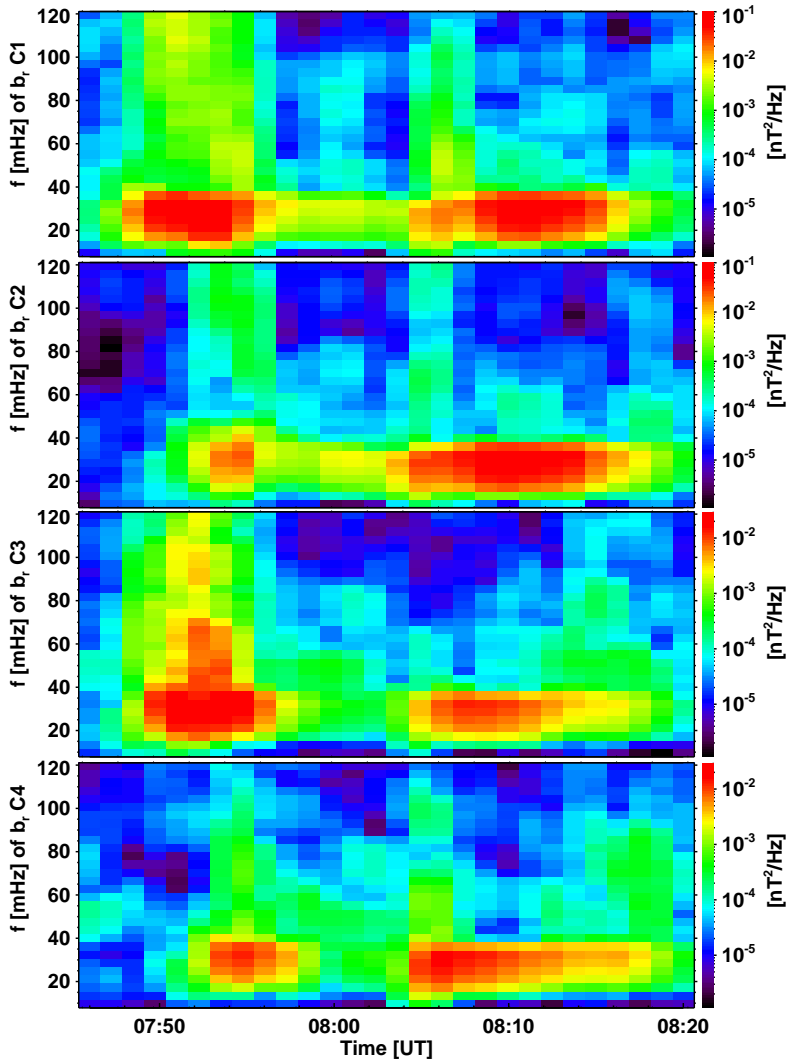
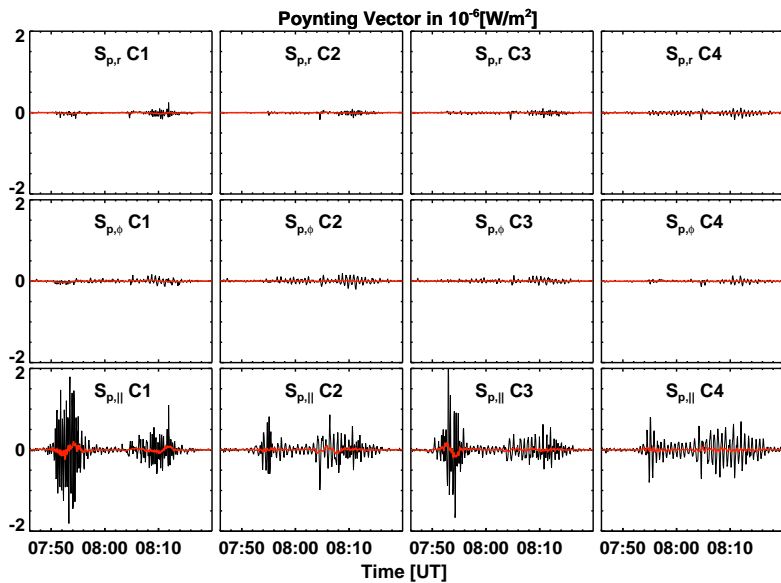Figure 8.4: Dynamic spectra of b_r components observed by the four Cluster satellites.

Figure 8.5: Components of the Poynting vector $\boldsymbol{S}_p$ observed by Cluster spacecraft. The red line represents the time-average energy flux $\langle \boldsymbol{S}_p \rangle$.
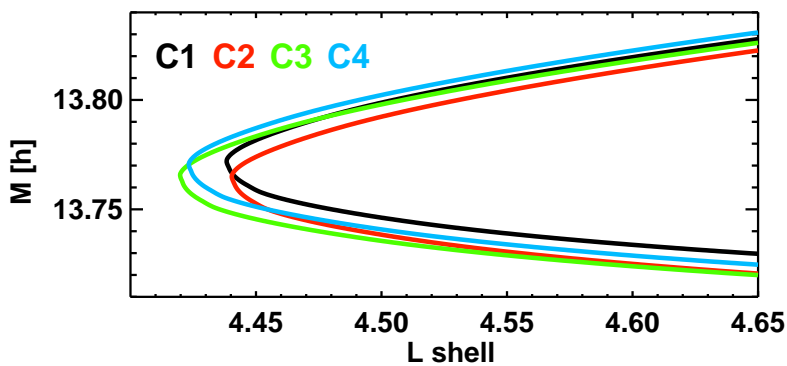

Figure 8.6: Magnetic local time of Cluster orbit plotted against the L coordinate.

The orbits of the four satellites are displayed in Fig. 8.7 transformed to the L-D coordinates, where the exact position of each spacecraft is marked at four specific times $t_1 = 07:54:02$, $t_2 = 07:55:06$, $t_3 = 08:04:10$ and $t_4 = 08:09:26$ UT. The satellites move from the southern magnetic hemisphere $D < 0$ R_E across the magnetic equator $D = 0$ R_E into the northern hemisphere $D > 0$ R_E. Between 07:46 and 08:20 UT all four Cluster spacecraft cross field lines with L values between 4.4 and 4.8. The color index of each orbit is related to the transverse amplitude $A = (A_r^2 + A_\phi^2)^{0.5}$ to identify regions of high wave activity. Here A_r and A_ϕ are the instantaneous amplitudes of the poloidal and toroidal magnetic field component, respectively, determined using the analytic signal or Carson-Gabor representation of the time series b_r and b_ϕ (see Sec. 6.5). Fig. 8.8 displays a more detailed description of the instantaneous transverse amplitude A.

The LD representation reveals, that the first maximum occurs when crossing field lines in the range $L = [4.50, 4.65]$ in the southern magnetosphere at $D \approx -0.6 R_E$, whereas the second maximum occurs crossing different field lines at $L = [4.42, 4.50]$ close to the field line vertex, i.e. close to the magnetic equator. The existence of an amplitude maximum in b_r together with the absence of any electric field oscillations near the magnetic equator suggest the existence of an even mode oscillation. This assumption is consistent with earlier studies, where dayside Pc4 pulsations have been interpreted as second harmonic wave modes (e.g. Singer et al. 1982, Takahashi and Anderson 1992).

Now we describe further details of the detected wave field by discussing the four selected times t_1, t_2, t_3 and t_4 marked in Figs. 8.7 and 8.8. At t_1 an amplitude maximum of around 2.6 nT is observed in spacecraft C1 and C3 simultaneously when both satellites are located nearly at the same L shell $L = 4.57$. At the same time spacecraft C2 and C4 are located about 0.05 R_E further out, where no clear amplitude maxima are visible. Accordingly, the radial extension of the first wave packet can be estimated at time t_1; we found a width of around $w = 0.1$ R_E.

At t_2 spacecraft C2 and C4 detects maxima with amplitudes of $A = 1.9$ nT (C2) and $A = 1.2$ nT (C4). These peaks are found at L shell $L = 4.59$, close to the field lines where C1 and C3 detect maxima. Consequently, the amplitude of the field line oscillation decreases between t_1 and t_2. Assuming that the amplitude of the signal decays exponentially in time, i.e. $A(t) \propto e^{-\gamma t}$, the decay constant γ can be determined from

$$\gamma = \frac{1}{\Delta t} \ln\left(\frac{A(t_1)}{A(t_2)}\right) \qquad (8.1)$$

with $\Delta t = 64$ s. Amplitude values are obtained from spacecraft C3 at t_1 and C2 at t_2, as both spacecraft have the same field parallel position $D = -0.58$ R_E at these times. Inserting $A(t_1) = 2.6$ nT and $A(t_2) = 1.8$ nT in Eq. 8.1 leads to a decay constant of $\gamma \approx 5$ mHz and a corresponding e-folding time $1/\gamma$ giving an approximation of the lifetime $\tau = 2/\gamma \approx 400$ s. The amplitude pattern observed by the four Cluster satellites at two different times indicates the existence of a transient standing field line oscillation at L shells $L = [4.5, 4.65]$.

The field line oscillation does not disappear after time t_2 despite the detected amplitude decay: While the satellites move to inner L shells and towards the magnetic equator spacecraft C2, C3 and C4 detect an amplitude peak simultaneously at t_3, whereas a peak is visible at C1 around 40 seconds later. Comparing with time series of b_r (Fig. 8.3) shows that these maxima mark the onset of the second wave packet detected at L shells
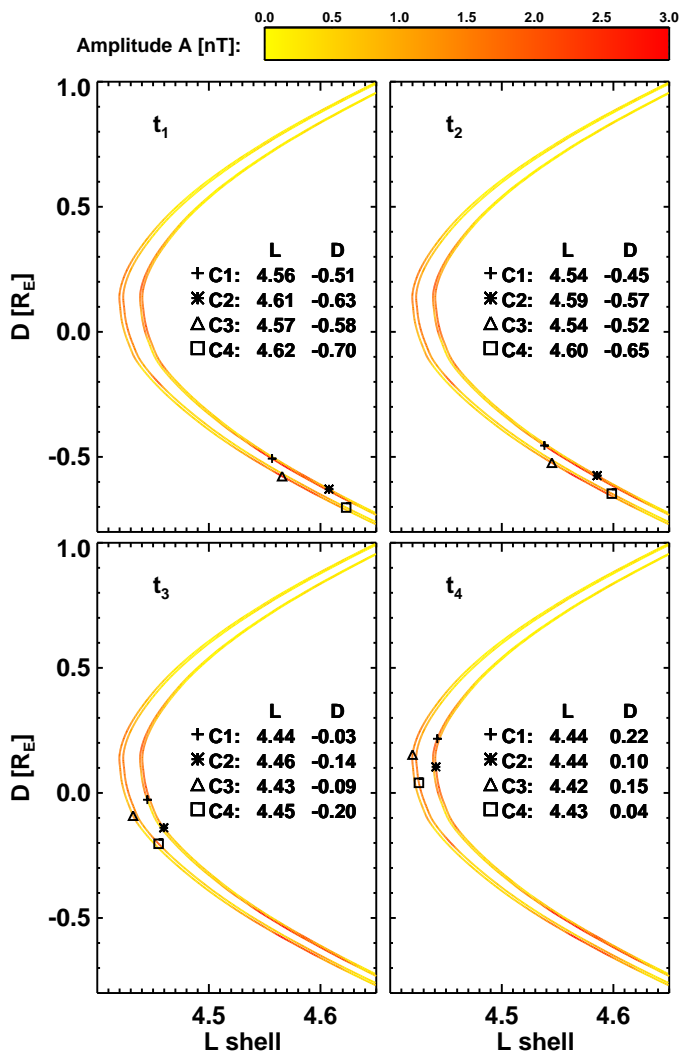
Figure 8.7: Cluster orbits in L-D coordinates at $t_1 - t_4$. The spacecraft move from negative to positive D values across the magnetic equator ($D = 0R_E$). The color index gives the instantaneous amplitude of the transverse magnetic field oscillation.
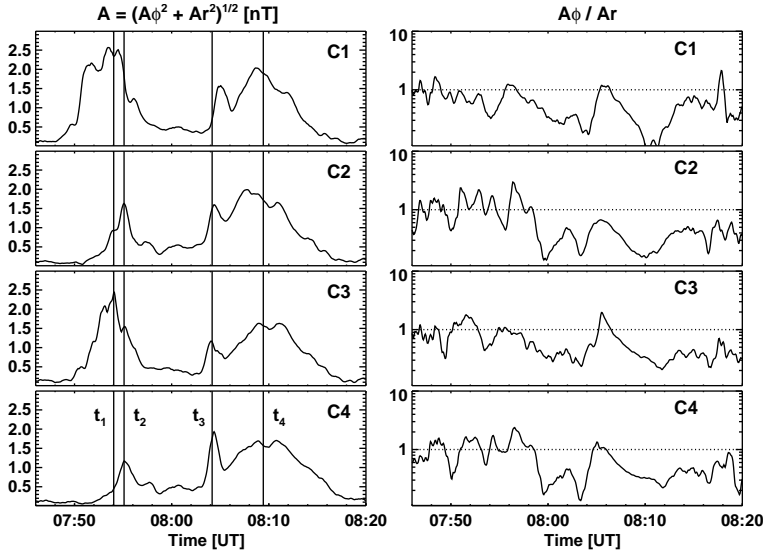
Figure 8.8: Instantaneous amplitude $A(t)$ of the transverse magnetic field oscillation (left) and ratio of poloidal and toroidal amplitudes (right) for time series of the four satellites.

$L = [4.42, 4.50]$. This wave packet is fully developed at time t_4 in all four spacecraft observations.

The observed temporal evolution of the wave amplitude justifies the assumption that both wave packets are excited successively. The first wave is detected at the end of its lifetime, whereas the second wave packet can be understood as another wave excited at the same magnetic field lines. As discussed in Chapter 4 the wave polarization of an ULF pulsation is expected to change from poloidal to toroidal during the temporal evolution of the wave field. Comparing the ratio of the toroidal amplitude A_ϕ and the poloidal amplitude A_r of both wave packets (Fig. 8.8) reveals that the first one is characterized by $A_\phi \approx A_r$, i.e. the toroidal part of the amplitude is comparable to the poloidal part. In contrast to that the second wave packet exhibits $A_\phi < A_r$, i.e. it is "less" toroidal than the first wave packet. Following the theory the observed pattern of the wave polarization indicates that the first wave packet is detected in a later phase of the temporal evolution than the second wave packet. Consequently, the double excitation of magnetic field lines within the same region is a possible scenario to describe the observed amplitude pattern and wave polarization.

8.4 Azimuthal wave number

The azimuthal wave number of the poloidal Alfvén wave under investigation is estimated using the method described in Sec. 7.4. Again high resolution magnetometer data (10 Hz)
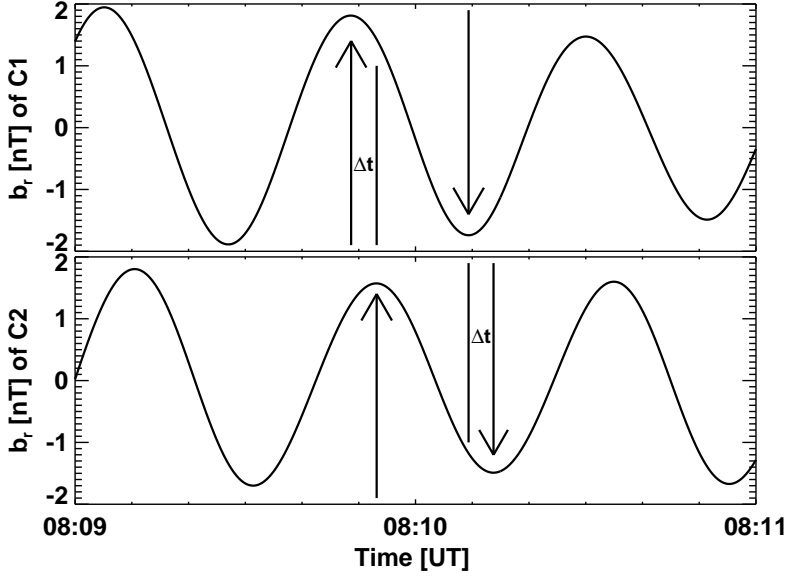
Figure 8.9: Time series of the radial magnetic field oscillation of spacecraft C1 and C2.

are used to estimate the phase difference $\Delta\Phi$ in the b_r component of two satellites observed between 08:09 and 08:11 UT, where the data are bandpassed filtered between 10 mHz and 50 mHz (Fig. 8.9). During this time interval spacecraft C1 and C2 are located on the same L shell, $L = 4.44$ (see Fig. 8.7). The angle in the azimuthal direction between the two satellites is $\Delta\Phi = 0.26° \pm 0.01°$. The time difference between extreme values of the signals is $\Delta t = 4.8 s$ which corresponds to a phase difference of $\Delta\Psi = 40°$ assuming a wave period of $T = 1/f_{obs} = 43$ s. Assuming an uncertainty in Δt of $\delta t = 0.2$ s due to the temporal resolution of the time series and in T of $\delta T = 1 s$ we have $m = 155 \pm 11$, which is in good agreement with the theoretically expected high-m values for poloidal ULF pulsations. The corresponding azimuthal wavelength is $\lambda = 2\pi/k_\phi \approx 1100$ km with $k_\phi = m/L$.

8.5   Radial Structure

A range-time-intensity (RTI) representation as known from ground-based ULF wave observations (e.g. Walker et al. 1979, McDiarmid and Allan 1990, Fenrich et al. 1995) is used to infer the radial structure and is displayed for the b_r component in Fig. 8.10. The actual perturbations of the magnetic field measured at the same time have been linearly interpolated between the four spacecraft positions. For the first wave packet, located at L shells between $L = 4.50$ and $L = 4.65$, the RTI plot reveals a clear spatial and temporal structure with perturbation maxima and minima moving across L-shells towards
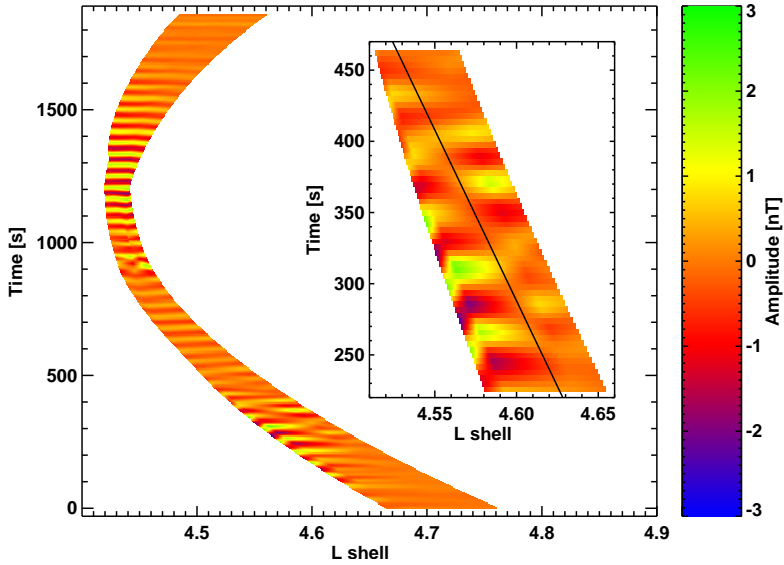
Figure 8.10: Range-time-intensity plot of the August 7, 2003, 07:49-08:16 UT magnetic field fluctuations of the b_r component. The ordinate is the time axis with T = 0 s corresponding to 07:49 UT. The black line in the inlet indicates the estimated location of the phase jump in L-direction.

the Earth. The structured change from positive to negative perturbations indicates a clear phase change in the L-direction. The black line in the inset of Fig. 8.10 traces the zero of magnetic field amplitude as the wave field goes through its temporal cycle within a spatial structure that exhibits a phase jump in the radial direction. Due to the time variation imposed on such a spatial structure the wave phase moves apparently towards smaller L shells (Wright et al. 1999b). This virtual earthward moving phase structure is reminiscent of poleward moving bands of irregularities observed in ionospheric data associated with field line resonance (Walker et al. 1979, Poulter et al. 1982).

In contrast to the first wave packet the second one found at $L = [4.42, 4.50]$ is composed of field lines oscillating exactly in phase (Fig. 8.10). Assuming that both wave packets originate from the oscillation of the same bundle of field lines and the phase jump is fixed between $L = 4.50$ and $L = 4.65$, the identification of a phase jump in the second wave packet is impossible. The Cluster satellites move parallel to the apparent position of the phase jump while detecting the second wave packet (see Fig. 8.7). This assumption is supported by the observation of the instantaneous amplitude A at time t_4: Spacecraft C1 and C2 located at $L = 4.45$ detects higher amplitude values, $A \approx 2.0$ nT, than C3 and C4 located at $L = 4.43$ detecting $A \approx 1.6$ nT (Fig. 8.8).

8.6   Modeling the spatio-temporal structure

For a more detailed understanding of the observed spatio-temporal structure we have modeled the ULF wave event using the following assumptions and observations:

(a) The pulsation is composed of two consecutively excited wave packets with lifetimes in the order of $\tau \approx 400$s.

(b) The pulsation is a second longitudinal harmonic standing field line oscillation.

(c) The azimuthal wave number of the wave field is $m = 155$.

(d) The wave phase changes by $180°$ in the range of L shells $L \in [4, 50, 4.65]$.

The spatio-temporal variation is described by the following expression:

$$b_{r,model} = b_0(t) \cdot S(D, t) \cdot B(\Psi) \cdot C(L), \qquad (8.2)$$

where the function $b_0(t)$ represents the time dependent amplitude, $S(D, t)$ the standing wave character, $B(\Psi)$ the azimuthal and $C(L)$ the radial structure of the wave field. In the following we discuss each of these functions whose parameter range is varied restricted by the assumptions given above in order to fit the actual observed data simultaneously in all four Cluster satellites. The main objective of this modeling efforts is a comparison of the modeled field line oscillation with the observed pulsation.

The time dependent amplitude $b_0(t)$ is given by two Gauss-functions generating the temporal development of the two wave packets:

$$b_0(t) = b_1 \exp\left(-\frac{(t - t_1)^2}{2\tau_1^2}\right) + b_2 \exp\left(-\frac{(t - t_2)^2}{2\tau_2^2}\right). \qquad (8.3)$$

The amplitude maxima in time are at $t_1 = 07{:}51$ UT and $t_2 = 08{:}10$ UT. For the first wave packet the maximum amplitude is $b_1 = 3.0$ nT and the width of the temporal amplitude distribution $\tau_1 = 200$ s. For the second wave packet we choose $b_2 = 4.0$ nT and $\tau_2 = 250$ s. The resulting temporal evolution of $b_0(t)$ is displayed in Fig. 8.11.

In order to demonstrate the need for assuming two separate wave packets and an decay of wave amplitude, Fig. 8.12 compares the time series of a modeled single wave packet with constant amplitude in time and the observed signals of the four satellites. The amplitude pattern of the first wave packet is well reproduced only in the spacecraft C1 and C3 observations. In C2 and C4 the observed wave amplitude is much smaller than the modeled amplitude. Furthermore, the observed second wave packet cannot be reproduced by the single wave model. A second amplitude maximum would be expected more than 10 minutes after the observed maximum when the satellites traverse the magnetic L shells where the first maximum is observed.

The standing wave along the magnetic field line is expressed by

$$S(D, t) = \exp\left(i\omega t + ik_{\parallel}D\right) + \exp\left(i\omega t - ik_{\parallel}D\right), \qquad (8.4)$$

where $k_{\parallel}$ denotes the field parallel wave number. The corresponding wavelength $\lambda_{\parallel} = 2\pi/k_{\parallel}$ depends on the length of the field line l and the harmonic number N of the oscillation:
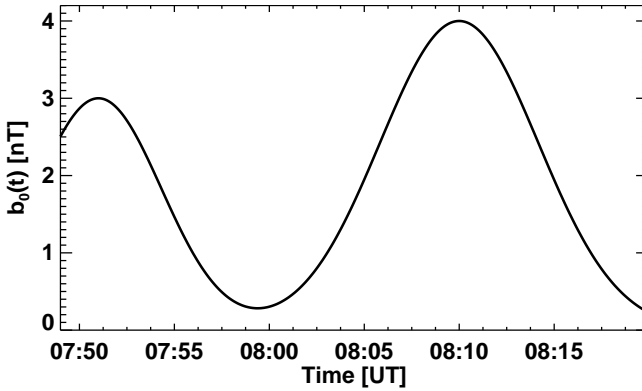
Figure 8.11: Temporal development of the wave amplitude $b_0(t)$.
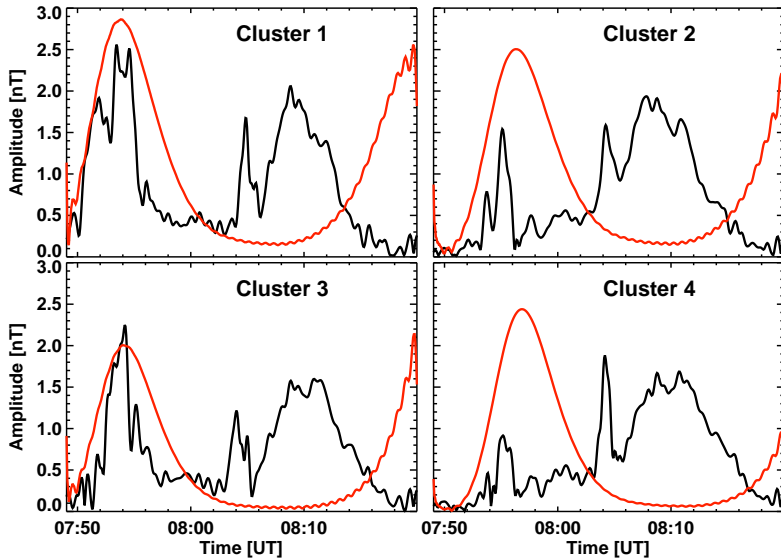
Figure 8.12: Instantaneous amplitudes of the radial magnetic field component b_r: observed signal (black) and modeled signal consiting of a single wave (red).
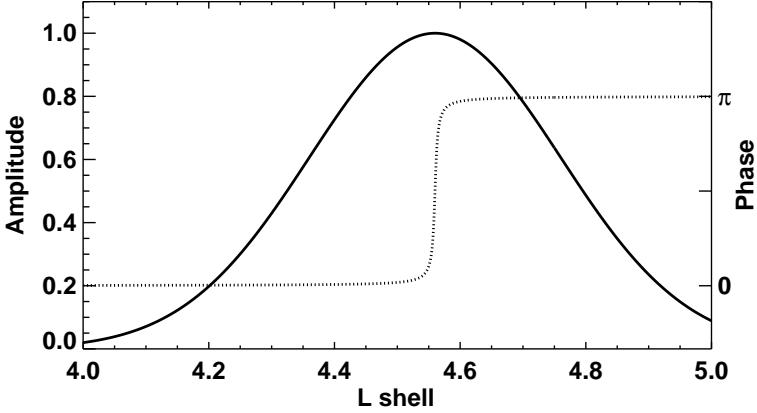
Figure 8.13: Radial profile of the wave amplitude (solid line) and phase shift (dotted line).

$\lambda_\parallel = 2l/N$. The length of the field line with the vertices $L_{pos} = 4.56$ is $l = 10.4$ R$_E$. Assuming a second harmonic oscillation, as discussed above, results in a wavelength of $\lambda_\parallel = 10.4$ R$_E$ and a field parallel wave number of $k_\parallel = 0.096$ R$_E^{-1}$.

The azimuthal variation of the wave field is given by

$$B(\Psi) = \exp(im\Psi), \tag{8.5}$$

where an azimuthal wave number of $m = 155$ is inserted which fits to the observed values of m. The corresponding azimuthal wavelength is $\lambda_\Psi = 2\pi/k_\Psi$ with $k_\Psi = m/L_{pos} = 34.0$ R$_E^{-1}$. Accordingly, the azimuthal spatial scale of the wave is $\lambda_\Psi = 0.18$ R$_E$.

The transverse structure of the wave field is described by a Gauss function and a phase function representing the amplitude variation and the change of the wave phase across the L shells, respectively:

$$C(L) = \exp\left(-\frac{(L - L_{pos})^2}{2\sigma^2}\right) \cdot \exp(i\Theta). \tag{8.6}$$

The parameter L_{pos} marks the position of maximum amplitude and phase jump. L_{pos} cannot be determined directly from the observations as the RTI plot indicates only the apparent motion of the phase jump, but not its actual position L_{pos}. This position can be determined comparing modeled and observed time series. The radial width of the wave field is represented by σ. The distribution of the phase is modeled by $\Theta = (\pi/2) + \arctan\left[w(L - L_{pos})\right]$, where w affects the width of the region within which the phase changes from 0° to 180°. With these assumptions and the free model parameter L_{pos}, σ and w we generated in trial-and-error manor a series of pulsation wave fields. We found the best agreement between the observed and the modeled b_r components by using $L_{pos} = 4.56$, $w = 300$ R$_E^{-1}$, $\sigma = 0.05$ R$_E$ for the first wave packet and $\sigma = 0.2$ R$_E$ for the second one.
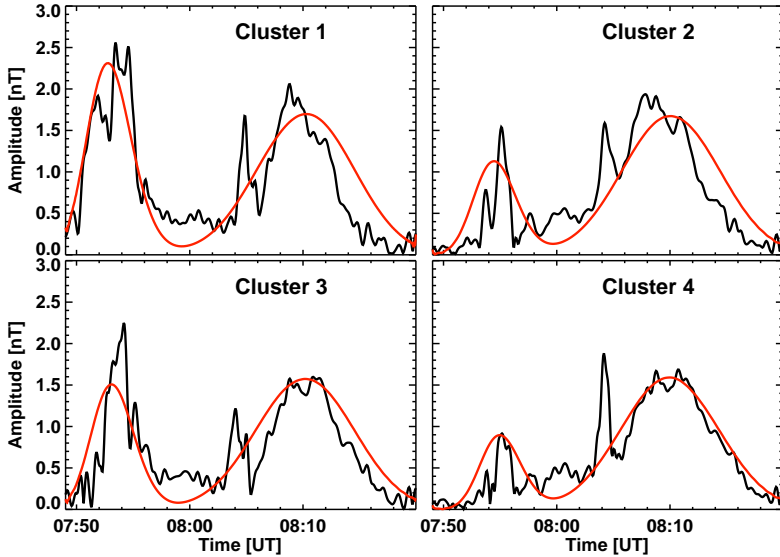
Figure 8.14: Instantaneous amplitudes of the radial magnetic field component b_r: observed signal (black) and modeled signal consisting of two waves but without phase jump (red).

At first the modeled signal is determined without the detected jump in wave phase, i.e. the second factor on the right hand side of Eq. 8.6 is ignored (Fig. 8.14). The correspondence is evident in main features of the observed amplitude modulation, such as time and magnitude of the amplitude maxima of both wave packets, although the observed maxima of the first wave packet (07:50 - 08:00 UT) in spacecraft C2 and C3 are clearly larger than in the artificial signal. Considering the complete model including the phase jump further improves the accordance of observation and model (Fig. 8.15), especially the amplitude pattern of the C2 and C3 observations.

Furthermore, the modeled signal is capable to explain some detailed structure in the first wave packet of the spacecraft C2, C3 and C4 observation, which is caused by crossing the phase jump at $L = 4.56$. However, some other details are not reproduced, e.g. the small-scale structure of the first wave packet seen by spacecraft C1 and in particular the narrow amplitude peaks at the beginning of the second wave packet visible in all four satellites. We speculate that the latter discrepancy between model and observation is a consequence of the assumed temporal amplitude modulation. Apparently, modeling $b_0(t)$ by Gauss-functions fails to satisfy the real temporal evolution of a field line oscillation at least at the beginning of its lifetime. Nevertheless, modeling resulted in a value $L_{pos} = 4.56$ for the position of the excited field line.
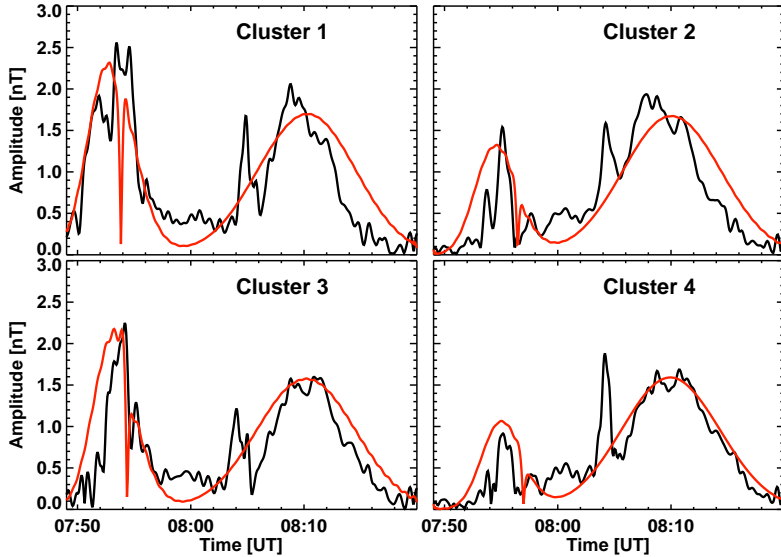
Figure 8.15: Instantaneous amplitudes of the radial magnetic field component b_r: observed signal (black) and modeled signal (red).

8.7   Poloidal Alfvén resonator

The excited field line bundle is located in the outer edge of the plasmapause as inspection of measurements of the spacecraft potential shows (Fig. 8.2). This outer region is suitable for the existence of an Alfvén resonator that confines the wave field by two poloidal turning points L_P (see Sec. 3). On account of this we compare the assumed radial amplitude distribution and the observed frequency $f_{obs} = 23$ mHz of the pulsation with the radial profile of the theoretically expected field line eigenfrequencies Ω_P and Ω_T (Fig. 8.18).

These eigenfrequencies are determined by applying the numerical method introduced in Sec. 6.1. For this purpose necessary plasma background parameters, e.g. distribution of magnetic field, current density and plasma density, are determined as introduced in Sec. 6.2. The radial and field aligned profiles of the magnetic field are calculated by the Tsy96 model (Tsyganenko and Stern 1996) for the input parameters $p_{dyn} = 2.60$ nPa, $D_{st} = -7$ nT, $b_y^{sw} = 6.0$ nT and $b_z^{sw} = 5.0$ nT. The radial plasma pressure profile $P(L)$ is calculated using Eq. 6.12 with $L_0 = 2.6$ R_E and $W = 2.04$ R_E. The maximum plasma pressure $P_0 = P(L_0)$ is selected so that at L_0 the plasma β is 0.019. For this set of parameters the current density $J_\perp(L)$ determined by Eq. 6.13 coincides with the current density obtained from the Tsy96 model (Eq. 6.11). The resulting radial profiles of β, P and $J_\perp$ are displayed in Fig. 8.16 corresponding to expected profiles during low geomagnetic activity (e.g. Lui and Hamilton 1992, Klimushkin et al. 2004).
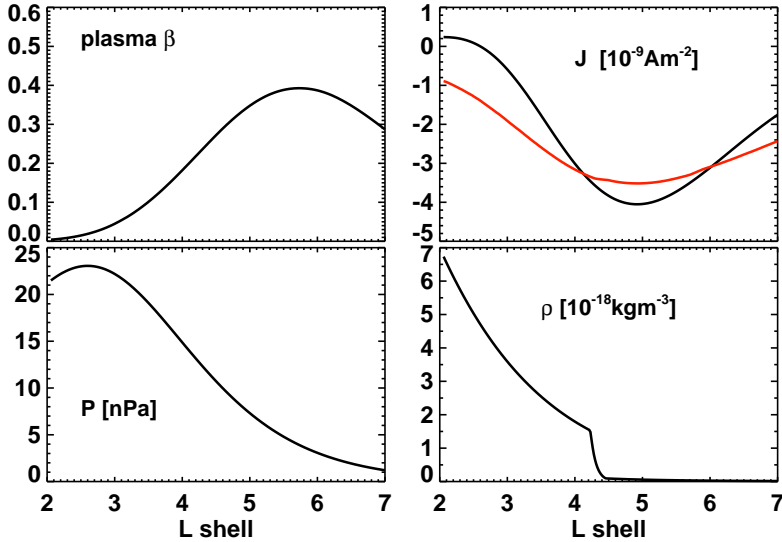
Figure 8.16: Assumed plasma background conditions. The plasma density is calculated from modeling the electron density. Profiles of plasma pressure P, β and current density J are determined by comparing the current density given by Eq. 6.14 with the current density obtained from the Tsy96 model (red line). Negative values of J correspond to a current directed westward.

The number density in the equatorial plane n_{eq} can be obtained from the model of Carpenter and Anderson (1992) (see Sec. 6.2.3). The distribution of the plasma density along field lines is assumed to follow the power law $\rho(s) = \rho_{eq}(LR_E/r)^\alpha$, where $\alpha = 2$ is typical for the vicinity of the plasmapause (e.g. Goldstein et al. 2001). From the modeled electron density distribution n_{eq} (Carpenter and Anderson 1992) we receive the plasma mass density $\rho_{eq} = n_{eq}m_{corr}m_p$, where m_p is the proton mass. Using a mass correction factor of $m_{corr} = 2$ considers that the plasma near the plasmapause is composed of protons and a significant part of heavier ions such as He^+, O^+ and O^{2+} (e.g. Takahashi et al. 2004).

The resulting radial profiles of poloidal and toroidal eigenfrequencies displayed in Fig. 8.17 are calculated for harmonic numbers $N = 1, \ldots, 4$. The poloidal eigenfrequency is slightly larger than the toroidal one, which is a necessary condition for the existence of the Alfvén resonator (e.g. Leonovich and Mazur 1995, Klimushkin et al. 2004). Observations and model of the wave field provide that the pulsation under investigation is a even harmonic wave. As evident from Fig. 8.17 the observed wave frequency $f_{obs} = 23$ mHz apparently belongs to a second harmonic oscillation which is radially trapped in an Alfvén resonator at the maximum of field line eigenfrequencies. However, similar to the first case study (Chapter 7) f_{obs} is not found between f_P and f_P as required by the theory.

In Fig. 8.18 the radial variations of eigenfrequencies Ω_P and Ω_T are compared with
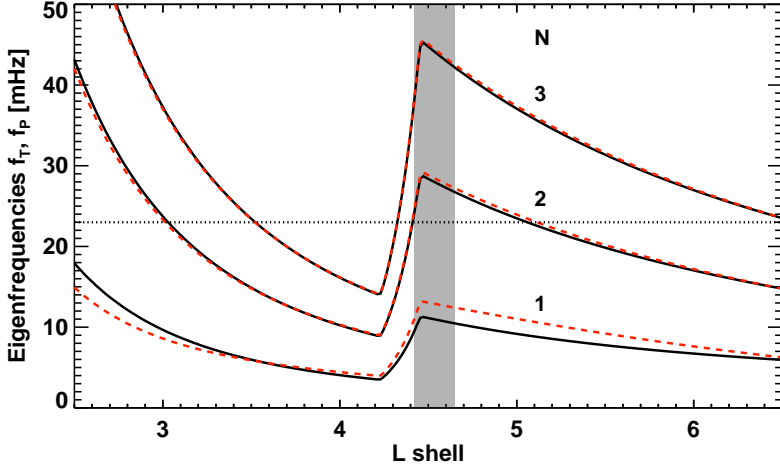
Figure 8.17: Profiles of the toroidal eigenfrequencies f_T (solid line) and poloidal eigenfrequencies (dashed line) f_T calculated for harmonic numbers $N = 1, \ldots, 4$ and a mass correction factor $m_{corr} = 2$. The dotted line marks the observed frequency $f_{obs} = 23$ mHz and the grey shaded background indicates L-shells where Cluster detects ULF wave activity.

the modeled amplitude profile of the wave mode at time t_4 of its maximum extension. The poloidal turning points defined by $f_{obs} = f_P$ are identified at field lines $L = 4.4$ and $L = 5.0$ leading to a total width of the poloidal wave resonator of 0.6 R_E. The modeled radial extend of the wave activity region is of the same size. The shift of the maximum of the amplitude distribution against the extremum of the eigenfrequency distribution is due to the asymmetry of the latter. We conclude that the wave field is confined in a poloidal Alfvén resonator at the outer edge of the dayside plasmapause.

The observed phase jump can be easily explained taking into account the radial localization and the rapid azimuthal variation $b_r \propto \exp(im\Psi)$. This results in a radially localized polarization current causing a magnetic field perturbation sheared in radial direction (Klimushkin et al. 2004). However, two other processes are capable to explain the existence of a phase jump in magnetic field line oscillations: Field line resonance and phase mixing. The classical process of field line resonance causes the onset of purely toroidal polarized Alfvén waves and, accordingly, can be excluded as origin of the phase jump, as the observed wave is mainly poloidally polarized. Phase mixing of adjacent field lines is as well inappropriate to explain the phase jump, because the wave packet is localized near the maximum of field line eigenfrequencies $\Omega_P(L)$, where the gradient $d\Omega_P/dL$ is small.

In order to examine under which conditions a theoretical correct Alfvén resonator can be established, the plasma background parameters are varied for the second harmonic frequencies. For this purpose the plasma mass density ρ has to be increased causing smaller
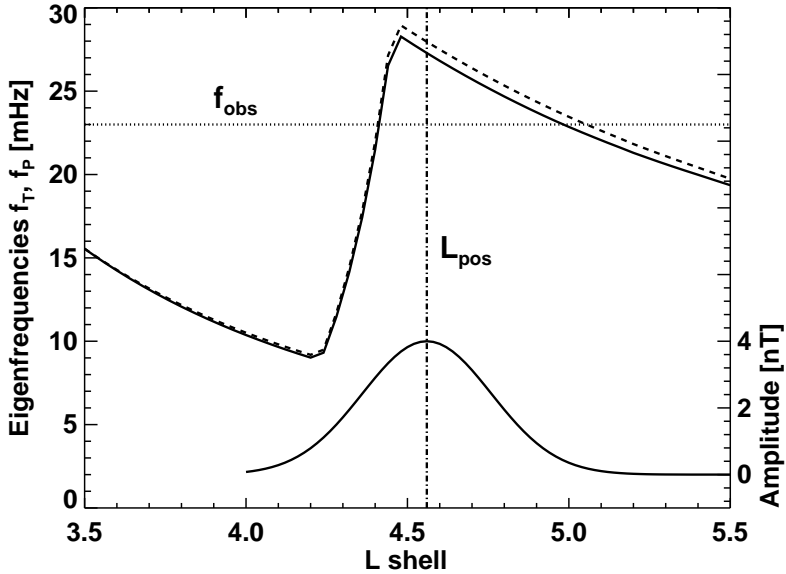
Figure 8.18: Radial profiles of wave amplitude at time t_4 and toroidal (solid line) and poloidal (dashed line) field line eigenfrequencies, each for the second longitudinal harmonic. The dotted line marks the observed frequency $f_{obs} = 23$ mHz, the dot-dashed line marks the L shell of maximum amplitude and phase jump $L_{pos} = 4.56$.

Alfvén velocity $V_A(L, \theta)$ and smaller eigenfrequencies. By changing the mass correction factor to $m_{corr} = 4.5$ the condition $f_{obs} > f_T$ is achieved. Additionally, the plasma β must be higher than before leading to an increase of the poloidal eigenfrequency and thus $f_P > f_{obs}$. Fig. 8.19 shows possible plasma background parameters, which are necessary for satisfying the requirement $f_P > f_{obs} > f_T$. Apparently, these conditions are not realistic for the terrestrial magnetosphere. A plasma pressure leading to $\beta \approx 1$ would be assumed at L-shells of interest as well as a high concentration of oxygen ions that would justify the high plasma density. Both is not expected to appear near the plasmapause, in particular during the assumed quiet level of geomagnetic activity.

8.8   Summary

The pulsation analyzed was detected by the four Cluster satellites in the time interval August 7, 2003 between 07:46 and 08:20 UT and has been localized close to the magnetic equatorial plane at field lines between $L = 4.42$ and $L = 4.70$. Comparing the plasmapause position, obtained from a dynamical simulation of the electron density, with the spacecraft orbit exhibited that the pulsation was excited at the outer edge of the boundary between
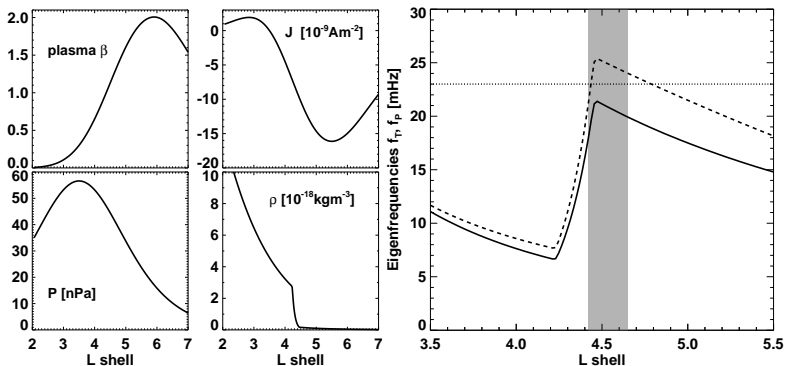
Figure 8.19: Plasma background parameters (left) and second harmonic eigenfrequencies (right). The grey shaded background indicates L-shells where Cluster detects ULF wave activity.

plasmasphere and magnetosphere. The spatial separation of the spacecraft has given us the possibility to determine the phase differences between signals of pairs of satellites in order to estimate the azimuthal wave number m of the pulsation. We have found $m \approx 155$ and consequently, a poloidal Alfvén wave with $m \gg 1$ has been observed.

A two wave packet structure of the pulsation has been detected in the instantaneous amplitude of the magnetic field oscillation featuring differences between both parts in terms of the wave polarization. In the first wave packet poloidal and toroidal magnetic field component have almost the same amplitude, whereas the second wave packet is purely poloidal for the most part. At first view this observation seems to be inconsistent with the theoretically expected evolution of a standing Alfvén wave which predicts a change in wave polarization from poloidal to toroidal (e.g. Mann and Wright 1995, Mager and Klimushkin 2006). However, displaying the instantaneous amplitude of the magnetic field oscillation in the LD coordinate system has elucidated a decrease of the wave amplitude in time at the same field lines for the first wave packet. Consequently, we have concluded that the first wave packet has been detected in a late stage of its temporal evolution when the amplitude of the toroidal component becomes comparable to the poloidal one. Wave damping due to dissipation at the ionosphere prevents the wave field from being observed in the status of purely toroidal polarization. The second wave packet has to be interpreted as a new excitation of a standing wave at the same field lines.

Modeling spacecraft observations crossing a double excited standing field line oscillation has confirmed and improved the knowledge about the above discussed spatial and temporal features of the detected wave field. It was shown that the wave is localized in radial direction with maximum of amplitude and phase jump located at $L = 4.56$. The spatial extend of the wave field is around 0.6 R_E. Location and size of the wave field was compared with the radial profile of theoretically expected toroidal and poloidal field line eigenfrequencies. We have suggested that the wave field is radially confined at the outer edge of the plasmapause between two L shells defined by $f_{obs} = f_P$ acting as wave turning

points. For that reason this specific region is believed to exhibit suitable conditions for the excitation of poloidal Alfvén waves (e.g. Klimushkin 1998a).

The radial magnetic field oscillation observed by the four Cluster satellites has been combined to a RTI representation (Fig. 8.10) which has clearly exposed a change in the wave phase by 180° in the radial direction. This phase jump is interpreted as a result of the localization of the wave field at the maximum of the radial amplitude distribution (Klimushkin et al. 2004).

9   General conclusions and outlook

The main aim of the present thesis has been formulated to compare the theoretically predicted spatio-temporal structure of poloidal standing field line oscillations excited in an Alfvén wave resonator region with multi-point measurements of ULF pulsations made by the Cluster satellites. In two case studies Alfvén wave activity has been detected near the terrestrial plasmapause, which is a favored region for the existence of the Alfvén resonator due to the strong gradients in Alfvén velocity and field line eigenfrequencies. The field aligned and azimuthal structure of these wave fields has been successfully identified as second and third harmonic standing field line oscillations, respectively, each with azimuthal wave numbers $m \gg 1$, which are well known characteristics of poloidal Alfvén waves. Investigating the radial structure and the temporal evolution in particular has benefited from the constellation of the four Cluster satellites and the polar orbit with perigee near the dayside plasmapause. These configurations have allowed the execution of newly developed representations of the magnetic field data, such as the field line related LDM coordinate system and the Range-Time-Intensity plot.

The LDM representation of wave activity has been successfully applied for different spacecraft constellations, both for the large spacecraft separation in Chapter 7 and for the small scaled Cluster tetrahedron in Chapter 8. The primary outcome of this analysis technique is that the detected radial structure of both wave fields exhibits theoretically expected Gaussian or more complex radial amplitude distribution, whose localization and radial extend fits precisely to the size of the Alfvén resonator regions bounded by two poloidal turning points $f_{wave} = f_P$. The resonator has been determined by comparing the observed frequency with theoretically expected poloidal and toroidal eigenfrequencies for realistic plasma background conditions. The RTI data representation produces reliable results only when the spacecraft separation is not too large. Consequently, the small- scale spacecraft configuration of the event detected outside the plasmasphere provides an insight into the temporal evolution of the wave field and enables the identification of a 180° jump of the wave phase across magnetic L-shells. The application of such investigations are inappropriate for the pulsation detected inside the plasmasphere due to the prevalent large distances between the satellites of more than 2 R_E.

Both studies have shown that spatial and temporal properties of the analyzed wave fields are in good agreement with main features predicted by the theoretical framework of Leonovich and Mazur (1990, 1993, 1995), Klimushkin et al. (2004) and Mager and Klimushkin (2006). However, some details of this framework concerning high-m waves are not reported until now, neither in ground based data nor in space. Although, for example, the radial extension of the observed wave fields coincide with the theoretical predicted wave turning points, the determined difference between poloidal and toroidal eigenfrequencies is in fact too small for the generation of resonator eigenfrequencies. It

has been found that a sufficient difference $\Omega_P - \Omega_T$ can be achieved for second or third harmonic oscillations only if the values of plasma density and plasma β are higher than one would expect in the inner magnetosphere. Consequently, the theoretical framework has to be improved in order to explain the existence of poloidal Alfvén resonators when $\Omega_P \approx \Omega_T$.

Furthermore, the suggested temporal change in wave polarization has not been detected neither in the pulsations analyzed in this work nor in other observations of magnetospheric ULF waves. In this case one would also expect the existence of a toroidal wave with a large azimuthal wave number, as m remains constant during the transformation of wave polarization. The reason for these lacking observations is probably the rapid damping of the poloidal oscillation due to ionospheric damping, which implies that the transformation from poloidal to toroidal is incomplete (e.g. Klimushkin and Mager 2004).

Consequently, further investigations on ULF wave activity near the plasmapause are necessary to improve our knowledge on the spatio-temporal structure of magnetospheric Alfvén waves. The detection of a field line oscillation transforming its polarization and the corresponding high-m toroidal wave would be an impressive verification of the theoretical framework. The present thesis could be used as a guide for future analysis of magnetospheric ULF wave activity with multi-spacecraft missions. It specifies essential theoretical background information on the characteristics of poloidal and toroidal field line oscillations and their spatial and temporal structure. The introduced analysis methods, developed for both small and large spacecraft separations, are capable to distinguish between spatial and temporal effects that cause the modulation in the observed wave amplitude. In general a small spacecraft tetrahedron seems to provide better possibilities of a detailed wave field analysis. In addition, the Cluster mission is an appropriate tool for the development of a statistical survey of properties of Alfvénic waves in the terrestrial magnetosphere, as it delivers an extensive amount of magnetic and electric field data over a time range of more than eight years and covering different regions of the Earth's magnetosphere.

Bibliography

Allan, W. and Poulter, E. M.: ULF waves-their relationship to the structure of the Earth's magnetosphere, Reports of Progress in Physics, 55, 533–598, 1992.

Allan, W., Poulter, E. M., and Nielsen, E.: STARE observations of a Pc 5 pulsation with large azimuthal wave number, J. Geophys. Res., 87, 6163–6172, 1982.

Allan, W., Poulter, E. M., Glassmeier, K. H., and Nielsen, E.: Ground magnetometer detection of a large m Pc5 pulsation observed with the STARE radar, J. Geophys. Res., 88, 183–188, 1983.

Allan, W., Poulter, E. M., and White, S. P.: Hydromagnetic wave coupling in the magnetosphere-Plasmapause effects on impulse-excited resonances, Planet. Space Sci., 34, 1189–1200, doi:10.1016/0032-0633(86)90056-5, 1986.

Anderson, B. J., Engebretson, M. J., Rounds, S. P., Zanetti, L. J., and Potemra, T. A.: A statistical study of Pc 3-5 pulsations observed by the AMPTE/CCE magnetic fields experiment. I - Occurrence distributions, J. Geophys. Res., 95, 10 495–10 523, 1990.

Angerami, J. J. and Carpenter, D. L.: Whistler Studies of the Plasmapause in the Magnetosphere, 2, Electron Density and Total Tube Electron Content near the Knee in Magnetospheric Ionization, J. Geophys. Res., 71, 711, 1966.

Arfken, G. B. and Weber, J. W.: Mathematical methods for physicists, San Diego, Calif.: Acad. Press, 1995.

Baker, D. N., Blake, J. B., Callis, L. B., Cummings, J. R., Hovestadt, D., Kanekal, S., Klecker, B., Mewaldt, R. A., and Zwickl, R. D.: Relativistic electron acceleration and decay time scales in the inner and outer radiation belts: SAMPEX, Geophys. Res. Lett., 21, 409–412, 1994.

Balogh, A., Carr, C. M., Acuna, M. H., and Dunlop, M. W.: The Cluster magnetic field investigation: overwiew of in-flight perfomance and initial results, Ann. Geophysicae, 19, 1207–1217, 2001.

Baumjohann, W.: Plasmaphysik im Sonnensystem, chap. Die Erdmagnetosphäre, B.I. Wissenschaftsverlag, 1991.

Baumjohann, W. and Treumann, R. A.: Basic Space Plasma Physics, Imperial Coll. Press, London, 1996.

Berube, D., Moldwin, M. B., Fung, S. F., and Green, J. L.: A plasmaspheric mass density model and constraints on its heavy ion concentration, J. Geophys. Res., 110, A04 212, 1–5, doi:10.1029/2004JA010684, 2005.

Bilitza, D.: Empirical modeling of ion composition in the middle and topside ionosphere, Advances in Space Research, 10, 47–56, 1990.

Bilitza, D. and Reinisch, B. W.: International Reference Ionosphere 2007: Improvements and new parameters, Advances in Space Research, 42, 599–609, doi:10.1016/j.asr.2007. 07.048, 2008.

Bronstein, I. N., Semendjajew, K. A., and Grosche, G.: Teubner Taschenbuch der Mathematik, chap. 0.10 Tabellen zu den Integraltransformationen, Teubner, 1996.

Carpenter, D. L.: Electron-Density Variations in the Magnetosphere Deduced from Whistler Data, J. Geophys. Res., 67, 3345–3360, 1962.

Carpenter, D. L.: Whistler Evidence of a 'Knee' in the Magnetospheric Ionization Density Profile, J. Geophys. Res., 68, 1675–1682, 1963.

Carpenter, D. L. and Anderson, R. R.: An ISEE/Whistler model of equatorial electron density in the magnetosphere, J. Geophys. Res., 97, 1097–1108, 1992.

Carson, J. R. and Fry, T. C.: Variable electric circuit theory with applications to the theory of frequency-modulation, Bell System Technical Journal, 16, 513–540, 1937.

Chapman, S. and Ferraro, V. C. A.: a New Theory of Magnetic Storms, J. Geophys. Res., 36, 77–97, 171–186, doi:10.1029/TE036i002p00077, 1931.

Chapman, S. and Ferraro, V. C. A.: a New Theory of Magnetic Storms, J. Geophys. Res., 37, 147–156, 421–429, doi:10.1029/TE037i002p00147, 1932.

Chapman, S. and Ferraro, V. C. A.: a New Theory of Magnetic Storms, J. Geophys. Res., 38, 79–96, doi:10.1029/TE038i002p00079, 1933.

Chen, L. and Cowley, S. C.: On field line resonances of hydromagnetic Alfven waves in dipole magnetic field, Geophys. Res. Lett., 16, 895–897, 1989.

Chen, L. and Hasegawa, A.: Kinetic theory of geomagnetic pulsations. I - Internal excitations by energetic particles, J. Geophys. Res., 96, 1503–1512, 1991a.

Chen, L. and Hasegawa, A.: Kinetic theory of geomagnetic pulsations. I - Internal excitations by energetic particles, J. Geophys. Res., 96, 1503–1512, 1991b.

Cheng, C. Z.: Magnetospheric equilibrium with anisotropic pressure, J. Geophys. Res., 97, 1497–1510, 1992.

Cheng, C. Z. and Qian, Q.: Theory of ballooning-mirror instabilities for anisotropic pressure plasmas in the magnetosphere, J. Geophys. Res., 99, 11 193–11 210, doi: 10.1029/94JA00657, 1994.

Chi, P. J. and Russell, C. T.: Phase skipping and Poynting flux of continuous pulsations, J. Geophys. Res., 103, 29 479–29 492, 1998.

Clilverd, M. A., Smith, A. J., and Thomson, N. R.: The annual variation in quiet time plasmaspheric electron density, determined from whistler mode group delays, Planet. Space Sci., 39, 1059–1067, doi:10.1016/0032-0633(91)90113-O, 1991.

Clilverd, M. A., Meredith, N. P., Horne, R. B., Glauert, S. A., Anderson, R. R., Thomson, N. R., Menk, F. W., and Sandel, B. R.: Longitudinal and seasonal variations in plasmaspheric electron density: Implications for electron precipitation, J. Geophys. Res., 112, A11 210, 1–10, doi:10.1029/2007JA012416, 2007.

Connerney, J. E. P., Acuna, M. H., and Ness, N. F.: Modeling the Jovian current sheet and inner magnetosphere, J. Geophys. Res., 86, 8370–8384, 1981.

Cramm, R., Glassmeier, K. H., Othmer, C., Fornacon, K. H., Auster, H. U., Baumjohann, W., and Georgescu, E.: A case study of a radially polarized Pc4 event observed by the Equator-S satellite, Ann. Geophysicae, 18, 411–415, 2000.

Cummings, W. D., O'Sullivan, R. J., and Coleman, P. J.: Standing Alfvén Waves in the Magnetosphere, J. Geophys. Res., 74, 778, 1969.

Daglis, I. A., Thorne, R. M., Baumjohann, W., and Orsini, S.: The terrestrial ring current: Origin, formation, and decay, Reviews of Geophysics, 37, 407–438, doi:10.1029/1999RG900009, 1999.

De Michelis, P., Daglis, I. A., and Consolini, G.: Average terrestrial ring current derived from AMPTE/CCE-CHEM measurements, J. Geophys. Res., 102, 14 103–14 112, doi:10.1029/96JA03743, 1997.

Décréau, P. M. E., Fergeau, P., Krasnoselskikh, V., Le Guirriec, E., Lévêque, M., Martin, P., Randriamboarison, O., Rauch, J. L., Sené, F. X., Séran, H. C., Trotignon, J. G., Canu, P., Cornilleau, N., de Féraudy, H., Alleyne, H., Yearby, K., Mögensen, P. B., Gustafsson, G., André, M., Gurnett, D. C., Darrouzet, F., Lemaire, J., Harvey, C. C., Travnicek, P., and Whisper Experimenters group: Early results from the Whisper instrument on Cluster: an overview, Ann. Geophysicae, 19, 1241–1258, 2001.

Denton, R. E. and Vetoulis, G.: Global poloidal mode, J. Geophys. Res., 103, 6729–6740, doi:10.1029/97JA03594, 1998.

Denton, R. E., Lessard, M. R., Anderson, R., Miftakhova, E. G., and Hughes, J. W.: Determining the mass density along magnetic field lines from toroidal eigenfrequencies: Polynomial expansion applied to CRRES data, J. Geophys. Res., 106, 29 915–29 924, doi:10.1029/2001JA000204, 2001.

Denton, R. E., Lessard, M. R., and Kistler, L. M.: Radial localization of magnetospheric guided poloidal Pc 4-5 waves, J. Geophys. Res., 108, SMP 4, 1–10, doi:10.1029/2002JA009679, 2003.

Denton, R. E., Menietti, J. D., Goldstein, J., Young, S. L., and Anderson, R. R.: Electron density in the magnetosphere, J. Geophys. Res., 109, A09 215, 1–14, doi:10.1029/2003JA010245, 2004.

Dungey, J. W.: Interplanetary Magnetic Field and the Auroral Zones, Physical Review Letters, 6, 47–48, doi:10.1103/PhysRevLett.6.47, 1961.

Dungey, J. W.: Hydromagnetic Waves, in: Physics of Geomagnetic Phenomena, edited by Matsushita, S. and Campbell, W. H., pp. 913–934, 1967.

Dunlop, M. W., Balogh, A., Southwood, D. J., Elphic, R. C., Glassmeier, K.-H., and Neubauer, F. M.: Configurational sensitivity of multipoint magnetic field measurements, Tech. rep., 1990.

Engebretson, M., Glassmeier, K.-H., Stellmacher, M., Hughes, W. J., and Lühr, H.: The dependence of high-latitude Pc5 wave power on solar wind velocity and on the phase of high-speed solar wind streams, J. Geophys. Res., 103, 26 271–26 384, 1998.

Engebretson, M. J. and Cahill, L. J.: Pc5 pulsations observed during the June 1972 geomagnetic storm, J. Geophys. Res., 86, 5619–5631, doi:10.1029/0JGREA0000860000A7005619000001, 1981.

Engebretson, M. J., Zanetti, L. J., Potemra, T. A., and Acuna, M. H.: Harmonically structured ULF pulsations observed by the AMPTE CCE magnetic field experiment, Geophys. Res. Lett., 13, 905–908, 1986.

Engebretson, M. J., Zanetti, L. J., Potemra, T. A., Klumpar, D. M., Strangeway, R. J., and Acuna, M. H.: Observations of intense ULF pulsation activity near the geomagnetic equator during quiet times, J. Geophys. Res., 93, 12 795–12 816, 1988.

Eriksson, A. I.: Analysis Methods for Multi-Spacecraft Data, chap. Spectral Analysis, pp. 10 – 14, International Space Science Institut (ISSI), 1998.

Eriksson, A. I., André, M., Klecker, B., Laakso, H., Lindqvist, P.-A., Mozer, F., Paschmann, G., Pedersen, A., Quinn, J., Torbert, R., Torkar, K., and Vaith, H.: Electric field measurements on Cluster: comparing the double-probe and electron drift techniques, Ann. Geophysicae, 24, 275–289, 2006.

Eriksson, P. T. I., Blomberg, L. G., and Glassmeier, K.-H.: Cluster satellite observations of mHz pulsations in the dayside magnetosphere, Adv. Space Res., 23, 2679–2685, doi:10.1016/j.asr.2005.04.103, 2005a.

Eriksson, P. T. I., Blomberg, L. G., Walker, A. D. M., and Glassmeier, K.-H.: Poloidal ULF oscillations in the dayside magnetosphere: a Cluster study, Ann. Geophysicae, 23, 2679–2685, 2005b.

Escoubet, C. P., Schmidt, R., and Goldstein, M. L.: Cluster - Science and Mission Overview, Space Science Reviews, 79, 11–32, 1997.

Escoubet, C. P., Fehringer, M., and Goldstein, M.: IntroductionThe Cluster mission, Ann. Geophysicae, 19, 1197–1200, 2001.

Fedorov, E., Schekotov, A. J., Molchanov, O. A., Hayakawa, M., Surkov, V. V., and Gladichev, V. A.: An energy source for the mid-latitude IAR: World thunderstorm centers, nearby discharges or neutral wind fluctuations?, Physics and Chemistry of the Earth, 31, 462–468, doi:10.1016/j.pce.2006.02.001, 2006.

Fenrich, F. R., Samson, J. C., Sofko, G., and Greenwald, R. A.: ULF high- and low-m field line resonances observed with the Super Dual Auroral Radar Network, J. Geophys. Res., 100, 21 535–21 548, 1995.

Fujita, S., Glassmeier, K. H., and Kamide, K.: MHD waves generated by the Kelvin-Helmholtz instability in a nonuniform magnetosphere, J. Geophys. Res., 101, 27 317–27 326, doi:10.1029/96JA02676, 1996.

Gabor, D.: Theory of communication, J. Inst. Elec. Eng., 93, 429–457, 1946.

Glassmeier, K. H.: Magnetometer array observations of a giant pulsation event, J. Geophys., 48, 127–138, 1980.

Glassmeier, K. H.: On the influence of ionospheres with non-uniform conductivity distribution on hydromagnetic waves, J. Geophys., 54, 125–137, 1984.

Glassmeier, K. H.: Reconstruction of the ionospheric influence on ground-based observations of a short-duration ULF pulsation event, Planet. Space Sci., 36, 801–817, doi:10.1016/0032-0633(88)90086-4, 1988.

Glassmeier, K. H.: Handbook of Atmospheric Electrodynamics, chap. ULF Pulsations, pp. 463–502, 1995.

Glassmeier, K. H. and Motschmann, U.: Comments on Time-Series Analysis, ESA SP-371: Proceedings of the Cluster Workshops, Data Analysis Tools and Physical Measurements and Mission-Oriented Theory, pp. 7–14, 1995.

Glassmeier, K. H., Lester, M., Mier-Jedrzejowicz, W. A. C., Green, C. A., Rostoker, G., Orr, D., Wedeken, U., Junginger, H., and Amata, E.: Pc5 pulsations and their possible source mechanisms - A case study, J. Geophys., 55, 108–119, 1984a.

Glassmeier, K. H., Volpers, H., and Baumjohann, W.: Ionospheric Joule dissipation as a damping mechanism for high latitude ULF pulsations: Observational evidence, Planet. Space Sci., 32, 1463–1466, 1984b.

Glassmeier, K. H., Othmer, O., Cramm, R., Stellmacher, M., and Engebretson, M.: Magnetospheric Field Line Resonances: A Comparative Planetology Approach, Surv. Geophys., 20, 61–109, 1999.

Goldstein, J.: Plasmasphere Response: Tutorial and Review of Recent Imaging Results, Space Science Review., 124, 203–216, doi:10.1007/s11214-006-9105-y, 2006.

Goldstein, J., Denton, R. E., Hudson, M. K., Miftakhova, E. G., Young, S. L., Menietti, J. D., and Gallagher, D. L.: Latitudinal density dependence of magnetic field lines inferred from Polar plasma wave data, J. Geophys. Res., 106, 6195–6202, doi:10.1029/2000JA000068, 2001.

Goldstein, J., Spiro, R. W., Reiff, P. H., Wolf, R. A., Sandel, B. R., Freeman, J. W., and Lambour, R. L.: IMF-driven overshielding electric field and the origin of the plasmaspheric shoulder of May 24, 2000, Geophys. Res. Letters, 29, 160 000–1, 2002.

Goldstein, J., Kanekal, S. G., Baker, D. N., and Sandel, B. R.: Dynamic relationship between the outer radiation belt and the plasmapause during March-May 2001, Geophys. Res. Letters, 32, 15 104–15 107, doi:10.1029/2005GL023431, 2005.

Goossens, M.: Advances in Solar System Magnetohydrodynamic, chap. Magnetohydrodynamic Waves and Wave Heating in Non-Uniform Plasmas, Cambridge University Press, 1991.

Guiter, S. M., Rasmussen, C. E., Gombosi, T. I., Sojka, J. J., and Schunk, R. W.: What is the source of observed annual variations in plasmaspheric density?, J. Geophys. Res., 100, 8013–8020, 1995.

Gustafsson, G., Bostrom, R., Holback, B., Holmgren, G., Lundgren, A., Stasiewicz, K., Ahlen, L., Mozer, F. S., Pankow, D., Harvey, P., Berg, P., Ulrich, R., Pedersen, A., Schmidt, R., Butler, A., Fransen, A. W. C., Klinge, D., Thomsen, M., Falthammar, C.-G., Lindqvist, P.-A., Christenson, S., Holtet, J., Lybekk, B., Sten, T. A., Tanskanen, P., Lappalainen, K., and Wygant, J.: The Electric Field and Wave Experiment for the Cluster Mission, Space Science Reviews, 79, 137–156, 1997.

Gustafsson, G., André, M., Carozzi, T., Eriksson, A. I., Fälthammar, C.-G., Grard, R., Holmgren, G., Holtet, J. A., Ivchenko, N., Karlsson, T., Khotyaintsev, Y., Klimov, S., Laakso, H., Lindqvist, P.-A., Lybekk, B., Marklund, G., Mozer, F., Mursula, K., Pedersen, A., Popielawska, B., Savin, S., Stasiewicz, K., Tanskanen, P., Vaivads, A., and Wahlund, J.-E.: First results of electric field and density observations by Cluster EFW based on initial months of operation, Ann. Geophysicae, 19, 1219–1240, 2001.

Hapgood, M. A.: Space physics coordinate transformations - A user guide, Planet. Spac Sci., 40, 711–717, doi:10.1016/0032-0633(92)90012-D, 1992.

Hasegawa, A.: Drift Mirror Instability in the Magnetosphere, Phys. Fluids, 12, 2642–2650, 1969.

Hasegawa, A.: Drift-Wave Instabilities of a Compressional Mode in a High-β Plasma, Phys. Rev. Lett., 27, 11–14, doi:10.1103/PhysRevLett.27.11, 1971.

Heacock, R. R.: Two Subtypes of Type Pi Micropulsations, J. Geophys. Res., 72, 3905–3917, 1967.

Hughes, W. J.: The effect of the atmosphere and ionosphere on long period magnetospheric micropulsations, Planet. Space Sci., 22, 1157–1172, doi:10.1016/0032-0633(74)90001-4, 1974.

Hughes, W. J. and Southwood, D. J.: The screening of micropulsation signals by the atmosphere and ionosphere, J. Geophys. Res., 81, 3234–3240, 1976.

Jacobs, J. A., Kato, Y., Matsushita, S., and Troitskaya, V. A.: Classification of Geomagnetic Micropulsations, J. Geophys. Res., 69, 180–181, 1964.

Jenkins, G. M. and Watts, D. G.: Spectral analysis and its appplications, pp. 313 – 317, Holden-Day, San Francisco, 1969.

Kivelson, M. G. and Southwood, D. J.: Coupling of global magnetospheric MHD eigenmodes to field line resonances, J. Geophys. Res., 91, 4345–4351, 1986.

Klimushkin, D. and Mager, P. N.: The spatio-temporal structure of impulse-generated azimuthalsmall-scale Alfvén waves interacting with high-energy charged particles in the magnetosphere, Ann. Geophysicae, 22, 1053–1060, 2004.

Klimushkin, D., Mager, P. N., and Glassmeier, K. H.: Toroidal and poloidal Alfvén waves with arbitrary azimuthal wavenumbers in a finite pressure plasma in the Earth's magnetosphere, Ann. Geophysicae, 22, 267–287, 2004.

Klimushkin, D. Y.: Spatial structure of transversally small-scale hydromagnetic waves in a plane finite-β model magnetosphere, Planet. Space Sci., 45, 269–279, 1997.

Klimushkin, D. Y.: Resonators for hydromagnetic waves in the magnetosphere, J. Geophys. Res., 103, 2369–2376, doi:10.1029/97JA02193, 1998a.

Klimushkin, D. Y.: Theory of azimuthally small-scale hydromagnetic waves in the axisymmetric magnetosphere with finite plasma pressure, Ann. Geophysicae, 16, 303–321, 1998b.

Klimushkin, D. Y. and Mager, P. N.: On the spatial structure and dispersion of slow magnetosonic modes coupled with Alfvén modes in planetary magnetospheres due to field line curvature, Planet. Space Sci., 56, 1273–1279, doi:10.1016/j.pss.2008.03.002, 2008.

Klimushkin, D. Y., Leonovich, A. S., and Mazur, V. A.: On the propagation of transversally small-scale standing Alfven waves in a three-dimensionally inhomogeneous magnetosphere, J. Geophys. Res., 100, 9527–9534, doi:10.1029/94JA03233, 1995.

Langel, R. A.: Teubner Taschenbuch der Mathematik, chap. Main Field in Geopmagnetism, Vol.1, pp. 249 – 512, Academic Press, London, 1987.

Lee, D.-H.: Dynamics of MHD wave propagation in the low-latitude magnetosphere, J. Geophys. Res., 101, 15 371–15 386, doi:10.1029/96JA00608, 1996.

Lee, D.-H. and Lysak, R. L.: Effects of azimuthal asymmetry on ULF waves in the dipole magnetosphere, Geophys. Res. Letters, 17, 53–56, 1990.

Lemaire, J.: The 'Roche-Limit' of ionospheric plasma and the formation of the plasmapause, Planet. Space Sci., 22, 757–766, doi:10.1016/0032-0633(74)90145-7, 1974.

Lemon, C., Toffoletto, F., Hesse, M., and Birn, J.: Computing magnetospheric force equilibria, J. Geophys. Res., 108, 1237–1248, doi:10.1029/2002JA009702, 2003.

Leonovich, A. S. and Mazur, V. A.: The spatial structure of poloidal alfven oscillations of an axisymmetric magnetosphere, Planet. Space Sci., 38, 1231–1241, doi:10.1016/0032-0633(90)90128-D, 1990.

Leonovich, A. S. and Mazur, V. A.: A theory of transverse small-scale standing Alfvén waves in an axially symmetric magnetosphere, Planet. Space Sci., 41, 697–717, doi:10.1016/0032-0633(93)90055-7, 1993.

Leonovich, A. S. and Mazur, V. A.: Magnetospheric resonator for transverse-small-scale standing Alfven waves, Planet. Space Sci., 43, 881–883, 1995.

Leonovich, A. S. and Mazur, V. A.: A model equation for monochromatic standing Alfven waves in the axially-symmetric magnetosphere, J. Geophys. Res., 102, 11 443–11 456, doi:10.1029/96JA02523, 1997.

Leonovich, A. S. and Mazur, V. A.: Standing Alfven waves in the magnetosphere from a localized monochromatic source, J. Geophys. Res., 104, 2411–2420, doi:10.1029/98JA02680, 1999.

Leonovich, A. S. and Mazur, V. A.: On the spectrum of magnetosonic eigenoscillations of an axisymmetric magnetosphere, J. Geophys. Res., 106, 3919–3928, doi:10.1029/2000JA000228, 2001.

Leonovich, A. S., Kozlov, D. A., and Pilipenko, V. A.: Magnetosonic resonance in a dipole-like magnetosphere, Annales Geophysicae, 24, 2277–2289, 2006.

Lui, A. T. Y. and Hamilton, D. C.: Radial profiles of quiet time magnetospheric parameters, J. Geophys. Res., 97, 19 325–19 332, 1992.

Lui, A. T. Y., McEntire, R. W., and Krimigis, S. M.: Evolution of the ring current during two geomagnetic storms, J. Geophys. Res., 92, 7459–7470, 1987.

Mager, P. N. and Klimushkin, D. Y.: Theory of azimuthally small-scale Alfvén waves in an axisymmetric magnetosphere with small but finite plasma pressure, J. Geophys. Res., 107, 10–1, doi:10.1029/2001JA009137, 2002.

Mager, P. N. and Klimushkin, D. Y.: On impulse excitation of the global poloidal modes in the magnetosphere, Ann. Geophysicae, 24, 2429–2433, 2006.

Mann, I. R. and Wright, A. N.: Finite lifetimes of ideal poloidal Alfvén waves, J. Geophys. Res., 100, 23 677–23 686, doi:10.1029/95JA02689, 1995.

Mann, I. R., Wright, A. N., and Cally, P. S.: Coupling of magnetospheric cavity modes to field line resonances: A study of resonance widths, J. Geophys. Res., 100, 19 441–19 456, 1995.

Mann, I. R., Wright, A. N., and Hood, A. W.: Multiple-timescale analysis of ideal poloidal Alfvén waves, J. Geophys. Res., 102, 2381–2390, 1997a.

Mann, I. R., Wright, A. N., and Hood, A. W.: Phase-mixing poloidal alfvén wave polarisations, Advances in Space Research, 20, 489–492, 1997b.

McDiarmid, D. R. and Allan, W.: Simulation and analysis of auroral radar signatures generated by a magnetospheric cavity mode, J. Geophys. Res., 95, 20 911–20 922, 1990.

McIlwain, C. E.: Magnetic Coordinates, Space Science Reviews, 5, 585–598, 1966.

McIlwain, C. E.: A Kp dependent equatorial electric field model, Advances in Space Research, 6, 187–197, doi:10.1016/0273-1177(86)90331-5, 1986.

McPherron, R. L.: Magnetic Pulsations: Their Sources and Relation to Solar Wind and Geomagnetic Activity, Surveys in Geophysics, 26, 545–592, doi:10.1007/s10712-005-1758-7, 2005.

Menk, F. W., Orr, D., Clilverd, M. A., Smith, A. J., Waters, C. L., Millng, D. K., and Fraser, B. J.: Monitoring spatial and temporal variations in the dayside plasmasphere using geomagnetic field line resonances, J. Geophys. Res., 104, 19 955–19 970, 1999.

Moldwin, M. B., Downward, L., Rassoul, H. K., Amin, R., and Anderson, R. R.: A new model of the location of the plasmapause: CRRES results, J. Geophys. Res., 107, 1339–1348, doi:10.1029/2001JA009211, 2002.

Newton, R. S., Southwood, D. J., and Hughes, W. J.: Damping of geomagnetic pulsations by the ionosphere, Planet. Space Sci., 26, 201–209, doi:10.1016/0032-0633(78)90085-5, 1978.

Ozeke, L. G. and Mann, I. R.: Modeling the properties of guided poloidal Alfvén waves with finite asymmetric ionospheric conductivities in a dipole field, J. Geophys. Res., 109, 5205–5219, doi:10.1029/2003JA010151, 2004.

Ozeke, L. G., Mann, I. R., and Mathews, J. T.: The influence of asymmetric ionospheric Pedersen conductances on the field-aligned phase variation of guided toroidal and guided poloidal Alfvén waves, J. Geophys. Res., 110, A08 210, 1–16, doi:10.1029/2005JA011167, 2005.

Park, C. G., Carpenter, D. L., and Wiggin, D. B.: Electron density in the plasmasphere - Whistler data on solar cycle, annual, and diurnal variations, J. Geophys. Res., 83, 3137–3144, 1978.

Pedersen, A., Mozer, F., and Gustafsson, G.: Electric Field Measurements in a Tenuous Plasma with Spherical Double Probes, in: Measurement Techniques in Space Plasmas – Fields, edited by Pfaff, R. F., Borovsky, J. E., and Young, D. T., pp. 1–12, 1998.

Pedersen, A., Décréau, P., Escoubet, C.-P., Gustafsson, G., Laakso, H., Lindqvist, P.-A., Lybekk, B., Masson, A., Mozer, F., and Vaivads, A.: Four-point high time resolution information on electron densities by the electric field experiments (EFW) on Cluster, Ann. Geophysicae, 19, 1483–1489, 2001.

Pierrard, V. and Cabrera, J.: Comparisons between EUV/IMAGE observations and numerical simulations of the plasmapause formation, Ann. Geophysicae, 23, 2635–2646, 2005.

Pierrard, V. and Lemaire, J. F.: Development of shoulders and plumes in the frame of the interchange instability mechanism for plasmapause formation, Geophys. Res. Letters, 31, 5809–5813, doi:10.1029/2003GL018919, 2004.

Pokhotelov, O. A., Pilipenko, V. A., and Amata, E.: Drift anisotropy instability of a finite-β magnetospheric plasma, Planet. Space Sci., 33, 1229–1241, doi:10.1016/0032-0633(85)90001-7, 1985.

Pokhotelov, O. A., Pilipenko, V. A., Nezlina, Y. M., Woch, J., Kremser, G., Korth, A., and Amata, E.: Excitation of high-β plasma instabilities at the geostationary orbit: Theory and observations, Planet. Space Sci., 34, 695–712, doi:10.1016/0032-0633(86)90124-8, 1986.

Poulter, E. M., Nielsen, E., and Potemra, T. A.: Field-aligned currents associated with Pc 5 pulsations - STARE and TRIAD observations, J. Geophys. Res., 87, 2331–2336, 1982.

Press, W. H., Teukolsky, S. A., Vetterlin, W. T., and Flannery, B. P.: Numerical Recepies - The Art of Scientific Computing, chap. 10 Minimizing or Maximizing of functions, Cambridge University Press, 3 edn., 2007.

Radoski, H. R.: Highly asymmetric MHD resonance: The guided poloidal mode, J. Geophys. Res., 72, 4026–4027, 1967.

Rème, H., Aoustin, C., Bosqued, J. M., and Dandouras, I.: First multispacecraft ion measurements in and near the Earth's magnetosphere with the identical Cluster ion spectrometry (CIS) experiment, Ann. Geophysicae, 19, 1303–1354, 2001.

Rickard, G. J. and Wright, A. N.: ULF pulsations in a magnetospheric waveguide: Comparison of real and simulated satellite data, J. Geophys. Res., 100, 3531–3537, 1995.

Russell, C. T.: Geophysical coordinate transformations., Cosmic Electrodyn., 2, 184–196, 1971.

Salat, A. and Tataronis, J. A.: Conditions for existence of orthogonal coordinate systems oriented by magnetic field lines, J. Geophys. Res., 105, 13 055–13 062, doi:10.1029/1999JA000221, 2000.

Samson, J. C.: Three-Dimensional Polarization Characteristics of High-Latitude Pc 5 Geomagnetic Micropulsations, J. Geophys. Res., 77, 6145–6160, doi:10.1029/JA077i031p06145, 1972.

Samson, J. C. and Rostoker, G.: Latitude-Dependent Characteristics of High-Latitude Pc 4 and Pc 5 Micropulsations, J. Geophys. Res., 77, 6133–6144, doi:10.1029/JA077i031p06133, 1972.

Samson, J. C., Jacobs, J. A., and Rostoker, G.: Latitude-Dependenct Characteristic of Long-Period Geopmagnetic Micropulsations, J. Geophys. Res., 76, 3675–3683, 1971.

Schäfer, S., Glassmeier, K. H., Eriksson, P. T. I., Pierrard, V., Fornaçon, K. H., and Blomberg, L. G.: Spatial and temporal characteristics of poloidal waves in the terrestrial plasmasphere: a CLUSTER case study, Ann. Geophysicae, 25, 1011–1024, 2007.

Schäfer, S., Glassmeier, K. H., Eriksson, P. T. I., Mager, P. N., Pierrard, V., Fornaçon, K. H., and Blomberg, L. G.: Spatio-temporal structure of a poloidal Alfvén wave detected by Cluster adjacent to the dayside plasmapause, Ann. Geophysicae, 26, 1805–1817, 2008.

Scholer, M.: On the motion of artificial ion clouds in the magnetosphere, Planet. Space Sci., 18, 977–1004, 1970.

Schulz, M.: Eigenfrequencies of geomagnetic field lines and implications for plasmadensity modeling, J. Geophys. Res., 101, 17 385–17 398, doi:10.1029/95JA03727, 1996.

Sciffer, M., Waters, C., and Menk, F.: Propagation of ULF waves through the ionosphere: Inductive effect for oblique magnetic fields, Ann. Geophysicae, 22, 1155–1169, 2004.

Sciffer, M. D., Waters, C. L., and Menk, F. W.: A numerical model to investigate the polarisation azimuth of ULF waves through an ionosphere with oblique magnetic fields, Ann. Geophysicae, 23, 3457–3471, 2005.

Singer, H. J.: Multisatellite observations of resonant hydromagnetic waves, Planet. Space Sci., 30, 1209–1218, 1982.

Singer, H. J. and Kivelson, M. G.: The latitudinal structure of Pc 5 waves in space - Magnetic and electric field observations, J. Geophys. Res., 84, 7213–7222, 1979.

Singer, H. J., Russell, C. T., Kivelson, M. G., Fritz, T. A., and Lennartsson, W.: Satellite observations of the spatial extent and structure of Pc 3, 4, 5 pulsations near the magnetospheric equator, Geophys. Res. Lett., 6, 889–892, 1979.

Singer, H. J., Hughes, W. J., and Russell, C. T.: Standing hydromagnetic waves observed by ISEE 1 and 2 - Radial extent and harmonic, J. Geophys. Res., 87, 3519–3529, 1982.

Southwood, D. J.: Preservation of the second adiabatic invariant during cross L diffusion, J. Geophys. Res., 77, 1123–1127, 1972.

Southwood, D. J.: Some features of field line resonances in the magnetosphere, Planet. Space Science, 22, 483–491, 1974.

Southwood, D. J.: Localised compressional hydromagnetic waves in the magnetospheric ring current, Planet. Space Sci., 25, 549–554, doi:10.1016/0032-0633(77)90061-7, 1977.

Southwood, D. J.: Wave generation in the terrestrial magnetosphere, Space Science Reviews, 34, 259–270, 1983.

Southwood, D. J. and Hughes, W. J.: Theory of hydromagnetic waves in the magnetosphere, Space Science Reviews, 35, 301–366, 1983.

Southwood, D. J. and Kivelson, M. G.: Charged particle behavior in low-frequency geomagnetic pulsations. II - Graphical approach, J. Geophys. Res., 87, 1707–1710, 1982.

Southwood, D. J. and Saunders, M. A.: Curvature coupling of slow and Alfvén MHD waves in a magnetotail field configuration, Planet. Space Sci., 33, 127–134, doi:10.1016/0032-0633(85)90149-7, 1985.

Southwood, D. J., Dungey, J. W., and Etherington, R. J.: Bounce resonant interaction between pulsations and trapped particles, Planet. Space Sci., 17, 349–361, 1969.

Sugiura, M.: Hourly values of equatorial Dst for the IGY, Ann. Int. Geophys. Year, 1964.

Sugiura, M.: Equatorial current sheet in the magnetosphere., J. Geophys. Res., 77, 6093–6103, 1972.

Takahashi, K. and Anderson, B. J.: Distribution of ULF energy (f is less than 80 mHz) in the inner magnetosphere - A statistical analysis of AMPTE CCE magnetic field data, J. Geophys. Res., 97, 10 751–10 773, 1992.

Takahashi, K., Denton, R. E., Anderson, R. R., and Hughes, W. J.: Frequencies of standing Alfvén wave harmonics and their implication for plasma mass distribution along geomagnetic field lines: Statistical analysis of CRRES data, J. Geophys. Res., 109, 1–15, doi = 10.1029/2003JA010 345,, 2004.

Tamao, T.: Transmission and coupling resonance of hydrodynamic disturbances in the non-uniform Earth's magnetosphere, Sci. Rep. Tohoku Univ., Ser 5, 17, 1965.

Tsurutani, B. T., Gonzalez, W. D., Lakhina, G. S., and Alex, S.: The extreme magnetic storm of 1-2 September 1859, J. Geophys. Res., 108, 1268–1275, doi:10.1029/2002JA009504, 2003.

Tsyganenko, N. A.: Global quantitative models of the geomagnetic field in the cislunar magnetosphere for different disturbance levels, Planet. Space Sci., 35, 1347–1358, doi:10.1016/0032-0633(87)90046-8, 1987.

Tsyganenko, N. A.: A magnetospheric magnetic field model with a warped tail current sheet, Planet. Space Sci., 37, 5–20, doi:10.1016/0032-0633(89)90066-4, 1989.

Tsyganenko, N. A.: Modeling the Earth's magnetospheric magnetic field confined within a realistic magnetopause, J. Geophys. Res., 1995.

Tsyganenko, N. A. and Peredo, M.: Analytical models of the magnetic field of disk-shaped current sheets, J. Geophys. Res., 99, 199–205, 1994.

Tsyganenko, N. A. and Stern, D. P.: Modeling the global magnetic field of the large-scale Birkeland current systems, J. Geophys. Res., 101, 27 187–27 198, 1996.

Vetoulis, G. and Chen, L.: Global structures of Alfven-ballooning modes in magnetospheric plasmas, Geophys. Res. Lett., 21, 2091–2094, 1994.

Vetoulis, G. and Chen, L.: Kinetic theory of geomagnetic pulsations 3. Global analysis of drift Alfvén-ballooning modes, J. Geophys. Res., 101, 15 441–15 456, doi:10.1029/96JA00494, 1996.

Walker, A. D. M.: Theory of magnetospheric standing hydromagnetic waves with large azimuthal wave number. I - Coupled magnetosonic and Alfven waves, J. Geophys. Res., 92, 10 039–10 045, 1987.

Walker, A. D. M. and Pekrides, H.: Theory of magnetospheric standing hydromagnetic waves with large azimuthal wave number 4. Standing waves in the ring current region, J. Geophys. Res., 101, 27 133–27 148, doi:10.1029/96JA02701, 1996.

Walker, A. D. M., Greenwald, R. A., Stuart, W. F., and Green, C. A.: STARE auroral radar observations of Pc 5 geomagnetic pulsations, J. Geophys. Res., 84, 3373–3388, 1979.

Warner, M. R. and Orr, D.: Time of flight calculations for high latitude geomagnetic pulsations, Planet. Space Sci., 27, 679–689, doi:10.1016/0032-0633(79)90165-X, 1979.

Williams, D. J.: Ring current composition and sources: An update, Planet. Space Sci., 29, 1195–1203, doi:10.1016/0032-0633(81)90124-0, 1981.

Woch, J., Kremser, G., Korth, A., Pokhotelov, O. A., Pilipenko, V. A., Nezlina, Y. M., and Amata, E.: Curvature-driven drift mirror instability in the magnetosphere, Planet. Space Sci., 36, 383–393, doi:10.1016/0032-0633(88)90126-2, 1988.

Wright, A. N., Allan, W., Elphinstone, R. D., and Cogger, L. L.: Phase mixing and phase motion of Alfvén waves on tail-like and dipole-like magnetic field lines, J. Geophys. Res., 104, 10 159–10 176, 1999a.

Wright, A. N., Allan, W., Elphinstone, R. D., and Cogger, L. L.: Phase mixing and phase motion of Alfvén waves on tail-like and dipole-like magnetic field lines, J. Geophys. Res., 104, 10 159–10 176, 1999b.

Ziesolleck, C. W. S., Fraser, B. J., Menk, F. W., and McNabb, P. W.: Spatial characteristics of low-latitude Pc3-4 geomagnetic pulsations, J. Geophys. Res., 98, 197–207, 1993.

Acknowledgements

Curriculum Vitae

Persönliche Daten:

Name:	Schäfer
Vorname:	Sebastian
Geburtstag:	27. September 1976
Geburtsort:	Braunschweig
Staatsangehörigkeit:	deutsch
Familienstand:	ledig

Schulbildung:

1983–1987	Grundschule Heinrichstrasse, Braunschweig
1987–1989	Orientierungsstufe Georg-Eckert Strasse, Braunschweig
1989–1996	Wilhelm-Gymnasium, Braunschweig
Juni 1996	Allgemeine Hochschulreife

Zivildienst:

1996–1997	Pfarrstelle für den Dienst an Geistigbehinderten in Braunschweig

Hochschulbildung:

1997–1999	Grundstudium der Physik an der TU Braunschweig
1999	Vordiplom Physik
1999–2003	Hauptstudium der Physik an der TU Braunschweig
2002–2003	Diplomarbeit am Institut für Geophysik und Meteorologie der TU Braunschweig ("Analyse von Plasmafluktuationen in der Erdmagnetosheath mit den Cluster 2-Satelliten als Wellenteleskop")
September 2003	Diplom Physik

Ausgeübte Tätigkeiten:

2000–2003	Wissenschaftliche Hilfskraft am Institut für Geophysik und Meteorologie der TU Braunschweig
2003–2008	Wissenschaftlicher Mitarbeiter am Institut für Geophysik und extraterrestrische Physik der TU Braunschweig
2004–2008	Mitglied der International Max Planck Research School on Physical Processes in the Solar System and Beyond

Veröffentlichungen:

Narita, Y., K.-H. Glassmeier, S. Schäfer, U. Motschmann, K. Sauer, I. Dandouras, K.-H. Fornaçon, E. Georgescu, H. Reme: Dispersion analysis of ULF waves in the foreshock using cluster data and the wave telescope technique, *Geophys. Res. Let., 30*, pp. SSC 43-1, 2003

Narita, Y., K.-H. Glassmeier, S. Schäfer, U. Motschmann, M. Fraenz, I. Dandouras, K.-H. Fornaçon, E. Georgescu, A. Korth, H. Reme, I. Richter: Alfven waves in the foreshock propagating upstream in the plasma rest frame: statistics from Cluster observations, *Ann. Geophysicae, 22*, pp.2315-2323, 2004

Schäfer, S., K.-H. Glassmeier, Y. Narita, K.-H. Fornaçon, I. Dandouras, M. Fraenz: Statistical phase propagation and dispersion analysis of low frequency waves in the magnetosheath, *Ann. Geophysicae, 23*, pp.3339-3349, 2005

Eriksson, P. T. I., L.G. Blomberg, S. Schäfer, K.-H. Glassmeier: On the excitation of ULF waves by solar wind pressure enhancements, *Ann. Geophysicae, 24*, pp.3161-3172, 2006

Eriksson, P. T. I., L.G. Blomberg, S. Schäfer, K.-H. Glassmeier: Sunward propagating Pc5 waves observed on the post-midnight magnetospheric flank, *Ann. Geophysicae, 26*, pp.1567-1579, 2008

Zhang, H., Q.-G. Zong, T. A. Fritz, S. Y. Fu, S. Schäfer, K.-H. Glassmeier, P. W. Daly, H. Rème, A. Balogh: Cluster observations of collisionless Hall reconnection at high-latitude magnetopause, *J. Geophys. Res., 113*, pp.3204-3213, 2008